ISBN 978-82-326-4674-6 (printed ver.)
ISBN 978-82-326-4675-3 (electronic ver.)
ISSN 1503-8181

NTNU
Norwegian University of
Science and Technology

Doctoral thesis

Markus Solberg Wahl

Doctoral theses at NTNU, 2020:163

NTNU
Norwegian University of Science and Technology
Thesis for the Degree of
Philosophiae Doctor
Faculty of Information Technology and Electrical
Engineering
Department of Electronic Systems

NTNU

Doctoral theses at NTNU, 2020:163

Markus Solberg Wahl

Detection and analysis of liquid-solid phase transitions with fiber-optic sensors

NTNU
Norwegian University of
Science and Technology

Markus Solberg Wahl

Detection and analysis of liquid-solid phase transitions with fiber-optic sensors

Thesis for the Degree of Philosophiae Doctor

Trondheim, May 2020

Norwegian University of Science and Technology
Faculty of Information Technology and Electrical Engineering
Department of Electronic Systems

NTNU
Norwegian University of
Science and Technology

NTNU
Norwegian University of Science and Technology

Thesis for the Degree of Philosophiae Doctor

Faculty of Information Technology and Electrical Engineering
Department of Electronic Systems

ISBN 978-82-326-4674-6 (printed ver.)
ISBN 978-82-326-4675-3 (electronic ver.)
ISSN 1503-8181

Doctoral theses at NTNU, 2020:163

Printed by NTNU Grafisk senter

Abstract

Fiber-optic sensors offer unique benefits within the field of experimental thermodynamics due to their small size and inert all-fiber design. Interrogation of the reflected signal enables insertion probes able to monitor harsh conditions, with fast response and minimal impact on the system. This thesis presents the development process – from understanding the fabrication and the associated challenges, through a proof-of-concept realization, to the application of fiber-optic sensors to study phase transitions.

The multi-mode fiber interferometers used are a simple and robust class of fiber-optic sensors, which can be designed to be sensitive to temperature, strain and refractive index (RI). The interference spectrum depends solely on the propagation constants and the geometry of the sensor, which is fabricated by splicing a section of coreless or thin-core fiber to the distal end of an optical fiber. Despite the simple fabrication, it is challenging to achieve a reproducible optical response. The thesis addresses this by investigating how inaccuracies in the geometry affect the ensemble of modes that is excited, and how this affects the produced spectrum. Guided-mode propagation simulations show that deviations in the cleave angle of the fiber end-face are more significant than inaccuracies in the spliced region. In the experimental results, however, large variations are observed independent of the cleave angle. It is concluded that the spliced region, which is more difficult to measure, plays a significant role in the produced spectrum.

The thesis proceeds to demonstrate how multi-mode fiber interferometers can be used in conjunction with a fiber-Bragg grating (FBG) to analyze phase transitions in binary mixtures of ethanol and water. The temperature and strain sensitivity of the FBG is used to decouple these parameters from the multi-mode interferometer (MMI) response. The remaining RI sensitivity of the MMI is used to measure the increased ethanol concentration caused by pure ice forming in the mixture. The measured melting points show excellent agreement with tabulated values.

The sensor system developed is then used to study ice formation in supercooled water-alcohol mixtures. The results are compared to theoretical predictions from heterogeneous nucleation theory. The effect on the nucleation barrier from solute type and concentration is studied, as well as the reduction in this barrier as a function of container material and pre-experiment rinsing procedures. Because of the dependency of the nucleation rate on the self-diffusivity of water, ice growth rates are measured in different ethanol concentrations to estimate the diffusivity at the liquid-solid interface.

Acknowledgement

The work presented in this thesis was conducted at the Department of Electronic Systems, Norwegian University of Science and Technology (NTNU), from 2016 to 2020. The work has been funded by Interreg, the energy and sensor systems group (ENERSENSE) and NTNU.

First of all, I want to thank my supervisors, Dag Roar Hjelme and Øivind Wilhelmsen. The best time I have had working with this thesis has been the time spent in our formal and informal meetings. I would not be sitting here writing my thesis if not for their great effort to teach, guide and encourage me. I want to thank Dag Roar for always having his door open, and always greeting my questions and ideas with a genuine interest and understanding. Our discussions, also the professional ones, have been essential for my well-being these years. I want to thank Øivind for all the optimism and inspiration he has given me these years. He has managed to balance between being a friend and a supervisor. He has pushed me when I needed pushing, and helped me when I needed helping. I know I have been extremely lucky with my supervisors. They have been the perfect combination, complementing each other with their tremendous knowledge and competence. I want to express my profound gratitude for all the time and energy they have spent on making this thesis possible.

I would like to thank Ian, my dear colleague and friend. Our projects together have been both fun and inspiring, and taught me a lot about being a researcher. I have really enjoyed all the trips we have made together, especially our rides to Røros and the Golden Gate Bridge. Most of all, I am grateful for our daily conversations. It has been

great to have someone to discuss both work related subjects and all the other aspects of life.

I want to further direct a special thanks to Robert, who has made me feel part of his small family with Kathi and Lolo. Thank you for the time we have spent all together, and the time with only the two of us. I have very much appreciated our meaningful discussions about life and work, spread out over the last four years.

A special thanks also to Arbab Ebi, for the strong connection we have made during these years. He has been, and still is, a very important part of my life.

I would also like to thank my co-disciple Ailo for the memorable moments we have shared, especially our trip to Boulder. I am also grateful for Ailos many precise and pedagogic explanations to the wonders of thermodynamics, which together with his great efforts towards the third paper of this thesis enabled me to finish my PhD.

By becoming a part of the ENERSENSE group, I have gotten to know a lot of amazing people. I want to thank the leader, Odne Burheim, Arbab Benham, Yash Bhai, Hujjat Bhai, Felix, Laura, Zohreh, Lena, Michael, Björn and everyone else for all the social activities, the scientific discussions, and for enabling me to meet my co-supervisor Øivind. Thanks also to Kjersti, for her highly contagious good mood and the time in our shared office at Kalvskinnet; Dominik, for the invaluable help with my LabVIEW programming and the highly interesting subjects he tends to bring up; and Jake, for our many funny discussions and the legendary trip back from Røros.

I have also been fortunate with the new colleagues I got when we moved to Gløshaugen. The casual discussions we have had in the hallway instantly sped up my project, but they were also a source to many interesting reflections on subjects not related to work. For this, I want to direct a special thanks to Silje, Ine, Karolina and Mukesh. I also enjoyed the few social activities I was able to join with Ambjørn, Ashkan, Bettina and Vitor.

I also want to my heartfelt gratitude and appreciation to Fredrik, Jakob, Jonas, Armend, Manuel, Nina, Børge, Johannes and Åsmund for all the good moments we have shared the last four years.

I am also tremendously grateful to my family for supporting me and for showing understanding to my life as a PhD candidate. My parents are always there if I need them and always support my decisions. My brother, Andreas and my sisters, Maria and Kristine, Mari, Øivind, Vetle, Maren and Sebastian never fail to brighten my day when I see them. I am especially grateful that Kristine has been here in Trondheim during most of my PhD, it has meant a lot to me.

Most of all, I want to thank Ingvild, who has never stopped supporting and believing in me. Her seemingly endless patience has only been interrupted by occasional strict directions to get my shit together, both of which I am forever grateful for.

List of Papers

The following publications are included in this thesis:

(I) **Addressing Challenges in Fabricating Reflection-Based Fiber Optic Interferometers**
Wahl, M.S., Wilhelmsen, Ø., Hjelme, D.R.
Sensors, 2019, 19, 18.

M.S.W., Ø.W. and D.R.H. conceptualized and designed the experiments; M.S.W. performed the experiments; M.S.W., Ø.W. and D.R.H. conceptualized and designed the model; M.S.W. created the model; M.S.W., Ø.W. and D.R.H. analyzed the results; M.S.W. prepared the original draft; Ø.W. and D.R.H. supervised and reviewed the paper.

(II) **Using Fiber-Optic Sensors to Give Insight into Liquid-Solid Phase Transitions in Pure Fluids and Mixtures**
Wahl, M.S., Wilhelmsen, Ø., Hjelme, D.R.
Submitted to *Experimental Thermal and Fluid Science*, Oct 31, 2019.

M.S.W., Ø.W. and D.R.H. conceptualized and designed the experiments; M.S.W. performed the experiments; M.S.W., Ø.W. and D.R.H. analyzed the results; M.S.W. prepared the original draft; Ø.W. and D.R.H. supervised and reviewed the paper.

(III) **Ice Formation and Growth in Supercooled Water–Alcohol Mixtures: Theory and Experiments with Dual Fiber Sensors**

Wahl, M.S., Aasen, A., Hjelme, D.R., Wilhelmsen, Ø.
Submitted to *Fluid Phase Equilibria*, Dec 23, 2019.

M.S.W., D.R.H and Ø.W. conceptualized and designed the experiments; M.S.W. performed the experiments; A.A. and Ø.W. conceptualized and designed the model; A.A created the model and performed the calculations; M.S.W., A.A., D.R.H. and Ø.W. analyzed the results; M.S.W., A.A. and Ø.W. prepared the original draft; Ø.W. and D.R.H. supervised and reviewed the paper.

The following works were published during the time of this thesis, but are not included:

Conference papers

1. **Dual parameter fiber optic sensor combining a Fabry-Perot and a Mach-Zehnder interferometer**
   Hammarling, K., Muri, H.I., Wahl, M.S., Engholm, M., Hjelme, D.R.
   2017 IEEE SENSORS Conference, 2017.

2. **Combined temperature and RI sensor for exploring the phase transitions of ethanol solutions**
   Wahl, M.S., Wilhelmsen, Ø., Hjelme, D.R.
   Optical Fiber Sensors (OFS) Conference, 2018 26th, 2018.

3. **Combining FBG and thin-core interferometers to analyse phase-transitions in binary fluids**
   Wahl, M.S., Wilhelmsen, Ø., Hjelme, D.R.
   Optical Fiber Sensors (OFS) Conference, 2020 27th, 2020. (*submitted*)

Conference abstracts

1. **A combined temperature sensor and phase transition detection probe on a single optical fiber**
   Wahl, M.S., Wilhelmsen, Ø., Hjelme, D.R.
   Twentieth Symposium on Thermophysical Properties, Boulder , June 24–29, 2018

Contents

1

Introduction

Water is a prerequisite for life and is present in virtually every aspect of our daily life. For humanity, water has always been a source of wonder, joy and suffering. From becoming one of the Aristotelian elements, up until today, water has sparked fascination and curiosity from scientists all over the world. Almost all industrial processes involve water, either as a solvent, product, reactant, or as an impurity. As a solvent, the properties of water, such as the boiling and freezing temperatures, depend on the concentration and properties of the solute. And as the only common substance to exist as a solid, liquid and gas under normal terrestrial conditions, the study of its transitions from one aggregate state to another is of tremendous interest.

At the time when this thesis is written, the age of sensors is upon us. What often is considered to be the first modern sensor, the thermostat, was invented in 1883 [1]. The world today has more than 20 billion sensor-containing devices connected to the internet [2]. Already in the year of 2009, the number of devices surpassed the human population, and the Internet of Things (IoT) was said to be born [3]. Today, sensors that measure temperature, pressure, proximity/distance, movement, humidity and electromagnetic waves, are a natural part of life.

With the invention of laser light in the year of 1960, the scientific progress towards optical waveguides was accelerated. The first fiber-optic sensor was patented already in 1967 – a proximity sensor based on bifurcated fiber bundles [4]. In 1970, the first low-loss, single-mode optical fiber from Corning Inc. sparked the development of modern communication technology [5]. More importantly for this work, these single-mode fibers enabled intrinsic interferometry, with significant advantages over sensors based on free space propagation. Because the light was now confined within the fiber, the sensors could also be embedded inside the materials to monitor the conditions from within [6].

Implementation of sensor technology in our society is expected to address eight out of the seventeen Sustainable Development Goals from the United Nation [7]. Sensors enable control and optimization, which may aid in the reduction of manufacturing costs, improving the utilization of natural resources, improving product quality, and with compliance to regulatory standards. Both implementation of existing solutions and development of new technology are important to reach these goals.

In the situation today, with increasing demand for energy and energy efficiency, there is a growing need for optimization and control. The EU's 20-20-20 goals – 20% increase in energy efficiency, 20% reduction of CO_2 emissions, and 20% renewables by 2020 – show the political incentive for new and improved solutions. The International Energy Agency (IEA) also found that most industrial processes use at least 50% more energy than what is theoretically required by the laws of thermodynamics [8]. When many thermodynamic processes include a transition from one aggregate state to another, such as hydrogen liquefaction [9], it is essential to optimize and control these transitions, also with regards to quality and safety [10, 11].

When measuring thermophysical properties, it is important to minimize the impact that the measurement has on the system. In that regards, fiber-optic sensors offer a unique possibility, with their inert material and small thermal mass. The possibility for remote sensing, and simple implementation in both experimental and industrial setups further strengthen the argument for this class of sensors. Their robustness from cryogenic temperatures [12] up to 1100°C [13] enables most phase transitions to be detected and analyzed.

1.1 The characteristics of phase transitions

In thermodynamics, a phase is a mechanically separable part of a system with homogeneous properties, such as temperature, pressure and concentration [14]. Therefore, the properties of a medium change when it transitions from one phase to another, e.g. between a solid, liquid, gas or plasma. These properties include e.g. the electrical conductivity, heat capacity, density, viscosity and refractive index. The phase transitions occur in response to changes in the external conditions, e.g. temperature and pressure, and often discontinuously. To know when a phase transition will occur and how it proceeds, is important in numerous industrial processes. Generally, these are processes where heat is exchanged, either purposely, e.g. to capture CO_2 [15], or where it is undesired, e.g. precipitation of inorganic salts from aqueous solutions [16].

1.2 Overview of characterization techniques

The simplest method to detect a phase transition is visual observation. Most materials look different depending on their aggregate state – transparent oils become opaque as they solidify, and gases are mostly transparent. In general, their optical properties change with aggregate state, e.g. how light is scattered, or how much is absorbed. Also the other physical properties that change during a phase transition can be measured to detect phase transitions.

Another method to detect phase transitions is to use the associated latent heat, also called enthalpy of fusion/solidification. Differences between the internal energies of the different phases must be supplied or removed in order for the transition to proceed. To melt ice into water, 333.55 J/g must be supplied, and the temperature will remain constant during the process. In freezing water, the same amount of energy is released.

Sensors are necessary to capture a phase transition based on the methods mentioned above. Visual inspection is not always viable in our automated world, but a camera with image processing can in some cases be an effective alternative [17]. However, this requires transparent windows or containers. Spectroscopic techniques, where the intensity of light is measured as a function its wavelength, may also be used to capture the wavelength-dependent changes associated with phase transitions in greater detail.

Techniques that measure other properties that change during a phase transition have also been demonstrated. By measuring changes in the impedance of the sample, Qin et al. [18] detected ice fouling on a subcooled metal surface. Zhang et al. [19] detected CO_2 frost points by measuring changes in pressure caused by the phase transition.

The latent heat associated with a phase transition may be detected by measuring the amount of heat that must be supplied/removed to increase/decrease the temperature, in comparison with a reference material. This technique is called differential scanning calorimetry (DSC), and was used by Takaizumi et al. [20, 21] and Koga et al. [22] to study the freezing of ethanol-water mixtures. Differential thermal analysis (DTA) is a simpler method, where the temperature is measured in comparison with a reference sample [17]. It is then important that the temperature measurement does not change the conditions of the experiment [23].

Whereas the above mentioned techniques are excellent for studying phase transitions, some may be complicated and difficult to implement in existing experimental setups. For instance, DSC requires the sample and reference to be compared under identical conditions, and the heat going into/out of both must be measured. To measure the impedance of a solution, the container also needs to be isolating to lead the current through the sample.

Fiber-optic sensor technology overcomes these challenges, with their simple implementation and small thermal masses. The ability for remote sensing also offers an intrinsically safe sensing system, which is ideal for monitoring in flammable environments. Although the ability for accurate measurements with little influence on the thermodynamic processes is ideal for analyzing phase transitions, the application of fiber-optic sensors for this purpose has so far received little attention. Only recently have researchers started exploring this field [24–27].

The fiber-optic techniques for phase transition detection are based on the difference in refractive index (RI) between the two phases. Han et al. used n-octadecane, which has RIs just above and below that of the glass used in optical fibers. This enabled easy characterization based on a guiding or no-guiding condition, and was demonstrated both in a multi-mode interferometer (MMI) [25] and a Fresnel reflection probe [24]. Although the RIs of n-octadecane is a special case, the principles can be used as long as there is a change in RI related to the phase transition. Mani et al. showed this by using a Fresnel reflection probe to detect freezing of aqueous NaCl-solutions [27]. These Fresnel-reflection sensors only have the cleaved end of the fiber in contact with the sample. This makes them mechanically robust, but also susceptible to irregularities such as impurities or bubbles that may be present. Kumar et al. detected melting of paraffin wax with an MMI by utilizing micro-strain in the sensor imparted by the solid phase [26].

Although the mentioned techniques are interesting and often well implemented, they do not fully exploit the potential of fiber-optic sensors to detect and analyze phase transitions. With fiber-optic sensors, both the temperature and concentration of the sample can be captured real-time during the progress of the phase transitions.

1.3 Aim and scope of the thesis

The aim of this thesis is to create a fiber-optic sensor system to detect and analyse liquid-solid phase transitions – and to demonstrate and evaluate its usefulness and the information it supplies. The temperature at which the nucleation and growth is initiated and how it progresses, represents important information about the system. Accurate sensing techniques that cause minimal perturbations to the system are important both with regards to improving the fundamental understanding of phase transitions, as well as in online monitoring of industrial processes. The thesis therefore intends to establish a general sensing system, based on fiber-optic sensors, which can be adapted and implemented in new or existing setups. The sensing system will be utilized to investigate liquid-solid transitions in aqueous ethanol mixtures in order to demonstrate its potential benefits.

The thesis treats challenges associated with fabricating fiber-optic sensors, limited to MMIs with their original diameter, i.e. no etching or side-polishing. The thesis also demonstrates how the information gained from the sensor system can be used in industrial monitoring or to obtain new insight about phase transitions, limited to liquid-solid and solid-liquid transitions.

1.4 Organization of the thesis

The following chapter presents the relevant background within the field of fiber-optic sensors, followed by a chapter on thermodynamic principles and classical nucleation theory. The experimental chapter contains details on the experimental setup, the fabrication of the sensors used in this thesis, as well as the theoretical framework and the implementation of the mode-field propagation model that has been developed. Then the publications included in this thesis are summarized and discussed, before the concluding remarks and suggestions for further work is presented. The papers will be presented chronologically according to their submission/publication date, as this order represents the progression of this work.

Fiber-optic sensors

2

A device that responds to a physical stimulus (such as heat, light, sound, pressure, magnetism, or a particular motion) and transmits a resulting impulse (as for measurement or operating a control)

— **Merriam-Webster**
definition of a sensor

A sensor is often defined as a device that outputs a signal in response to changes in its environment. The response should only be sensitive to the measurand, and insensitive to other parameters. It is also important that the influence by the presence or operation of the sensor on the measured property is minimized. This is especially important when measuring thermodynamic properties.

Active sensors depend on an excitation signal, which is modulated by the sensor. *Passive* sensors intrinsically exhibits a signal that is sensitive to the measured property. In both cases, the correlation between changes in the signal and the measured property needs to be established, often referred to as sensor calibration. Also, modern systems often require analog-to-digital conversion to utilize the measurement in our digital world. For chemical sensors and biosensensing, some sort of recognition is required to ensure adequate specificity [28]. This is not required when measuring parameters such as temperature and pressure, although cross-sensitivity may be an issue also here [29].

Fiber-optic sensors offer many advantages over conventional electrical sensors in certain situations. However, only few commercial successes have materialized despite great efforts from the research community [6, 30]. One possible reason for this is the competition with conventional sensors in well-established markets, such as within civil engineering [31]. Fiber-optic sensing technologies are therefore more popular in applications where they offer unique advantages over electrical sensors, e.g. where there is a need for low weight/volume, electrically passive sensing heads, or distributed measurements [6]. Examples of areas where fiber-optic sensors have been realized successfully include e.g. distributed sensing (temperature/acoustic) [6, 32], gyroscopes and specific chemical sensors [6].

The general setup for fiber-optic sensing is shown in Fig. 2.1, in a transmission geometry (a) and reflection geometry (b). In both cases, a light source is used to create the input signal, which in the end is captured by the detector and translated into a meaningful quantity by the electronics. Based on the measured parameter, the transducer modulates the signal with regards to its amplitude, frequency, polarization or phase. The transducer can be as small as only the end-face of the fiber [24], or *be* the whole length of the fiber as in distributed sensing [32].

In optical sensing, the sensor is often understood as the transducer alone, see Fig. 2.1. The transducer creates an optical signal, and the sensor system therefore also requires optical-to-electrical conversion (detector). Although the sensitivity of the sensor is often defined based on the transducer, the performance of the sensor system also depends on the light source, the detector and the electronics.

This chapter presents the relevant background and theory within the field of fiber-optic sensors, which will be limited to the sensor itself. This includes multi-mode and grating based interferometers with regards to measuring temperature and refractive index. First, a short introduction to fiber-optic waveguides is included.

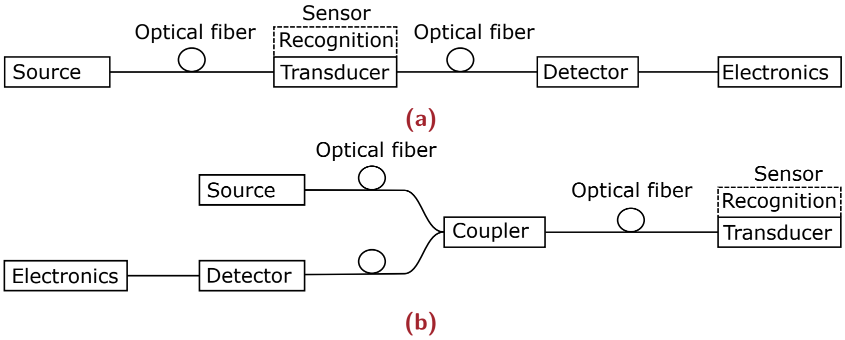

Fig. 2.1: Generalization of a fiber-optic sensor system in a transmission (a) and reflection (b) configuration.

2.1 Optical fibers as waveguides

Optical fibers are dielectric cylinders that guide light based on total internal reflection. The condition for guiding light is a higher RI in the guiding medium compared to the surroundings. In most optical fibers the light is guided in the core of the fiber, which has a higher RI than the surrounding cladding material, see Fig. 2.2.

Because the reflected wave needs to be self-consistent after two reflections, the limited diameter of the guiding medium only allows certain reflection angles θ_m. Each allowed reflection angle creates an electromagnetic field profile, which remains constant as it propagates through the fiber. These fields are called the *modes* of the fiber, and mode m propagates according to [33]

$$\beta_m = n_{core} k_0 \cos\theta_m, \tag{2.1}$$

where n_{core} is the RI of the core and $k_0 = 2\pi/\lambda_0$ is the free-space propagation constant. The quantity, $n_{eff} = n_{core}\cos\theta_m$ is often called the effective index, which is the ratio between the waveguide and the free-space propagation constants, $n_{eff} = \beta/k_0$.

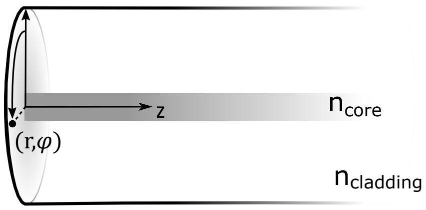

Fig. 2.2: Shows the cylindrical coordinates in the fiber.

The components of the electric and magnetic fields can be expressed in cylindrical coordinates (Fig. 2.2) as

$$U(r,\varphi,z) = u_{l,m}(r)\exp(-jl\varphi)\exp(-j\beta_{l,m}z), \tag{2.2}$$

where (l,m) are the mode indices, φ is the azimuthal angle. The radial field profile $u_{l,m}(r)$ can be found by solving the Helmholz equation. For a fiber with core radius a and an infinitely large cladding, the profiles are found to be expressed by Bessel functions

$$u_{l,m} \propto \begin{cases} J_l(k_T r), & r < a \quad \text{core} \\ K_l(\gamma r), & r > a \quad \text{cladding}, \end{cases} \tag{2.3}$$

where $k_T = \sqrt{n_{core}^2 k_0^2 - {\beta_{l,m}}^2}$, $\gamma = \sqrt{{\beta_{l,m}}^2 - n_{clad}^2 k_0^2}$, J_l is the Bessel function of the first kind, and K_l is the modified Bessel function of the second kind [33]. The parameters k_T and γ therefore defines the radial profile of the field, which will be described in greater detail in Sec. 4.2.

2.2 Interferometric sensors

A large group of optical sensors are based on interferometry – the principle of measuring the interference between two or more waves. From Michelson invented his interferometer in an attempt to detect the *aether* [34], the interferometric principle has become an important part of modern metrology. Optical interferometers generally exhibit high sensitivities and accuracies, because these quantities scale with the wavelength. In the last two decades, the advantages have also been utilized within the field of fiber-optic sensing. Due also to the robust, all-fiber design and simple fabrication, fiber-optic interferometers have received much attention and countless different designs have been realized [35].

To realize an interferometer, the light is split into different paths which exhibit different retardation based on the measured property. In an optical fiber, the different paths may be the *modes* of the fiber (Sec. 4.2), which propagate at different velocities and have different sensitivities. These are classified as multi-mode interferometers (MMI) due to the multiple modes contributing to the interference spectrum (Sec. 2.2.1). Fiber Bragg gratings are another class of interferometric sensors, where coherent refraction from periodic RI modulations in the fiber core generate a reflected peak (Sec. 2.2.2). If the grating is tilted with regards to the fiber axis (tilted-FBG), this can also be used to excite cladding modes in the fiber.

In this thesis a combination of a MMI and an FBG sensor was chosen to be able to independently measure temperature and RI. MMIs are easily fabricated and interrogated with standard spectrometers, but the cross-sensitivity between temperature, strain and RI complicates the analysis. The combination with a tempereature and strain sensitive FBG is therefore ideal to decouple the variables, as it exhibits a narrow-band resonance that can easily be detected when superimposed on the broad MM spectrum. An alternative configuration would be to use a tilted FBG (TFBG) which combines RI sensitive and *in*sensitive resonances. This is a very useful feature, but fabrication is more complicated and the sensors are not yet available for sale.

2.2.1 Multi-mode interferometers

In 1997, Matsubara et al. developed a hetero-core fiber-optic interferometer aimed at monitoring structural changes in landmasses to detect earthquakes or landslides [36]. The concept of cladding-mode interference has since then been used to measure e.g. temperature [37], strain [38], RI [39, 40], and as a fiber focusing lens [41]. The sensors can be realized in two configurations, either in transmission (Mach-Zehnder type) or in reflection (Michelson type). They can also be classified according to the method of cladding-mode excitation, e.g. core-diameter mismatch (hetero-core) [36, 37, 42], core offset [40], or long-period gratings [43].

The reflection-based, core-diameter mismatch type was chosen in this thesis, as rotationally symmetric insertion probes were desired. The sensors are fabricated by splicing a section of a core-diameter mismatched fiber to the end of a single-mode fiber (SMF), see Fig. 2.3. The mismatched cores cause an ensemble of higher order modes to be excited (see Sec. 4.2). If the fiber section is a multi-mode fiber i.e. the core is *larger* than the SMF core, the modes are bound by the cladding. In this case, the interference spectrum will be sensitive to temperature due to thermal expansion and the thermo-optic effect. It will also be sensitive to strain because it affects the optical path length (OPL), both by the strain directly and due to the strain-optic effect.

If the fiber section has a core that is *smaller* than the SMF, the excited modes will be bound by the outer diameter of the fiber. The evanescent field outside the fiber creates a sensitivity to the surrounding medium, as the effective index of each mode (n_{eff}) becomes a function of the external RI (n_{ext}). Because of the inherent different propagation constants of the modes, this creates an interference

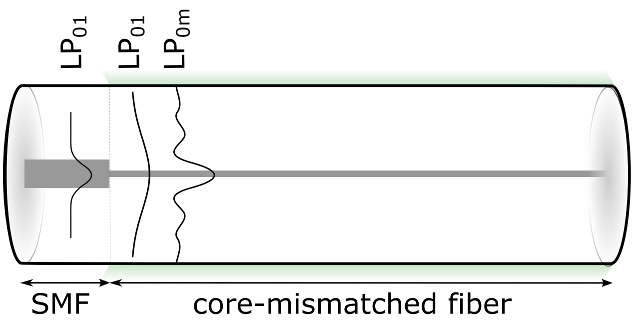

Fig. 2.3: A multi-mode interferometer fabricated by splicing a fiber segment with a core radius different from the single-mode fiber (SMF). The mismatched cores excite cladding modes that interfere due to different propagation constants.

spectrum at the spectrometer. Minima in the spectrum (λ_{dip}) occur when the difference in OPL is equal to an odd number of (π),

$$2\pi\left[n_{eff}(\lambda,n_{ext})-n'_{eff}(\lambda,n_{ext})\right]\frac{L}{\lambda_{dip}}=(2m+1)\pi. \tag{2.4}$$

Here, L is the propagation length and m is an integer. n_{eff} and n_{ext} are sensitive to temperature through the thermo-optic effect, and L is subject to thermal expansion and strain. Several minima will be observed because of the large number of modes that are excited. The expression that describes the temperature and RI sensitivities will be given in Sec. 2.4 and 2.5, respectively.

The sensitivity to the external RI can also be used to create sensors sensitive to relative humidity [43] and pH [44, 45] by applying stimuli-responsive coatings. The MMI will be explained in further detail when the theoretical model is presented in Sec. 4.2.

2.2.2 Grating-based sensors

Ken Hill et al. demonstrated the first fiber Bragg grating (FBG) in 1978. Although initially applied as narrow-band reflection filters, FBGs soon became popular as sensors [46]. Their inherent sensitivity to temperature and strain can be utilized directly as a sensing element. A coating may also be applied that either increases the inherent sensitivities or makes it sensitive to other parameters [47]. Most of these methods are based on the coating imparting strain on the fiber due to absorption of gas or other molecules [48, 49].

FBGs are also an important part of optical communication systems, where they function as notch filters [50]. Their narrow-band reflectivity enables them to be used in multiplexing, where it is used to add or extract specific frequencies (channels). This also an advantage when used in sensing, as it enables quasi-distributed sensing.

FBGs are fabricated by creating periodic variation in the core RI, see Fig. 2.4. This requires photosensitive fibers, which are usually achieved with germanium-doped fibers or by pre-loading the fiber with hydrogen. The RI variations are incscribed with high intensity UV light, either through two-beam interference or a phase mask.

Used as sensors, FBGs are usually interrogated by tracking the reflected wavelength, given by

$$\lambda_B = 2n_e\Lambda, \tag{2.5}$$

where λ_B is the reflected Bragg wavelength, n_{eff} is the effective refractive index and Λ is the grating period. The reflected wavelength is sensitive to strain due to the associated change in the grating period and the RI (strain-optic effect). Similarly, the temperature sensitivity

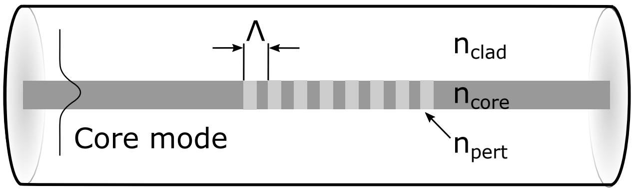

Fig. 2.4: A fiber-Bragg grating inscribed in a single-mode fiber. The periodic pertubations (n_{pert}) in refractive index cause light wavelengths given by Eq. 2.5 to be reflected.

is caused by thermal expansion in addition to the thermo-optic effect. This can be expressed as

$$\Delta\lambda_B = \lambda_B(\alpha + \xi)\Delta T, \tag{2.6}$$

where α and $\xi = dn/dT$ are the thermal expansion coefficient and the thermo optic coefficient, respectively.

Because the light is confined to the fiber core, FBG sensors are generally not sensitive to the surrounding medium. But as mentioned earlier, coating materials that undergo volumetric changes based on the mesurand concentration can be used to create sensitivities to other parameters.

In an FBG, the grating period is the same order of magnitude as the wavelength (Eq. 2.5). Poole et al. first reported that with longer grating periods the light may also be coupled into forward-propagating cladding modes. The long-period fiber gratings (LPGs) couple light from periodic perturbations in the range 100 μm to 1 mm. Strong coupling can be achieved when the periodicity of the perturbations Λ

is matched to the propagation constants of the core β_{01} and cladding modes $\beta_{cl}^{(n)}$ by the relation [51]

$$\beta_{01} - \beta_{cl}^{(n)} = \frac{2\pi}{\Lambda}. \tag{2.7}$$

The evanescent field creates the RI sensitivity because $\beta_{cl}^{(n)}$ depends on the external RI. The temperature and strain sensitivities follow the same principles as for FBG sensors. Although LPGs are normally interrogated in transmission, reflection-based insertion probes can be fabricated with an end-face mirror. The grating couples the reflected light, creating a fringe pattern with increased sensitivity [52].

If the FBG is inscribed at an angle to the fiber axis, cladding modes may also be excited [53]. This group of (tilted) FBGs is generally called TFBGs. The backwards propagating modes follow Eq. 2.7, where the large difference in propagation constants is enabled by the short-period grating similar to an FBG. The gratings can be designed such as to retain the RI *in*sensitive core mode reflection from standard FBGs. This is a great advantage as it enables independent temperature and RI measurements.

2.3 Distributed fiber-optic sensing

Another group of intrinsic fiber-optic sensors are the true distributed sensors, which measure the temperature or strain dependent backscattering along the entire length of the fiber [32]. Based on the type of backscattered light (Rayleigh, Raman, or Brillouin), either the frequency or intensity of the light is measured as a function of time. The position in the fiber is determined by a time-of-flight principle, either through optical time domain reflectometry (OTDR) or optical frequency domain reflectometry (OFDR).

2.4 Fiberoptic temperature sensors

FBGs are generally the simplest option for fiber-optic temperature sensing, with their linear sensitivity, high reflectivity, small size, and simple single-wavelength read-out [54]. The fabrication requires special equipment, but the sensors are readily available for purchase online. The only cross-sensitivity in FBGs is to strain, whereas RI sensitive sensors are also dependent on the temperature sensitivity of the surrounding medium. Because of the narrowband signal, FBGs can easily be multiplexed by including gratings with different periods on the same fiber, which then provide separate signals at different wavelengths [46]. This enables quasi-distributed sensing where the distance between each sensor defines the spatial resolution.

Efforts have also been made to discriminate temperature from strain in FBG sensors. One solution is to use two sensors with very different sensitivities to temperature and strain and calculate the inverted transfer matrix [46]. One way to do this is to use two FBGs with different cladding diameters, which will then exhibit different strain if subject to the same stress, but identical temperature response [55]. If the reflection spectrum is probed, the fiber can be cut and fixed only at one point. This will eliminate strain in liquid and gas media.

One of the most significant drawbacks of conventional FBG temperature sensors is the rapid degradation at temperatures exceeding 200°C [56]. Although improvements have been made on the stability at elevated temperatures [53, 57], the stability of MMIs is higher. Because these sensors are fabricated with standard fibers, they remain stable almost up to the glass transition temperature of SiO_2 (1475 K) [58]. Grating based sensors have been demonstrated to be stable up to around 800°C without modifications and 1190°C if annealed properly [54].

While the temperature sensitivity of an FBG is expressed by Eq. 2.6, the temperature sensitivity for MMIs can be found by writing the total differential of Eq. 2.4 and solving for $d\lambda_{dip}/dT$. The result can be written as [59]:

$$\frac{d\lambda_{dip}}{dT} \cong \left[\frac{\lambda_D}{\Delta n_{eff}}\left(\frac{\partial \Delta n_{eff}}{\partial n_{eff}}\frac{dn_{eff}}{dT} + \frac{\partial \Delta n_{eff}}{\partial n'_{eff}}\frac{dn'_{eff}}{dT}\right) + \frac{\lambda_D}{L}\frac{dL}{dT}\right] \Big/ \left(1 - \frac{\lambda_D}{\Delta n_{eff}}\frac{\partial n_{eff}}{\partial \lambda}\right), \quad (2.8)$$

which shows that the temperature sensitivity depends on the different sensitivity of the effective indices (n_{eff}, n'_{eff}) for the two modes that are considered.

The temperature sensitivity of the sensors is an important metric as it affects the resolution of the temperature measurement together with how accurate the wavelength of the signal can be determined. As a measure for the performance the figure of merit (FOM = S/$\Delta\lambda$) is often used for fiber-optic sensors, which relates the sensitivity, S to the linewidth of the signal, $\Delta\lambda$ often defined as the full width at half maximum (FWHM). For the sensors discussed, the sensitivity is defined as the shift in wavelength per degree. For FBG sensors, the sensitivity is typically around 10 pm/K [46], whereas MM interferometers have been realized in the range of 15-82 pm/K [42, 60, 61]. LPGs have reported sensitivities in the range of a few tens of pm/K [35].

The temperature sensitivity can be increased for all sensors by applying coatings with higher thermal expansion coefficients, although this introduces the possibility of detrimental delamination. External coating can also be used to remove the RI sensitivity of MM and LPG sensors [52]. Although MM interferometers and LPGs have some advantages over FBG temperature sensors, they exhibit more complicated spectra that makes multiplexing challenging.

2.5 Refractive index sensors

For direct measurements of refractive index (RI), the light needs to get in contact with the medium. In fiber-optic sensors, this is done through the evanescent field created by light bound by the outer diameter of the fiber, or at the end-face of the fiber as in Fresnel-reflection probes [24, 27]. For normal incidence, the Fresnel reflectivity R can be expressed as

$$R = \left(\frac{n_f - n_m}{n_f + n_m} \right)^2 , \tag{2.9}$$

where n_f is the fiber RI and n_m is the medium RI [33]. In an optical fiber, the reflectivity is actually governed by the effective index of the modes, but in an MMF this is approximately equal to the core index, $n_{eff} \approx n_f$.

As the reflectivity is a function of the index contrast, the reflected intensity can be used to determine the RI of the medium. To reduce the effect of fluctuations in the light source, the ratio relative to a reference arm can be utilized [24]. As only the end-face of the fiber is in contact with the sample, these sensors represent a mechanically robust alternative. But the small sensitive area also makes the measurement susceptible to impurities and irregularities.

The principle of operation for evanescent field-based RI sensing is based on the effective RI of the propagating light becoming a function of the RI outside the fiber (Eq. 2.4). The altered effective index can be estimated by a weighted average based on the confinement of the mode. Less confined modes will therefore exhibit a higher sensitivity, as a larger part of the electromagnetic field is propagating outside the fiber. How interference minima shift as a function of the external RI can be derived from the total differential of Eq. 2.4. With the expression for the group index ($n_g = n - \lambda\,\partial n/\partial\lambda$), this may be written as

$$\frac{d\lambda_{dip}}{dn_{ext}} = \frac{\lambda_{dip}}{(n_g - n'_g)}\left(\frac{\partial n}{\partial n_{ext}} - \frac{\partial n'}{\partial n_{ext}}\right). \tag{2.10}$$

This gives a positive RI sensitivity for most geometries because the first factor remains positive [62].

Bringing the evanescent field in contact with the surrounding medium can be done in several ways. Standard FBG sensors can be etched to reduce the cladding diameter [13, 63] or polished into a D-shaped fiber [64]. These sensors have the advantage that they have a strong and narrowband reflection peak, but are less mechanically robust. This is contrary to LPG sensors, with their inherent RI sensitivity. The option used in this thesis is through core-diameter mismatch, as described in Sec. 2.2.1, which enables the excitation of cladding modes. These sensors are mechanically robust and easily fabricated, but exhibit complicated spectra.

3

Liquid-solid phase transitions

Phase transitions occur everywhere in our daily life – from the bubbles that form in boiling water, to the water droplets and ice crystals that form in the atmosphere in relation to weather and climate. Although it is a physical phenomenon which has been studied for almost 300 years, the solidification of water into ice is still poorly understood [65–71].

This section will present the theory and literature relevant for liquid-solid transitions. This includes classical nucleation theory (CNT) and the application of equations of state (EoS) in thermodynamic modeling.

3.1 Important concepts and definitions

First a brief introduction to the concepts and definitions necessary for further treatment of the subject will be presented.

3.1.1 Phases

A material can exists in different states called phases, which have the same constituents but different properties. The different phases are defined based on how the constituents are ordered, which encompasses both their mobility, location and orientation [72].

3.1.2 Equilibrium state and state variables

A thermodynamic state is defined by the state variables, e.g. volume (V), pressure (P), temperature (T) and the number of molecules (N). These variables are measurable, and other quantities describing the system can be calculated from these. For each state of the system, the calculated variables (e.g. system energy (U), entropy (S), density (ρ), chemical potential μ) are uniquely defined.

In terms of the thermodynamic variables, the equilibrium state can be defined as where the free energy of the system is minimized, or where the total entropy of the system and surrounding is maximized. Which condition that is used, depends on the constraints on the system. In systems where the temperature and volume is kept constant, the Helmholtz energy is minimized, whereas the Gibbs energy is used for constant temperature and pressure. For completely isolated systems, the entropy is maximized at thermodynamic equilibrium.

The functional relation between the measured quantities are called equations of state (EoS), which can take the general form $f(P, V, T) = 0$. The concept of EoS and how they are used in thermodynamic modeling will be further treated in Sec. 3.4.

3.1.3 Chemical potential and surface tension

The chemical potential μ_i of a component i in a bulk system is defined as

$$\mu_i = \left(\frac{\partial U}{\partial N_i}\right)_{S,N_{j\neq i},V} = \left(\frac{\partial G}{\partial N_i}\right)_{T,P,N_{j\neq i}}, \tag{3.1}$$

which means the change in system energy when one molecule of component i is added, when the entropy S, number of other molecules $N_{j\neq i}$ and volume V are kept constant. Or, the change in Gibbs free energy G, with the temperature T, pressure P, and other molecules kept constant.

The energetic contribution from a surface between two phases can similarly be described by the the surface tension, γ, which is defined as the change in system energy when the surface area is increased, while keeping the entropy, number of molecules and volume constant

$$\gamma = \left(\frac{\partial U}{\partial A}\right)_{S,N_i,V}. \tag{3.2}$$

The change in energy is caused by the molecules having less negative energy than molecules in the interior of the system.

3.1.4 Phase equilibrium

To find the requirements for phase equilibria, a simplified derivation is included. This assumes a perfectly spherical nucleus with the same density as the liquid, and disregards effects from the crystal structure.

The general properties of a system consisting of two phases in equilibrium can be found with the expressions for the change in energy of the two phases

$$dU_p = T_p dS_p - P_p dV_p + \sum_i \mu_{i,p} dN_{i,p} \tag{3.3}$$

and the interface between them

$$dU_s = T_s dS_s - \gamma dA + \sum_i \mu_{i,s} dN_{i,s}. \tag{3.4}$$

The subscript p represents either of the two phases, s the interface, and i the molecule species.

In thermodynamic equilibrium the total entropy S_{tot} is maximized, which means that $dS_{tot} = dS_1 + dS_2 + dS_s = 0$. In an insulated rigid system, the total energy is constant ($dU_{tot} = 0$), the total volume is constant ($dV_{tot} = 0$), and the total number of molecules is constant ($dN_{tot} = 0$). With a flat interface, the interface area remains unchanged (disregarding constraints from the container shape) although molecules transfer from one phase to the other. This is not the case with curved interfaces, where an increased radius causes a larger surface area.

Solving Eq. 3.3 and 3.4 for the entropy in the two phases (liquid, 1; nucleus, 2) and a curved interface between them, the terms can be added to give the expression

$$dS_{tot} = \left(\frac{1}{T_1} - \frac{1}{T_s}\right) dU_1 + \left(\frac{1}{T_2} - \frac{1}{T_s}\right) dU_2 + \sum_i \left(\frac{\mu_{i,1}}{T_1} - \frac{\mu_{i,s}}{T_s}\right) dN_{i,1} + \sum_i \left(\frac{\mu_{i,2}}{T_2} - \frac{\mu_{i,s}}{T_s} d\right) dN_{i,2} + \left(\frac{P_1}{T_1} - \frac{P_2}{T_2} + \frac{2\gamma}{T_s r}\right) dV_1. \tag{3.5}$$

$dV_1 = -dV_2$ because the total volume is constant. The last term comes from the relation between the surface and volume of a spherical particle with radius r. With the requirement that $dS_{tot} = dS_1 + dS_2 + dS_s = 0$ regardless of which quantity is varied (i.e. the other parameters are kept constant), and that $dU_{tot} = 0$, $dV_{tot} = 0$ and $dN_{tot} = 0$, the following conditions for phase equilibrium can be established:

$$T_1 = T_2 = T_s \tag{3.6}$$

$$\mu_{i,1} = \mu_{i,2} = \mu_{i,s} \tag{3.7}$$

$$\frac{P_1}{T_1} - \frac{P_2}{T_2} + \frac{2\gamma}{T_s r} = 0 \tag{3.8}$$

For flat interfaces, r is infinite, which gives $p_1 = p_2$. Eq. 3.6 and 3.8 also gives the *Young-Laplace equation* which relates the pressures over a curved interface:

$$P_1 = P_2 + \frac{2\gamma}{r} \tag{3.9}$$

In summary, this means that for phases in thermodynamic equilibrium, the chemical potentials and the temperature of both phases need to be the same and the pressure given by the Laplace equation.

3.1.5 Gibbs energy

Gibbs energy is a thermodynamic potential which describes the free energy of systems that are interacting with temperature and pressure reservoirs, where work and heat can be exchanged with the reservoir by e.g. increasing/decreasing its volume. At thermodynamic equilibrium in such systems, the Gibbs energy is minimized. Systems with constant temperature and pressure are commonly encountered. Many processes take place in the atmosphere where the temperature and pressure can be considered constant.

The Gibbs energy is expressed as

$$G = U - TS + PV, \tag{3.10}$$

which together with the Euler relation $U = TS - PV + \mu_1 N_1 + \mu_2 N_2$ for a two-component system, becomes

$$G = \mu_1 N_1 + \mu_2 N_2. \tag{3.11}$$

The change in Gibbs energy for an infinitesimal change in either N_1 or N_2 can therefore be written as $dG = \mu_1 dN_1 + \mu_2 dN_2$. By keeping one component constant, this gives the second definition of the chemical potential given in Eq. 3.1.

3.2 Classical Nucleation Theory

Classical nucleation theory (CNT) is a phenomenological approach used to estimate the free energy of formation for clusters of a new phase, based on macroscopic properties [73]. This is contrary to molecular, first principle, approaches (e.g. molecular dynamics, Monte Carlo simulations), which induce and investigate cluster formation by letting each particle in the system interact based on interaction potentials [68]. In molecular dynamics, this is done by solving Newtons equations of motion. CNT can be used to describe a variety of phase transitions (e.g. condensation, boiling, crystallization, melting), but the treatment here will be limited to liquid-solid transitions.

The evolution of a first-order phase transition can be divided into two steps, the formation of a cluster (nucleation) in the original metastable phase, and the growth of this cluster into a new phase [74]. In general, the crystal growth is fast, and the activation barrier for the creation of a new phase is dominated by the nucleation event. Whereas the melting of water occurs as soon as the temperature exceeds $0°\text{C}$ [75], the initiation of a freezing process in general requires the system to deviate further into the metastable region. The deviation creates a driving force which aids in overcoming the activation barrier of the nucleation [73]. In this work, the driving force depends on the degree of supercooling, $\Delta T = T_m - T$, where T_m is the melting temperature.

The mathematical foundation in CNT is based on the competing terms of the volumetric driving force for the cluster growth and the cost of increasing the surface area. In terms of Gibbs energy, this can be expressed as $\Delta G_{cluster} = \Delta G_v + \Delta G_a$, where the subscript v denotes the volumetric term and a the area. Small clusters continuously form and dissipate. Only when a cluster reaches a critical size r^* will further growth be thermodynamically favorable ($\Delta G_{cluster} < 0$), see Fig. 3.1. For spherical clusters, the free energy of formation can be expressed as [76],

$$\Delta G_{cluster} = \frac{4}{3}\pi r^3 \Delta g + 4\pi r^2 \gamma, \tag{3.12}$$

where r is the cluster radius, γ the surface tension. Δg is the thermodynamic driving force for forming a nucleus per unit volume. The critical radius is found by setting the derivative of Eq. 3.12 equal to zero, which when inserted back into the original equation gives

$$\Delta G^*_{cluster} = \frac{16\pi}{3} \frac{\gamma^3}{\Delta g^2}. \tag{3.13}$$

The Arrhenius equation from Volmer and Weber describes the steady-state nucleation rate [77]

$$J = J_{kin} \exp\left(-\frac{\Delta G^*_{cluster}}{k_B T}\right). \tag{3.14}$$

The product of the Boltzmann constant and the temperature $k_B T$ represents the thermal energy in the system, and J_{kin} is a kinetic prefactor that will be discussed in Sec. 3.4. The quantities mentioned thus far are all functions of pressure [78] and temperature [68]. The surface tension is generally assumed to vary linearly with temperature, whereas the volumetric driving force Δg is proportional to the degree of supercooling. The latter therefore means that the kinetic barrier (Eq. 3.13) decreases for greater supercooling temperatures, which again results in a higher nucleation rate.

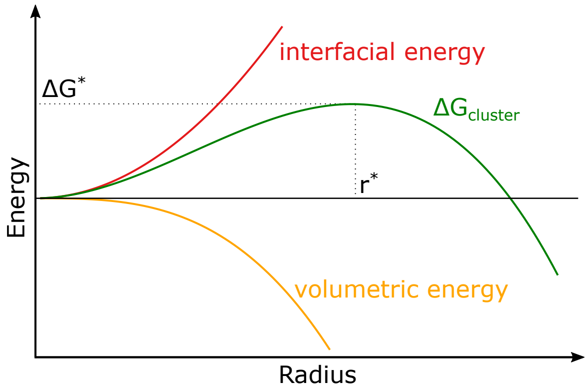

Fig. 3.1: The energy terms as a function the cluster radius, from Eq. 3.12. Because of the opposite sign of the two terms (Δg and γ), the sum has a maximum value for the critical radius r^*.

3.2.1 Heterogeneous nucleation

In most situations, ice nucleation is catalyzed by a foreign phase, which is called heterogeneous nucleation. The presence of the new interface lowers the nucleation barrier, which by Eq. 3.14 increases the nucleation rate. The result is that a critical cluster is more probable to form at higher temperatures (i.e. lower supercooling). In fact, simulations have shown that ice nucleation less than 20 K below the melting point must be heterogeneous [66].

A common way to express the reduction in the free energy barrier is with the shape factor $f(\theta)$, where θ is the contact angle [68, 72, 79, 80]:

$$\Delta G_{het} = f(\theta)\Delta G^*_{cluster}. \tag{3.15}$$

The concept of the contact angle is only applicable for ideal planar surfaces, where it is given by the Young's relation. The contact angle is a macroscopic property and relies on a spherical geometry, both of which can not be directly transferred to the length scales relevant for nucleation [68]. Also, actual nucleating surfaces often have many different nucleation sites with various morphologies, which makes predictions complicated. Pruppacher et al. lists criteria for a surface to be an efficient ice nucleator: i) it should be highly water-insoluble; ii) the surface should be able to form hydrogen bonds similar to those in the ice crystal; iii) the atomic or molecular structure of the surface should resemble low-index planes in the ice crystal [81]. Bi et al. further clarifies that these criteria are suggestive rather than predictive, and that no unique correlation has been established [70]. In fact, many papers clearly state that heterogeneous nucleation of ice is still poorly understood [66–71].

The cooling rate must also be considered, as the nucleation rate describes the stochastic nature of the freezing event [22].

3.3 Binary mixtures and colligative effects

Melting-point depression, often called freezing-point depression, is the decrease in melting temperature in solvents caused by an addition of a non-volatile solute. This colligative effect can be explained by the lower chemical potential of the solvent in a mixture than in the pure liquid. The decrease in chemical potential is caused by the increased entropy in mixtures, and hence a greater increase in the entropy gained for a molecule going from the solid to the liquid phase. With coexisting liquid and solid phases, the equilibrium requires the chemical potentials to be equal. In a mixture, a lower (melting) temperature is therefore required to satisfy the equilibrium condition [82].

Due to the linear relationship in Eq. 3.15, the freezing point depression is expected to follow approximately the same trend.

It should also be noted that the solid formed in binary mixtures of water will be pure ice for the dilute concentrations used in this thesis [20, 22, 83].

3.4 Equations of State and Modeling

As explained in Sec. 3.1, equations of state (EoS) describe the relation between state variables in a thermodynamic system. A simple and probably the most well-known example of an EoS is the *ideal gas law*:

$$PV - nRT = 0, \tag{3.16}$$

where n is the number of moles and R the ideal gas constant. The ideal gas law describes a hypothetical ideal gas, which neglects both molecular size and inter-molecular attraction forces. It can therefore be a good approximation for low-density, monoatomic gases.

One of the first modifications to the ideal gas law came with the *van der Waals equation of state*. The finite volume of the gas molecules were accounted for by subtracting the volume occupied by the molecules (nb), and a term for inter-molecular attraction was added to the pressure:

$$\left(P + a\frac{n^2}{V^2}\right)(V - nb) = nRT, \tag{3.17}$$

where b represents the volume occupied by one molecule and a describes the attraction forces. Because the van der Waals equation can be written as a cubic function of V it is classified as a cubic EoS. Another EoS that is widely used to describe complex phase equilibria today is the *cubic plus association* (CPA) [84], which will be presented next.

3.4.1 Cubic plus association

The CPA EoS is a popular EoS that was developed to also describe compounds with polar or hydrogen bonding components [84]. The EoS is based on the cubic Soave-Redlich-Kwong (SRK) equation [85], with an association term from Wertheim theory [86]. The EoS can be expressed as [84]:

$$P = \frac{RT}{V_m - b} - \frac{\alpha(T)}{V_m(V_m + b)} \\ - \frac{1}{2}\left(\frac{RT}{V_m}\right)\left(1 + \frac{1}{V_m}\frac{\partial \ln g}{\partial(1/V_m)}\right)\sum_i x_i \sum_{A_i}(1 - X_{A_i}). \quad (3.18)$$

$\alpha(T)$ gives a temperature dependence to the attractive forces, V_m is the molar volume, g is the radial distribution function and x_i is the mole fraction of component i. X_{A_i} is the fraction of unbonded active sites and needs to be determined for the specific system. With no associating compounds, it reduces to the cubic SRK equation of state. The CPA EoS can be challenging to use with mixtures where both components are self-associating, such as alcohol-water mixtures [87]. One of the reasons for this, is that the interaction parameter may then have to describe both the vapor-liquid and liquid-liquid equilibria. However, with the parameters for the pure components [88, 89] and accurate experimental data on the vapor-liquid equilibrium (VLE) [90–93], the binary interaction parameters k_{ij} can be calculated. As these parameters are validated only for VLEs, the accuracy is not confirmed for the solid phase.

3.4.2 The Equation of state for ice Ih

Hexagonal ice (Ih) is the most commonly found form in the biosphere of the earth [94]. An EoS for ice Ih has been constructed by Feistel and Wagner [95], which is valid over the entire $T - P$ existence region. The equation describes the behavior of pure ice at equilibrium, which includes ice that precipitates from mixtures. The EoS is expressed as a Gibbs potential function

$$g(T,P) = g_0 - s_0 T_t \tau + T_t \,\mathrm{Re} \sum_{k=1}^{2} r_k \Bigg[(t_k - \tau) \ln(t_k - \tau) \\ + (t_k + \tau) \ln(t_k + \tau) - 2t_k \ln t_k - \frac{\tau^2}{t_k} \Bigg], \qquad (3.19)$$

which is equal to the chemical potential of ice $\mu_{Ih}(T,P)$. The residual Gibbs energy g_0 and r_2 are polynomials of pressure s_0 a real constant, T_t the triple point temperature, $\tau = T/T_t$ the reduced temperature, and t_1, t_2 and r_1 are complex constants. Re takes the real part of the whole expression within the summation.

To match the two models (CPA+Ice), two adjustable parameters of the ice EoS must be determined. This can be done by defining two conditions: (1) the experimental triple point temperature and pressure must be reproduced by the combined model; (2) the enthalpy of fusion $\Delta H_{ice/liq}$ at the triple point calculated with the combined models must be equal to the experimental value (6007 J/mol).

3.4.3 Determining the melting point

At the melting point, the liquid and the solid phases coexist – they are in thermodynamic equilibrium. As was found in Sec. 3.1, this means that the temperature, pressure and chemical potential (T, P, μ) must be equal in the two phases. Because the chemical potential of water in a mixture is lowered, the melting point also decreases (see Sec. 3.3). To estimate the melting point, the CPA+Ice model must therefore be solved under this requirement, which can be done with the algorithms outlined in [96]. With the estimated melting points, the amount of supercooling required to initiate the phase transitions can be estimated.

3.4.4 Modeling the nucleation barrier

As was seen in Sec. 3.2.1, the nucleation rate scales exponentially with the kinetic energy barrier, with the driving force being the degree of supercooling. To determine the freezing temperature, the melting temperature therefore needs to be known. The nucleation barrier is equal to the work of formation for a critical ice cluster. How the work of formation for ice depends on the alcohol concentration will be presented subsequently. To simplify the notation, the work of formation will henceforth be expressed as $W = \Delta G^*_{cluster}$. Because of the pressure difference across the curved interface of a cluster (Eq. 3.9) a more convenient expression for W is [72]

$$W = -\Delta P V_c + A_c \gamma_{i,w}, \tag{3.20}$$

for homogeneous nucleation. V_c and A_c are the volume and area of the critical cluster, defined by the critical radius (spherical), and $\gamma_{i,w}$ is the ice-water surface tension. The first term describes the PV-work from creating the cluster, and the second is the work required to create the new interface. From Eq. 3.9, the size of the critical cluster becomes

$$R^* = \frac{2\gamma_{i,w}}{\Delta P}, \tag{3.21}$$

with the two unknown quantities $\gamma_{i,w}$ and ΔP. The temperature dependent surface tension can be estimated from data in the literature [74, 97, 98], whereas the pressure difference is estimated from the CPA+ice model. This is done with the requirement that the chemical potential is equal in the liquid and solid phases, where the chemical potential in the liquid is given by CPA at the specific temperature and concentration. The chemical potential in the ice is given by the ice-EoS, but requires a higher pressure to match the chemical potential in the liquid phase.

The work of formation is the difference between the two state functions, independent of the pathway of the process. One sequence that can be chosen is to first calculate the osmotic work (ΠV_c) to remove all solute molecules in the volume V_c. This is required because the ice cluster consists of only water, which creates an osmotic pressure Π [97, 99]. Then, the cluster of pure water can be converted to ice, where the energy involved is the work of formation for pure water. The ice cluster also needs to equilibrate with the liquid mixture, but the energy involved is assumed to be small and is commonly omitted in the literature [97, 99]. The combined energies of the pathway described gives the work of formation in mixtures, which then can be expressed as

$$W = (\Pi - \Delta P)V_c + A_c\gamma_{i,w}. \tag{3.22}$$

The above discussion is limited to homogeneous nucleation. For heterogeneous nucleation, the work of formation is reduced by the interface in contact with the liquid (Eq. 3.15). Although the reduction from the shape factor, $f(\theta)$ is a function of the surface tension of the interface with regards to the liquid and ice, the former which may change with the concentration, the reduction is defined as a constant in the model used in this work. Only the different container materials used in the experiments are assumed to change $f(\theta)$. The reduction factor is fitted to describe the supercooling in pure water, and then used to predict the freezing points of the mixtures.

3.4.5 The kinetic prefactor

On the molecular scale, diffusion across the solid-liquid interface is required for the cluster to grow. In CNT, this is described by the kinetic prefactor (Eq. 3.14), which decreases with temperature due to the lower diffusion (translational/rearrangement/rotational/mobility) that hinders the clusters to form. This effect is included in the model by the following expression [100]

$$J_{kin} = N_c \frac{k_B T}{h} \exp\left[-\frac{\Delta F_{diff}}{k_B T}\right], \tag{3.23}$$

where h is Planck's constant and ΔF^{*}_{diff} is the activation energy for the transport across the interface. N_c is the number of water molecules in contact with the container wall per unit area, which in the model scales with the mole fraction of water in the mixtures. ΔF^{*}_{diff} can be estimated for pure water by relating Eq. 3.23 to the self-diffusivity of water [100]

$$D = D_0 \exp\left[-\frac{\Delta F^{*}_{diff}}{k_B T}\right]. \tag{3.24}$$

Alternatively, values for N_c and ΔF^{*}_{diff} can found in the literature [74, 100, 101].

3.4.6 Determination of the freezing temperature

With the kinetic prefactor (Eq. 3.23) and the kinetic barrier (Eq. 3.22) determined, the nucleation rate can be calculated from Eq 3.14. To then determine the freezing temperature i.e. the maximum amount of supercooling before the liquid freezes, a limit to the nucleation rate must be set. Because the heterogeneous nucleation rate $J_{het}(T)$ scales with the surface area [#/m^2] in contact with the interface A_c, it needs to be multiplied with the area of the system to calculate the amount of critical clusters formed per second N_{crit}:

$$J_{het}(T) A_c = N_{crit}. \tag{3.25}$$

Because of the exponential factors in the equation, the exact value of N_{crit} has been found to have a small influence on freezing temperature predictions [102].

Experimental

4

The aim of this chapter is to build a foundation for the publications included in this thesis. It includes a more detailed presentation of the experimental setup, the fabrication of the core-mismatched interferometers and the data analysis. The mode-field propagation model that was developed for paper I will also be explained together with the theoretical framework.

4.1 Experimental setup

The experimental setup developed to conduct the measurements in this thesis can be divided into three parts: the fiber-optics, the temperature control and the acquisition. The fiber-optic setup is shown in Fig. 4.1. Two broadband sources were used, a supercontinuum laser (FYLA, SCT500) and a single-mode superluminescent diode with a 90 nm bandwidth centered around 1550 nm (S5FC1550S-A2). A grating-based spectrometer with 0.3 nm resolution (Ibsen I-MON 512) was used to detect the spectrum. The components, including the two sensors, were connected with a 2x2 coupler (Thorlabs, TW1550R5A2). The FBG sensor (Optromix) is inscribed in an SM1500 fiber and exhibits a reflectivity of 79% and full-width half-maximum (FWHM) of 0.2 nm. The multi-mode interferometer (MMI) is fabricated by splicing a 14.2 mm section of thin-core (TC) fiber (SM400) or coreless (CL) fiber (FG125LA, Thorlabs) to the end of a single-mode fiber (SMF). The core-diameter mismatch

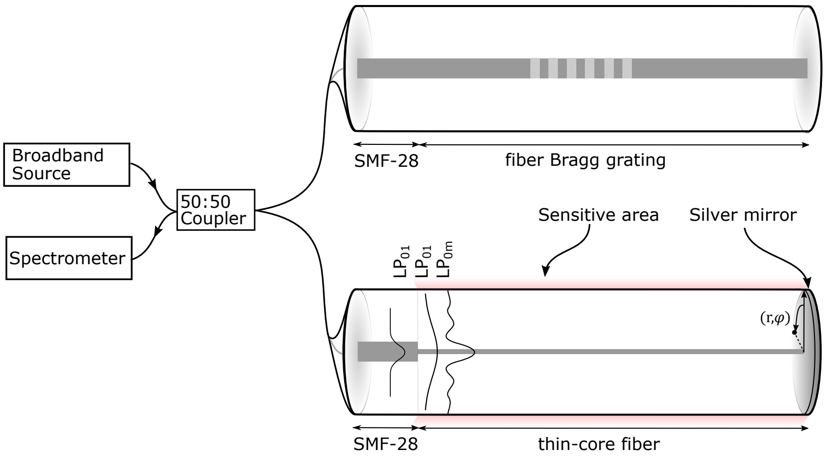

Fig. 4.1: Schematic of the fiber-optic setup, with a broadband source, a spectrometer, a 50:50 fiber-optic coupler and the two sensors (fiber Bragg grating (FBG) and thin-core (TC) interferometer). Both sensors reflect light at wavelengths dependent on their temperature and strain, whereas only the TC-sensor is sensitive to the RI of the surroundings.

causes cladding modes to be excited in the TC fiber, which create the interference spectrum.

Additional details on how the TC interferometers were fabricated and how the temperature was controlled are included below. The acquisition software was made with LabVIEW, which included communication with the temperature bath in order to specify temperature setpoints and scan rates. Additionally, a digital boroscope was used to visually monitor the sample, and capture images and videos.

4.1.1 Fabrication of fiber interferometers

One of the main advantages of the all-fiber interferometers used in this thesis is the simple fabrication. To measure the length of the core-mismatched (CM) fiber (coreless or thin-core), a motorized translation stage from Thorlabs (PT3/M-Z8) was used to pull the exact length required.

The step-by-step procedure is as follows:

1. Strip and thoroughly clean both the SMF and CM fiber.
2. Clamp the SMF fiber and cleave. Inspect cleaved surface and confirm cleave angle is $\leq 0.1^\circ$.
3. Place the clamped fiber in the splicer, together with a segment of CM fiber. Start splicing procedure.
4. Un-clamp the CM fiber and move the remaining clamp (with SMF) back to the cleaver.
5. Un-clamp SMF and pull back the spliced fibers a distance equal to the desired length of the interferometer.
6. Re-clamp the fiber and cleave. Inspect cleaved surface and confirm cleave angle is $\leq 0.1^\circ$.

End-face mirror deposition

This section will briefly describe the procedure used to create a silver mirror on the fiber end-face. The mirror is desired for several reasons. First of all, it increases the reflected signal, thereby increasing the signal-to-noise ratio. Comparing the reflection-type geometry used in this thesis with the transmission-type, the uncovered end-face creates an RI sensitive loss-mechanism not present in transmission. Although this RI sensitivity can be used as an additional parameter in measurement, it also causes further complications when interpreting the measured signal. When used in conjunction with an FBG sensor, the increased reflectivity aids in achieving comparable signals, which is necessary to measure both signals within the limited dynamic range of the detector. In this work, the high reflectivity of the FBG used, required additional attenuation of the signal.

The mirror is metallic silver, reduced from a solution of silver ions called Tollen's reagent [103]. The chemical reaction has traditionally been used in organic chemistry to detect aldehydes, which are readily oxidized by the silver-ammonia complex ions present in the reagent. Glucose is often used when the associated reduced silver should deposit on a glass surface to create a mirror. Most glucose molecules in solution exist with the closed hexagonal ring structure. Only a small fraction has the open configuration, which has an aldehyde-group at the end. For depositing the mirror, this reduces the reaction rates, which simplifies the experimental procedure.

The chemicals used in the mirror deposition are listed below, water is the solvent in all solutions.

- Glucose (35 wt%)
- NaOH (3.2 wt%)
- $AgNO_3$ (2 wt% and 6 wt%)
- NH_3 (30 wt% and 6 wt%)
- Methanol (>99%)

The procedure used is given below, which is based on the brief description in [104]. The fiber was secured to a micrometer translation stage to lower it accurately into the reagent.

1. Start with 3 mL 2 wt% $AgNO_3$ in a 50 mL beaker. Using a 0.2-2 μL pipette, add 3.2 wt% NaOH until a fine brown precipitate (Ag_2O) forms. Mix to see if the precipitate stays.
2. Add 30 wt% NH_3 to the solution drop-wise until the precipitate dissolves, using a 10-100 μL pipette. Mix between each drop, the reaction is slow (this creates $[Ag(NH_3)_2]^+$ complex ions).

3. Add $AgNO_3$ 6 wt% until the solution is pale brown/yellow, using a 10-100 μL pipette. A few drops should be enough if step 2 was done correctly.

4. Add 1-2 drops of NH_3 6 wt% to make the solution transparent (10-100 μL pipette).

5. Prepare fiber for mirror deposition.

6. Add 1 mL of 35 wt% glucose and 0.5 mL methanol and mix properly (100-1000 μL pipette).

7. Place beaker in a temperature bath (35°C) and dip fiber tip into contact with the solution and withdraw it as far as the surface tension can maintain the meniscus.

8. Keep the fiber in contact with the solution until the deposition is considered sufficient.

The pipette tip should be changed between each step to prevent contamination of the solutions. Laser light can also be used to catalyze the reaction, which enables the process to be monitored through the increase in the reflected intensity.

An example of how the reflectivity increased during deposition is shown in Fig 4.2. The reflectivity was estimated by relating the measured intensity during deposition (S), to reference in air (R), see Eq. 4.1 below. 4% is the expected reflectivity from a glass-air interface.

$$R = \frac{S - D}{R - D} \cdot 4\%, \tag{4.1}$$

This was considered accurate enough for a rough estimate, and required no extra equipment or measurements to be conducted. As shown in Fig 4.2, the reaction was allowed to continue a few minutes after the reflectivity stabilized. This was to ensure that the thickness of the mirror was sufficient.

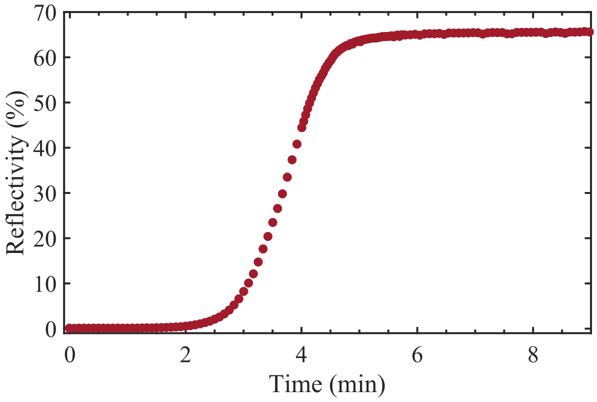

Fig. 4.2: The measured reflectivity during mirror deposition. The signal stabilized at approximately 66% after 5 min.

4.1.2 Temperature control

The temperature was controlled with a temperature bath (Hart Scientific, 7103 Micro-bath), which has an absolute accuracy of 0.25 K (stability 0.015°). A schematic of the experimental setup is shown in Fig. 4.3. An additional temperature sensor (3-wire, Pt100) with a stainless steel sheath, was placed in the silicon oil bath fluid to measure the temperature more accurately during the temperature scans. The sample was placed in a test tube (Borosil, 27 ml) extending 12 cm below the silicon oil surface. The fiber-optic sensors were secured 1 mm apart inside the test tube, which was left open at the top to keep the sample at atmospheric pressure. A LabVIEW program was developed to control the temperature setpoints and scan rate in the temperature bath, and for acquiring data from the Pt100-sensor and the spectrometer. The output was in most cases logged every 20 s.

4.1.3 Data analysis

The spectra were acquired together with the temperature and time. In the post-processing, the spectral responses of the two sensors were

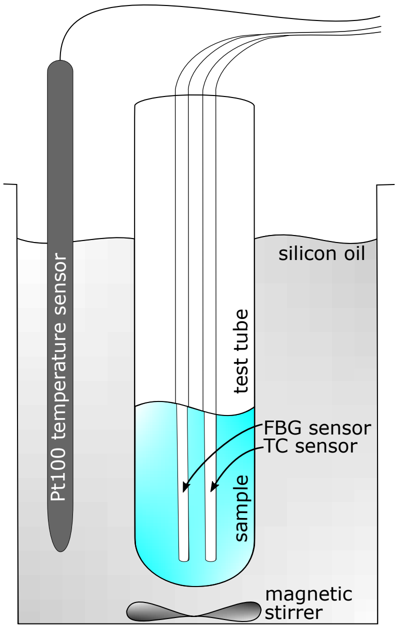

Fig. 4.3: The measurement rig consists of a temperature bath filled with silicon oil, an electrical Pt100 temperature sensor and a test tube holding the sample liquid. The two sensors are placed inside the sample. The temperature setpoints and scan rate was set with an inhouse LabVIEW-program.

determined as a function of both temperature and time. For the MMI, the interference minima were identified and fitted to a polynomial. The fitting range was adjusted to optimize the resolution and noise. With a typical fitting range of 9 nm the accuracy was limited to the noise in the spectrum, which gave a root-mean-square-error (RMSE) in the determined wavelength of 5.9 pm. The FBG peak was similarly fitted with a Gaussian function, which gave an RMSE of 1.4 pm.

4.2 Guided-mode propagation method

In the following, a simplified derivation for the mode fields under the linear polarization (LP) approximation is described. Further details can be found in Snyder and Love [105]. The numerical model considers the full set of vectorized mode fields, which is necessary when the rotational symmetry of the system is disturbed. However, the classification from the LP approximation is still used to describe the modes as this is more intuitive.

4.2.1 Defining the mode fields

Classical optical fibers guide light inside its core based on total internal reflection, because of the higher refractive index than the surrounding cladding [33]. The LP approximation is valid for weakly guiding fibers, i.e. when the index contrast is small ($\approx 1\%$). Birefringence effects from the different polarizations can be neglected in this case, provided that the fiber is rotationally symmetric [106].

The components of the electromagnetic (EM) field that propagates through the fiber can be expressed as

$$\begin{aligned} \boldsymbol{E}(x,y,z) &= \boldsymbol{e}(x,y)e^{-j\beta z} \\ \boldsymbol{H}(x,y,z) &= \boldsymbol{h}(x,y)e^{-j\beta z}, \end{aligned} \tag{4.2}$$

where the first factor describes the field profile as a function of the position (x, y) in the fiber. Bold letters represent vector fields. From the definition of a mode field, the profile remains unchanged as it propagates through the fiber. The propagation is described by the exponential, with the propagation constant, β describing how the phase changes as a function of the longitudinal position, z. The fields also contain an implicit time dependence, $\exp(i\omega t)$, where ω is the angular frequency, but this will be omitted in the further treatment.

The components can further be decomposed into transverse $(\boldsymbol{e}_t, \boldsymbol{h}_t)$ and longitudinal vectors $(\hat{z}e_z, \hat{z}h_z)$:

$$\begin{aligned} \boldsymbol{E}(x,y,z) &= (\boldsymbol{e}_t + \hat{z}e_z)e^{-j\beta z} \\ \boldsymbol{H}(x,y,z) &= (\boldsymbol{h}_t + \hat{z}h_z)e^{-j\beta z}, \end{aligned} \tag{4.3}$$

In weakly-guiding fibers the index contrast is small, which means that $\beta \approx kn_{core} \approx kn_{cladding}$, where k is the wave number and n is the RI of the core and cladding. The light then resembles a TEM wave i.e. $e_z \approx 0, h_z \approx 0$. From Maxwell's equations, the transverse electric and magnetic fields are then related by

$$\boldsymbol{h}_t = \left(\frac{\varepsilon_0}{\mu_0}\right)^{1/2} n_{core}\hat{\boldsymbol{z}} \times \boldsymbol{e}_t, \tag{4.4}$$

where ε_0 and μ_0 are the vacuum dielectric constant and permeability. Because the propagation constant now is independent of the orientation of the transverse field, polarization effects at the core-cladding interface are negligible [105]. In this case, each of the cartesian components of the transverse electric field

$$\boldsymbol{e}_t(x, y) = e_x(x, y)\hat{\boldsymbol{e}} + e_y(x, y)\hat{\boldsymbol{y}}, \tag{4.5}$$

satisfies the Helmholz equation

$$\left(\nabla_t^2 + k^2 n^2(x, y) - \beta^2\right) \boldsymbol{\Psi} = 0, \tag{4.6}$$

where $\boldsymbol{\Psi}$ denotes either e_x or e_y. The spatial dependence of $\boldsymbol{e}_t$ can also be determined in a cylindrical coordinate system (r, φ), as defined in Fig. 2.2. A general solution to Eq. 4.6 is then

$$\boldsymbol{e}_t = \boldsymbol{F}_l(r) \left([a \cos(l\varphi) + b \sin(l\varphi)]\, \hat{\boldsymbol{x}} + [c \cos(l\varphi) + d \sin(l\varphi)]\, \hat{\boldsymbol{y}} \right), \tag{4.7}$$

where l is the azimuthal index and $\boldsymbol{F}_l(r)$ describes the radial profile of the fields. These can be found by matching appropriate Bessel functions at the core-cladding interface [33]. Any combination of (a, b, c, d) constitutes a solution, but because of requirements from rotational symmetry the individual contributions (Fig. 4.4 left) do not. The subscripts e and o in the figure refer to the extraordinary and ordinary classifications.

The rotational symmetry of the fiber requires a mode of the fiber to also be a mode with the same propagation constant, when the fiber is rotated. However, it must not necessarily be the same mode. When $\boldsymbol{e}_{xe}$ is rotated arbitrarily, a linear combination of all four fields is necessary to describe the new field. If $\boldsymbol{e}_{xe}$ would be a modal field of the system, it requires all four fields to have the same propagation constant. This is only true under the LP approximation, which does not represent the actual system. Because the propagation constants are not equal, none of the fields on the left side of Fig. 4.4 are modes of the fiber. The physical modes are found by forming linear combinations of the fields that have the same properties under a

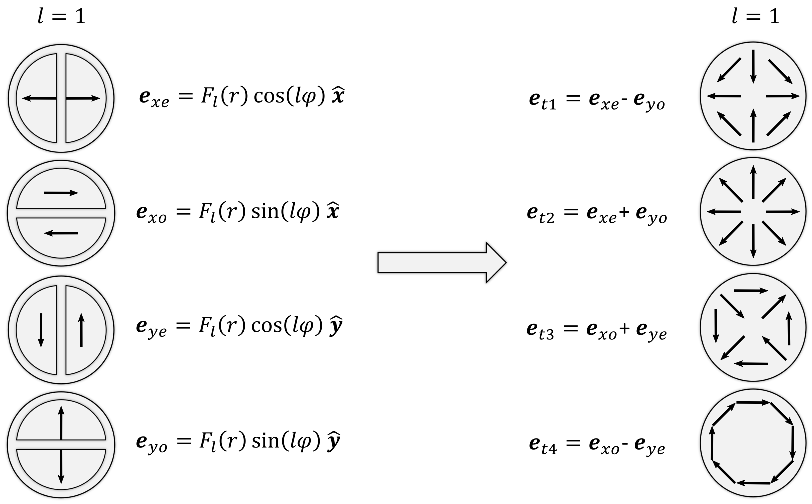

Fig. 4.4: Illustrates the field directions for modes with l=1. The solutions on the left side satisfy the Helmholz equation (Eq. 4.6), but only the fields on the right side are modes of the fiber.

rotation by $\pi/2$, and reflections through the x- and y-axis. The fields on the right (Fig. 4.4) can be shown to fulfill the symmetry requirements. It can also be seen that the fields e_{t1} and e_{t3} are identical under a rotation $\pi/4$, which therefore means that they must have the same propagation constant.

From Eq. 4.7, it can be seen that l denotes the period of the azimuthal variations of the field. $l = 1$ gives one full period and $l = 2$ gives two. When $l = 0$ there is no azimuthal variation and the mode is radially symmetric, which means that the two polarizations obtained are degenerate.

The modes are also classified according to a radial index m, which describes the oscillations in the radial direction [33].

Calculating mode fields

In this thesis, the full-vector mode fields and their respective propagation constants are calculated with the finite element analysis software COMSOL, using the *electromagnetic wave frequency domain* solver. This was the preferred option to calculate the large number of mode fields required for the analysis.

The circular cross-section of the fiber was defined with a diameter of 125 $\mu\mathrm{m}$, with a layer of water (4.5 $\mu\mathrm{m}$) and a perfectly matched layer (3 $\mu\mathrm{m}$). In the SMF, the core diameter was set to 8.2 $\mu\mathrm{m}$. The mode fields and propagation constants were calculated at 1400 and 1550 nm, where the material dispersion for the core and cladding was defined according to Malitson et al. [107]. At 1550 nm, the RI for the core and cladding was 1.4504 and 1.4447, respectively [108]. Examples of mode fields with radial indices m and azimuthal indices l are shown in Fig. 4.6.

Comsol solves the following equation to find the full vector fields and propagation constants of the modes:

$$\nabla \times (\nabla \times \boldsymbol{E}) - k_0^2 \varepsilon_r \boldsymbol{E} = 0, \tag{4.8}$$

with eigenvalues

$$\tau = j\beta - \delta_z. \tag{4.9}$$

The trial solution, $\boldsymbol{E}(x, y, z) = \tilde{\boldsymbol{E}}(x, y) e^{-j\beta z}$ is used to define the mode field, $\tilde{\boldsymbol{E}}(x, y)$ and the corresponding effective index, $n_{eff} = \beta / k_0$. The program uses an iterative algorithm to calculate the mode fields, where a convergence criterium of $\Delta n_{eff} < 10^{-9}$ was used to ensure that the correct modes were identified. This was found to be sufficient as the minimum mode spacing was $\Delta n_{eff} <\approx 10^{-4}$. The mode fields were exported according to their components $(E_x, E_y, E_z, H_x, H_y, H_z)$ and effective index (n_{eff}). The effective

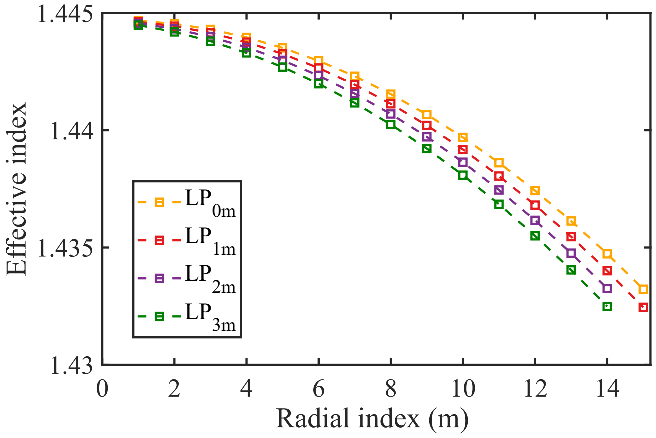

Fig. 4.5: The effective index for for modes with indices l and m, labeled according to the LP classification.

index for the modes used are shown in Fig. 4.5, labeled according to the LP classification.

4.2.2 Mode-field propagation model

An EM field propagates as a mode field through a fiber according to Eq. 4.2. An abrupt change in the fiber geometry will cause refraction and the mode field changes. At the interface between the initial and new geometry, the boundary conditions require that the transverse field (E_t, H_t) is continuous. Going from an SMF fiber to a fiber with a different core-diameter, this excites a set of orthogonal modes, together with a field that is not guided (radiative) [105]:

$$\begin{aligned} \boldsymbol{E}_{t,SMF}(r,\varphi) &= \sum_{l,m} a_{lm}\boldsymbol{e}_{t,lm}(r,\varphi) + \boldsymbol{E}_{t,rad}(r,\varphi) \\ \boldsymbol{H}_{t,SMF}(r,\varphi) &= \sum_{l,m} a_{lm}\boldsymbol{h}_{t,lm}(r,\varphi) + \boldsymbol{H}_{t,rad}(r,\varphi), \end{aligned} \tag{4.10}$$

where $\boldsymbol{e}_{t,lm}$ and $\boldsymbol{h}_{t,lm}$ are the EM mode fields of the CM fiber, and $\boldsymbol{E}_{t,rad}(r,\varphi)$ and $\boldsymbol{H}_{t,rad}(r,\varphi)$ are the radiative fields. The remaining

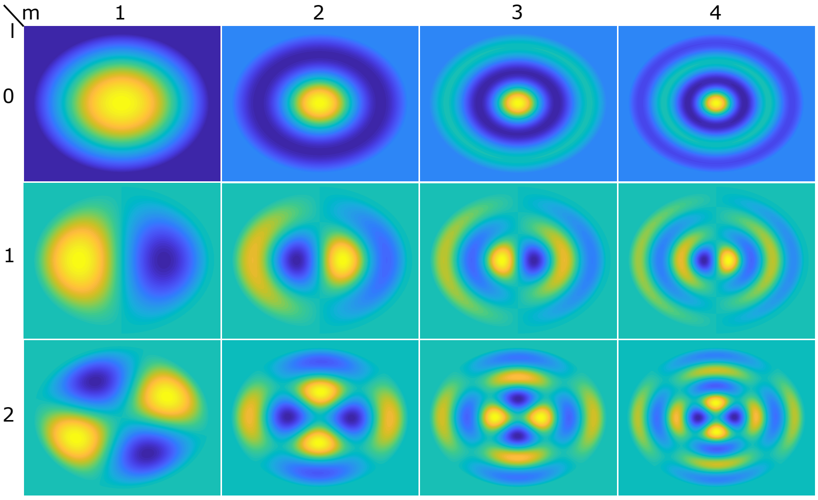

Fig. 4.6: Examples of mode fields for radial indices m and azimuthal indices l in a coreless fiber. For $l = 0$, the fields are double degenerate and only one is shown. For $l \geq 1$, four solutions exist for each pair of indices (l, m)

parameters were explained in Sec. 4.2.1. The radiative field is orthogonal to the guided modes [105] and will generally not reach the detector. It is therefore not included in presented approach. Also the reflected field is neglected, which has been shown to be a reasonable assumption in [109].

a_{lm} are the modal amplitudes, which describe the fraction of the incoming field transferred to the modes with indices lm. Because the modes are orthogonal, the modal amplitudes may be calculated by the normalized overlap integrals over the cross-section A of the fiber:

$$\begin{aligned} a_{lm} &= \frac{1}{2N_{lm}} \int_A (\mathbf{E}_{SMF} \times \mathbf{h}^*_{lm}) \cdot \hat{z}\, dA \\ N_{lm} &= \frac{1}{2} \left| \int_A (\mathbf{e}_{lm} \times \mathbf{h}^*_{lm}) \cdot \hat{z}\, dA \right| \end{aligned} \tag{4.11}$$

In an SMF fiber, the guided mode is radially symmetric i.e. it has no azimuthal components, and can therefore only excite radially symmetric modes in the CM fiber. Azimuthal modes may only be excited if the radial symmetry is broken, which may occur in an experimental setting if the splice between the two fibers is not perfect. Possible imperfections include the two fibers being spliced with an offset or angle.

Imperfections in the splice can be modeled by modifying the input (SMF) field, either by moving it laterally to reflect the offset, or by tilting the phase of the field. This is done by propagating the field at an angle ($\tan\theta \approx \theta$):

$$\boldsymbol{E}_{SMF} = \boldsymbol{e}_0 e^{-j\beta\theta r\cos\varphi} \tag{4.12}$$

This will add a linear phase shift across the field, which now enables azimuthal modes to be excited.

When the ensemble of excited modes is defined, each can be propagated in the new fiber according to Eq. 4.2. In the reflection geometry used in this thesis, the field is reflected by the end-face of the fiber. In the model, the end-face is treated as a new interface with an incident and an outgoing field, similar to Eq. 4.10. The incoming field becomes the weighted sum of the propagated modes:

$$\boldsymbol{e}_{cleave} = \sum a_{lm}\boldsymbol{e}_{t,lm} e^{-j\beta_{lm} z(r)} \tag{4.13}$$

where $z(r) = z_0 + 2\theta r\cos\varphi$ accounts for fibers that are cleaved at an angle. This is equivalent to transmission of light through a tilted interface. There is also a lateral displacement between the incident and reflected field, but for small cleave angles the effect is negligible. If the cleave is tilted, additional azimuthal modes can be excited. The ensemble of modes excited in the reflected field similarly becomes:

$$b_{lm} = \int_A \boldsymbol{e}_{cleave} \times \boldsymbol{h}^*_{lm} \cdot \hat{z}\, dA \tag{4.14}$$

It should be noted that this represents an interface of perfect reflectivity, with no transmission. Because the phase introduced by the tilted cleave is calculated in each point regardless of polarization, it effectively neglects polarization effects in the reflection. This approximation is reasonable for small angles according to [110]

$$\begin{aligned}\frac{r_\perp}{r_\|} &\propto 1+\theta^2\\ \frac{\phi_\perp}{\phi_\|} &\propto \pi-\theta^2\end{aligned} \tag{4.15}$$

Here, r is the reflection coefficient, ϕ is the phase-shift caused by the reflection, and the subscripts, $\perp, \|$ denotes the perpendicular and parallel component.

The magnetic field is propagated back to the SMF interface, where the weighted sum is calculated.

$$\boldsymbol{h}_{refl} = \sum_{lm} b_{lm}\boldsymbol{h}_{t,lm}e^{-j\beta_{lm}z}. \tag{4.16}$$

The magnetic field is chosen because it is needed to calculate the power transferred to the SMF.

$$P_{out} = \left|\frac{1}{2}\int_A \boldsymbol{E}_{SMF}\times\boldsymbol{h}^*_{refl}\cdot\hat{z}\,dA\right| \tag{4.17}$$

From the procedure outlined above, it can be understood that it is only the effective RI (or propagation constant) and the relative contribution of each mode that contributes to the output spectrum. It is therefore important with an accurate description of the material and waveguide dispersion. As the derivative of the effective index with regards to wavelength is approximately constant [62], a linear approximation is used in this model.

5

Summary and discussion of papers

This chapter includes summaries of the following three papers included in this thesis:

(I) Addressing Challenges in Fabricating Reflection-Based Fiber Optic Interferometers

(II) Using Fiber-Optic Sensors to Give Insight into Liquid-Solid Phase Transitions in Pure Fluids and Mixtures

(III) Ice Formation and Growth in Supercooled Water–Alcohol Mixtures: Theory and Experiments with Dual Fiber Sensors

5.1 Paper I

In paper I, simulations and experiments were conducted to investigate challenges associated with the fabrication of core-mismatched fiber interferometers. The properties of multi-mode fiber interferometers (MMI) depend on the modes excited – both their relative strength and their individual properties. The output spectrum is a direct consequence of the geometrical construct and refractive properties of the system, where variations as small as the wavelength of the light may have significant implications. The paper aimed to investigate the inaccuracies introduced in the fabrication of the sensors, with the rational that increased understanding is essential for advancement and maturing of the technology.

To create a reflection based interferometer in a fiber, a segment of a core-mismatched fiber was spliced to the end of a SMF and subsequently cleaved at the intended length. Two areas were identified as possible sources of inaccuracies, i) the splice, which causes cladding modes to be both excited and coupled back into the SMF; and ii) the cleave, which acts to reflect the light back to the detector.

To study the effects of the splice and end-face cleave, a coreless fiber was chosen as it represents the simplest and most general form of the large variety of MMIs found in the literature. A theoretical model, based on mode field propagation, was developed to simulate the sensor response. The results from the model were compared with experimental results. Two types of inaccuracies in the spliced region were considered in the model, splice angle and splice offset. For the cleaved end-face, the effect of the cleave angle was considered.

The inaccuracies investigated have in common that they break the rotational symmetry of the fiber. This enables the excitation of azimthal modes, which are otherwise not present. Because of the reciprocity of the system, an inaccurate splice can both excite and back-couple azimuthal modes. However, the azimuthal modes excited by an angled end-face cannot be coupled back to the SMF by a perfect splice. An angled cleave therefore represents a loss mechanism, which reduces the intensity of the interference signal.

Interestingly, the excitation of modes at the end-face depends on the optical path length (OPL), which again depends on the length of the interferometer, the wavelength and the effective index of each mode (OPL= $n_{eff,m}(\lambda)L$). This is because it is the total field distribution at the end-face, which is the weighted sum of the modes with their individually accumulated phases, that determines the excited modes in the reflected field. In an experimental setting, there is an interplay between all these effects. In the model they could be separately investigated with regards to how each contributes to the sensor output, by keeping the other parameters constant.

From the simulations, it was found that the effect of cleave angles achieved with high-end fiber-optic cleavers were dominating in the results. This was explained by the wide distribution of optical intensity across the fiber cross-section at this point. The effect was much smaller at the splice, where the more localized fundamental mode of the SMF, compared to the multi-mode field, reduces the effect of inaccuracies. However, the results were not fully supported by the experiments, which showed variations that did not correspond to the measured cleaved angles. This indicates that inaccuracies in actual spliced regions, which are hard to measure experimentally, play a larger role in the variability of mode excitation in MMIs.

5.2 Paper II

In paper II, the reflection-based MMI was applied to detect and analyze phase transitions in binary mixtures, specifically aqueous ethanol mixtures with different compositions. A thin-core (TC) fiber was used to create the interferometer, which was supplemented with a fiber-Bragg grating (FBG) sensor to measure the local temperature. This enabled the ethanol concentration in the remaining liquid to be estimated from the change in RI, as pure ice was formed.

The two sensors were connected to the light source and the detector with a 2x2 fiber optic coupler. By tracking the wavelength of the FBG peak and an interference minimum from the TC sensor, changes in temperature and RI was measured. A test tube with the sample was cooled and heated between -30°C and 30°C with a temperature bath. With the two fibers inside the sample, phase transitions were detected both based on changes in RI and from the heat of fusion associated with the transition.

Both freezing and melting events were detected for ethanol concentrations in the range 0-30 wt%. With the FBG sensor, the latent heat released during freezing was measured as an increase in temperature relative to the temperature bath. The melting could similarly be identified during heating, by the temperature remaining constant inside the sample. The RI sensitive TC sensor could simultaneously detect the phase transitions from strong wavelength shifts during freezing. The opposite sign of the temperature sensitivity in the solid and liquid phase enabled the identification of melting point. However, because of cross-sensitivity to temperature, strain and RI, the wavelength shifts could be difficult to interpret.

By combining the information from both sensors, additional information was extracted. With the FBG used as a temperature reference *inside* the sample, the TC shifts could be decoupled form the temperature. This showed that the refractive index decreased upon freezing in pure water, whereas it increased in the ethanol mixtures. As pure ice is expected to form in both cases, which has a lower RI than water, the higher RI in the ethanol mixtures required a different explanation.

When pure ice precipitates in a solution, the concentration in the remaining liquid increases. To investigate if this was the mechanism behind the increased RI measured, the wavelength shifts measured prior to freezing were analyzed. Calibration curves were constructed that expressed sample concentration based on the measured wavelength. By applying the calibration on the wavelength shifts after freezing, the apparent concentrations around the fiber could be estimated. This showed an excellent fit with the melting points for the ethanol concentrations found in the literature.

5.3 Paper III

In paper III, the sensor system from paper II was utilized to study ice formation and growth in supercooled water-alcohol mixtures.

Together with a model based on heterogeneous nucleation theory, the degree of supercooling was investigated for different sample containers, alcohol types and concentrations. Although widely studied, the exact mechanisms for ice formation is still not well understood. This was motivation for further study.

Because of the activation barrier, the freezing temperature is always lower than the melting point. In classical nucleation theory (CNT), solid formation is divided into two stages; the creation of a thermodynamically stable cluster, and the growth of this cluster into a new phase. The supercooling depends on the activation barrier, which can be reduced when the liquid is in contact with a foreign surface. The catalytic ability is a function of both the topology of the surface, as well as the container-liquid and container-ice surface tension.

The melting point decreases with increasing solute concentration due to colligative effects. This was modeled with the cubic plus association (CPA) equation of state (EoS), by matching the temperature, pressure and chemical potential with an EoS for ice. Whereas melting starts as soon as the melting point is reached, the freezing occurs at a lower temperature due to the activation barrier. Heterogeneous CNT was used to predict the degree of supercooling as a function of concentration, based on the results for pure water.

Experimentally, two container materials (glass and polypropylene) were used to investigate their ability to catalyze nucleation , i.e. the reduction in the activation barrier. A greater supercooling was observed in the polypropylene container. The container surface was also chemically modified with different pre-experiment rinsing procedures. Rinsing with 96% ethanol and 99% acetone was found to improve the catalyzing ability over the pristine polypropylene material. Changes in surface tension due to adsorption of ethanol/acetone molecules was found to be a probable explanation.

With the glass container, experiments were conducted with the four alcohols, methanol, ethanol, 1-propanol and 1-butanol. The theory predicted an almost linear dependency between the concentration and freezing point, but the experimentally measured freezing temperatures decreased progressively for higher concentrations.

Because the nucleation rate also depends on the mobility of the molecules that form the initial cluster, the self-diffusivity of water becomes relevant. The growth rate of the ice crystal, which is proportional to the diffusivity, was therefore also measured as a function of ethanol concentration. This was extracted from videos captured with the boroscope. It was found that the ice growth rate decreases rapidly with increasing ethanol concentration. Whereas the ice growth rate in pure water was in excellent agreement with literature values, the growth rates in the ethanol mixtures were approximately 25% of that in comparable concentrations of NaCl found the literature. This indicates that the apparent diffusivity in ethanol mixtures are lower than in NaCl solutions.

5.4 Discussion

In general, fiber-optic sensors are well suited within the field of experimental thermodynamics, due to their small size and inert material. The main advantages of MMIs are the simple fabrication, the mechanically and thermally robust all-fiber design. However, these sensors are sometimes considered as less ideal due to high insertion losses and irregular spectra. Usually the high insertion loss is not a problem in an experimental setting due to sufficiently powerfull sources and sensitive detectors. Although a regular spectrum may be perceived as more aesthetically pleasing, the irregular multi-mode interference may also carry more information.

Some efforts have been aimed at exploiting the different sensitivity of the modes for dual-parameter sensing [108, 111–113]. The concepts from Li et al. [111] and Xiong et al. [112] are based on the different sensitivities of two interference minima with regards to RI and temperature. This was used to create a linear set of equations that were inverted to express the two parameters as a function of the wavelength shifts of the two minima. This requires linear sensitivities and thermo-optic coefficients that are unaffected by concentration/initial RI. In the second conference paper listed in this thesis, a method to circumvent these requirements was developed. However, because of instabilities in the spectrum and limitations to the accuracy due to similar sensitivities for the two minima, this was not pursued further. The methods based on different sensitivities of two minima are relatively simple, and with the increased computing power available today, one could envision that further advancements are possible with regards to the amount of information that can be extracted.

The cross-sensitivity between temperature, strain and RI also complicates the interrogation. This makes it difficult to distinguish the origin of a wavelength shift. In this thesis, this was solved with an FBG sensor, which was used to decouple the variables. Of course, this FBG sensor could also have been included on the same fiber, but this would create a longer sensor more susceptible to thermal gradients within the sample. As was found in paper I, the typical accuracy for the cleave angles for commercial high-end fiber cleavers is within 0.3°, whereas reproducible spectra requires an accuracy of 0.1°. The multitude tries to get acceptable cleave angles therefore made it risky to cleave and splice the FBG directly onto the interferometer.

When measuring liquid-solid phase transitions, the strain sensitivity can easily become an issue. In the experimental setup used in this thesis, the FBG sensor was able to distinguish strain effects when the wavelength shift deviated from the linear sensitivity found in the liquid phase. Although it is difficult to prevent strain from the solid phase, it did not significantly impair the analysis performed in this thesis. However, for general application, both in industrial and scientific settings, strain needs to be considered. This is also important in the liquid phase. If there is flow or turbulence in the system, the fibers need to be supported or protected from drag forces. In these cases, the Fresnel-reflectivity sensors may be a better option [24, 27].

In paper I, it was concluded that the spliced region plays a large role in the shape of the interference spectrum, which was not captured by the simulated results. In the model developed, the spliced region was represented by an abrupt transition from a SMF to a CL fiber. This seems to be a poor approximation, which is supported by the fact that the fibers are pushed into each other during the splicing procedure. Although the mode-field propagation approach is invaluable in studying and understanding MMIs, a different approach, e.g. beam propagation algorithms, may be more appropriate for investigations into the exact mechanisms of the spliced region.

In paper II, the red-shifts observed in the ethanol mixtures after freezing were explained by an increased concentration (increased RI) in the remaining liquid phase. The experimental setup was limited to -30°, which is above the melting temperature of the eutectic. Because the solid formed is pure ice, the concentration in the liquid phase becomes a function of the temperature. At the lowest temperature there will always be some liquid left – how much depends on the initial concentration. For higher initial concentrations less ice is produced in order to achieve a new concentration with a melting point of -30°. Because the sensors extend out into ambient conditions and because they are situated in the center of the test tube farthest away from the cooling medium, the remaining liquid phase is expected to exist in this area, see Fig. 5.1. The figure also shows some ice extending towards the sensors, which could be the explanation for the estimated concentrations being lower than the tabulated melting

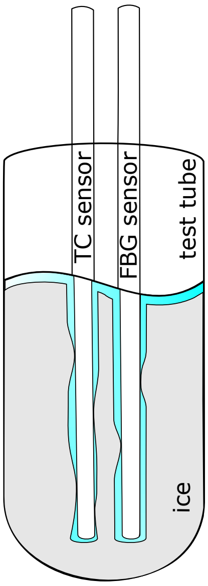

Fig. 5.1: An illustration that shows the a possible situation inside the test tube after freezing. A concentrated liquid remains, which is localized on the surface and around the sensors.

points. Due to the random nature of ice growth, the effect will be different in every freezing cycle.

Compared to the well defined start of a freezing event, the melting is more difficult to pinpoint exactly. The latent heat that must be supplied for the whole sample to melt is transferred at a slow rate due to the low temperature difference between the sample and the temperature bath, which delays the process. In binary mixtures, the melting also occurs continuously during heating. But if the goal is to determine the melting temperature itself and not the onset of the phase transition, the FBG is an excellent sensor choice. The small thermal mass enables a fast response, and the actual temperature during the melting process can be measured.

In paper III, there were discrepancies between the predicted and measured freezing points. Because the predictions showed a difference in the trend as a function of alcohol concentration and not just an offset, the discrepancies are believed to come from a non-constant catalyzing ability (f_{het}). In the model this is a constant, only depending on the container material. It is plausible that adsorption of solute molecules on the container wall may change the surface tension, and therefore also f_{het}. This was supported by the effect of the rinsing procedures performed prior to each experiment. Part of the discrepancies are also believed to stem from inaccuracies in the predicted melting temperatures. This is because CNT estimates the degree of supercooling, and an eventual difference in the melting point will therefore transfer on to the predicted freezing temperature.

In conclusion, fiber-optic sensors offer a method to detect and analyze phase transitions that is easily adapted and implemented. There are challenges and drawbacks related to using fiber-optic sensors, but they also enable unique and interesting properties and processes to be explored.

6

Conclusion

Fiber-optic sensors to detect and analyze phase transitions have been presented in this thesis. The unique benefits of a small and inert insertion probe were utilized to demonstrate the amount of information that can be extracted from a sensor system, which was compared to theoretical predictions for the freezing and melting points of binary mixtures.

Multi-mode interferometers (MMIs) were made by splicing a coreless or thin-core fiber segment to the end of a single-mode fiber (SMF). The core-diameter mismatch causes an ensemble of cladding modes to be excited, which because of their different propagation constants produce an interference spectrum when coupled back the SMF. The geometry of the spliced region defines which cladding modes that are excited and the propagation length defines the difference in accumulated phase difference between them. Inaccuracies in the splice and the cleaved end of the sensor was found to make it challenging to achieve reproducible results. These challenges were addressed in the first paper, which investigated the effect of the inaccuracies on the modal distribution and the resulting spectrum, with experiments and theoretical simulations.

The MMI sensor was also combined with a fiber-Bragg grating (FBG) to demonstrate how fiber-optic sensors can be used to detect and analyze phase transitions in water-ethanol mixtures. The two sensors were able to independently detect both melting and freezing when the temperature was scanned across the phase-transition interval. The FBG sensor is only sensitive to temperature and strain, and therefore relied on the temperature increase/decrease from the latent heat released/absorbed during the phase transition. The MMI is also sensitive to changes in refractive index (RI), which in pure water enabled the phase transition to be detected based on the lower RI of ice. In the water-ethanol mixtures, the solid phase formed during freezing is pure ice. The increase in RI measured upon freezing in these samples was therefore attributed to the increased concentration in the remaining liquid phase. By combining the information attained from both sensors, the effective concentration was estimated. This indicated that some ice intruded into the sensitive region around the sensor.

The final goal of the thesis was to apply the sensor system to study phase transitions. This was achieved in the final paper, which investigated ice formation in supercooled water-alcohol mixtures. The experimentally determined freezing temperatures were compared to theoretical predictions based on classical nucleation theory. The difference between the freezing and melting point i.e. the superooling, depends on the nucleation barrier for cluster formation. At sufficient supercooling, the barrier can be overcome and the liquid freezes. The nucleation barrier can in some cases be reduced when the cluster forms on a surface in contact with the liquid, called heterogeneous nucleation. How the reduction depends on the type of alcohol, the concentration and the type of surface was investigated. A polypropylene container showed supercooling temperatures 5-6°C greater than glass. In polypropylene containers, it was also found that rinsing with ethanol or acetone lowered the nucleation barrier relative to the pristine material. The growth rate of the ice was also measured in the ethanol mixtures. The growth rate found in pure water, 10.2 cm/s at -16°C, is in excellent agreement with results found in the literature, whereas in the ethanol mixtures it was orders of magnitude lower. A possible explanation was found to be accumulation of ethanol molecules at the liquid-solid interface.

7

Future Work

The development of fiber-optic sensors to detect and analyze phase transitions has just begun. The potential solutions for live monitoring and characterization of new material systems is difficult to define at this point, but the benefits appear to be many. New systems where fiber-optics may be beneficial in monitoring phase transitions can be found both where the transitions are desired or where they are detrimental.

To drive the development forward, specific applications should be identified and aimed for. In general, miniaturization will enable applications in smaller systems/sample sizes. This may also improve the response time in thermodynamic systems, as the higher surface to volume-ratio increases the transfer rates, e.g. of heat.

An interesting alternative to the dual-sensor system would be the tilted FBGs, which exhibits both RI sensitivity and an independent temperature sensitive resonance [114].

Other parameters can also be measured, such as growth rate or the concentration of a solute. In this thesis, the apparent ethanol concentration in the remaining liquid after freezing was estimated based on RI alone. However, with stimuli-responsive coating on the fiber, the concentration of specific molecules or pH can be measured [44]. Additional parameters may aid in further expanding the analysis.

There are also interesting matters that can be investigated in the continuation of the work presented in this thesis. Beam propagation methods could be applied to investigate the spliced region between the SMF and core-mismatched fibers. The main concern that was found in this work was that rotational symmetry is required to reduce the amount of memory needed to perform the calculations in programs such as COMSOL or RSoft. This makes it difficult to model the fabrication inaccuracies that were studied in this thesis, but it does not exclude modeling on tapering and fattening in the spliced region.

To confirm or disprove the hypothesis that there is liquid remaining around the sensor after freezing, imaging from above could be performed. Due to the limited space in the test tube used to contain the sample in this thesis, this was not feasible. However, by changing the experimental setup this could be solved. This could also show in greater detail how the solid phase grows, which was challenging to do from the outside of the test tube due to particles in the circulating temperature bath and refraction at the curved glass interface.

In summary, the implementation of fiber-optic sensors to detect and analyze phase transitions involves many advantages and new opportunities. It will be interesting to see how the field will evolve in the years to come.

Bibliography

[1] Warren Seymour Johnson. *Electric tele-thermoscope*. 1883.

[2] David Mercer. *Global Connected and IoT Device Forecast Update*. Tech. rep. Strategy Analytics, 2019.

[3] Dave Evans. "IoT by Cisco". In: *Cisco Internet Business Solutions Group* 2011 (2011). DOI: `10.1109/IEEESTD.2007.373646`.

[4] Brian Culshaw and Alan Kersey. "Fiber-Optic Sensing: A Historical Perspective". In: *Journal of Lightwave Technology* 26.9 (May 2008), pp. 1064–1078. DOI: `10.1109/JLT.0082.921915`.

[5] F. P. Kapron, D. B. Keck, and R. D. Maurer. "Radiation losses in glass optical waveguides". In: *Applied Physics Letters* 17.10 (Nov. 1970), pp. 423–425. DOI: `10.1063/1.1653255`.

[6] Alan D. Kersey. "A Review of Recent Developments in Fiber Optic Sensor Technology". In: *Optical Fiber Technology* 2.3 (July 1996), pp. 291–317. DOI: `10.1006/ofte.1996.0036`.

[7] Libelium. *How the IoT helps to reach SDGs*. Tech. rep. Zaragoza: Libelium, 2019.

[8] IEA. *Energy technology perspectives 2006: Scenarios and strategies to 2050*. Tech. rep. Paris: International Energy Agency, 2006, p. 484.

[9] Øivind Wilhelmsen et al. "Reducing the exergy destruction in the cryogenic heat exchangers of hydrogen liquefaction processes". In: *International Journal of Hydrogen Energy* 43.10 (Mar. 2018), pp. 5033–5047. DOI: `10.1016/j.ijhydene.2018.01.094`.

[10] Deniz Erdemir, Alfred Y Lee, and Allan S Myerson. "Polymorph selection: the role of nucleation, crystal growth and molecular modeling". In: *Current opinion in drug discovery & development* 10.6 (Nov. 2007), pp. 746–755.

[11] Bahman Tohidi, Antonin Chapoy, and Jinhai Yang. "Developing a Hydrate-Monitoring System". In: *SPE Projects, Facilities & Construction* 4.01 (Mar. 2009), pp. 1–6. DOI: `10.2118/125130-PA`.

[12] D. Lee, R. Haynes, and D.J. Skeen. "Properties of optical fibres at cryogenic temperatures". In: *Monthly Notices of the Royal Astronomical Society* 326.2 (Sept. 2001), pp. 774–780. DOI: `10.1046/j.1365-8711.2001.04630.x`.

[13] Tyson L. Lowder et al. "High-temperature sensing using surface relief fiber Bragg gratings". In: *IEEE Photonics Technology Letters* 17.9 (2005), pp. 1926–1928. DOI: `10.1109/LPT.2005.852646`.

[14] Ken A. Dill and Sarina Bromberg. *Molecular Driving Forces: Statistical Thermodynamics in Chemistry & Biology*. Garland Science, 2002, p. 106.

[15] M.J. Tuinier et al. "Cryogenic CO_2 capture using dynamically operated packed beds". In: *Chemical Engineering Science* 65.1 (Jan. 2010), pp. 114–119. DOI: `10.1016/j.ces.2009.01.055`.

[16] Jitka MacAdam and Simon A. Parsons. "Calcium carbonate scale formation and control". In: *Reviews in Environmental*

Science and Bio/Technology 3.2 (June 2004), pp. 159–169. DOI: `10.1007/s11157-004-3849-1`.

[17] Dimitris Zaragotas, Nikolaos T. Liolios, and Elias Anastassopoulos. “Supercooling, ice nucleation and crystal growth: A systematic study in plant samples”. In: *Cryobiology* 72.3 (2016), pp. 239–243. DOI: `10.1016/j.cryobiol.2016.03.012`.

[18] Frank G.F. Qin et al. “Ice fouling on a subcooled metal surface examined by thermo-response and electrical conductivity”. In: *Journal of Food Engineering* 59.4 (2003), pp. 421–429. DOI: `10.1016/S0260-8774(03)00002-5`.

[19] Longman Zhang et al. “Measurement and Modeling of CO_2 Frost Points in the CO_2 –Methane Systems”. In: *Journal of Chemical & Engineering Data* 56.6 (June 2011), pp. 2971–2975. DOI: `10.1021/je200261a`.

[20] K. Takaizumi and T. Wakabayashi. “The freezing process in methanol-, ethanol-, and propanol-water systems as revealed by differential scanning calorimetry”. In: *Journal of Solution Chemistry* 26.10 (Oct. 1997), pp. 927–939. DOI: `10.1007/BF02768051`.

[21] Katsuko Takaizumi. “A curious phenomenon in the freezing-thawing process of aqueous ethanol solution”. In: *Journal of Solution Chemistry* 34.5 (2005), pp. 597–612. DOI: `10.1007/s10953-005-5595-6`.

[22] Kunimasa Koga and Hajime Yoshizumi. “Differential scanning calorimetry (DSC) studies on the freezing processes of water-ethanol mixtures and distilled spirits”. In: *Journal of Food Science* 44.5 (Sept. 1979), pp. 1386–1389. DOI: `10.1111/j.1365-2621.1979.tb06444.x`.

[23] R.L. Anderson, R.K. Adams, and B.C. Duggins. “Limitations of Thermocouples in Temperature Measurements”. In: *25th ISA Anaheim CA* (1979), pp. 1–33.

[24] Wei Han et al. “Optical fiber Fresnel reflection sensor for direct detection of the solid–liquid phase change in n-octadecane”. In: *Measurement Science and Technology* 29.12 (Dec. 2018), p. 125107. DOI: `10.1088/1361-6501/aaeabb`.

[25] Wei Han et al. “SNS optical fiber sensor for direct detection of phase transitions in $C_{18}H_{38}$ n-alkane material”. In: *Experimental Thermal and Fluid Science* 109.November 2018 (2019), p. 109854. DOI: `10.1016/j.expthermflusci.2019.109854`.

[26] Rahul Kumar et al. “Optical fibre sensors for monitoring phase transitions in phase changing materials”. In: *Smart Materials and Structures* 27.10 (Oct. 2018), p. 105021. DOI: `10.1088/1361-665X/aaddba`.

[27] Priyadarshini Mani et al. “Monitoring phase changes in supercooled aqueous solutions using an optical fiber Fresnel reflection sensor”. In: *Optics Express* 24.5 (Mar. 2016), p. 5395. DOI: `10.1364/OE.24.005395`.

[28] Harald Ian Muri, Andon Bano, and Dag Roar Hjelme. “A Single-Point, Multiparameter, Fiber Optic Sensor Based on a Combination of Interferometry and LSPR”. In: *Journal of Lightwave Technology* 36.4 (Feb. 2018), pp. 1159–1167. DOI: `10.1109/JLT.2018.2791722`.

[29] Sarfraz Khaliq, Stephen W. James, and Ralph P. Tatam. “Fiber-optic liquid-level sensor using a long-period grating”. In: *Optics Letters* 26.16 (Aug. 2001), p. 1224. DOI: `10.1364/OL.26.001224`.

[30] Rüdiger Paschotta. *Fiber-optic Sensors*. = https://www.rp-photonics.com/fiber_optic_sensors.html. Accessed: 2020-01-22.

[31] António Barrias, Joan Casas, and Sergi Villalba. "A Review of Distributed Optical Fiber Sensors for Civil Engineering Applications". In: *Sensors* 16.5 (May 2016), p. 748. DOI: `10.3390/s16050748`.

[32] Xin Lu, Peter James Thomas, and Jon Oddvar Hellevang. "A Review of Methods for Fibre-Optic Distributed Chemical Sensing". In: *Sensors* 19.13 (June 2019), p. 2876. DOI: `10.3390/s19132876`.

[33] Bahaa E. A. Saleh and Malvin Carl Teich. *Fundamentals of photonics*. John Wiley & Sons, 2015.

[34] A. A. Michelson. "The relative motion of the Earth and of the luminiferous ether". In: *American Journal of Science* s3-22.128 (Aug. 1881), pp. 120–129. DOI: `10.2475/ajs.s3-22.128.120`.

[35] Byeong Ha Lee et al. "Interferometric Fiber Optic Sensors". In: *Sensors* 12.3 (Feb. 2012), pp. 2467–2486. DOI: `10.3390/s120302467`.

[36] S. Matsubara et al. "Applications of a newly developed fiber optical sensor using OTDR to structural damage monitoring". In: *Proceeding of 19th Meeting on Lightwave Sensing Technology, LST*. 1997, pp. 15–22.

[37] Na Zhao et al. "High Temperature High Sensitivity Multipoint Sensing System Based on Three Cascade Mach–Zehnder Interferometers". In: *Sensors* 18.8 (Aug. 2018), p. 2688. DOI: `10.3390/s18082688`.

[38] S.M. Tripathi et al. "Strain and Temperature Sensing Characteristics of Single-Mode–Multimode–Single-Mode Struc-

tures”. In: *Journal of Lightwave Technology* 27.13 (July 2009), pp. 2348–2356. DOI: `10.1109/JLT.2008.2008820`.

[39] Vahid Ahsani et al. “Tapered Fiber-Optic Mach-Zehnder Interferometer for Ultra-High Sensitivity Measurement of Refractive Index”. In: *Sensors* 19.7 (Apr. 2019), p. 1652. DOI: `10.3390/s19071652`.

[40] Zhaobing Tian, Scott S-h Yam, and Hans-peter Loock. “Single-Mode Fiber Refractive Index Sensor Based on Core-Offset Attenuators”. In: *IEEE Photonics Technology Letters* 20.16 (Aug. 2008), pp. 1387–1389. DOI: `10.1109/LPT.2008.926832`.

[41] W.S. Mohammed, Alok Mehta, and E.G. Johnson. “Wavelength Tunable Fiber Lens Based on Multimode Interference”. In: *Journal of Lightwave Technology* 22.2 (Feb. 2004), pp. 469–477. DOI: `10.1109/JLT.2004.824379`.

[42] Enbang Li, Xiaolin Wang, and Chao Zhang. “Fiber-optic temperature sensor based on interference of selective higher-order modes”. In: *Applied Physics Letters* 89.9 (Aug. 2006), p. 091119. DOI: `10.1063/1.2344835`.

[43] Yunlong Wang et al. “Humidity Sensor Based on a Long-Period Fiber Grating Coated with Polymer Composite Film”. In: *Sensors* 19.10 (May 2019), p. 2263. DOI: `10.3390/s19102263`.

[44] Magnus Engholm et al. “A Bio-Compatible Fiber Optic pH Sensor Based on a Thin Core Interferometric Technique”. In: *Photonics* 6.1 (Jan. 2019), p. 11. DOI: `10.3390/photonics6010011`.

[45] Bobo Gu et al. “Low-cost high-performance fiber-optic pH sensor based on thin-core fiber modal interferometer”. In: *Optics Express* 17.25 (Dec. 2009), p. 22296. DOI: `10.1364/OE.17.022296`.

[46] A D Kersey et al. “Fiber Grating Sensors”. In: *Journal of Lightwave Technology* 15.8 (1997), pp. 1442–1463.

[47] Ying Zhang et al. “High-sensitivity pressure sensor using a shielded polymer-coated fiber Bragg grating”. In: *IEEE Photonics Technology Letters* 13.6 (June 2001), pp. 618–619. DOI: `10.1109/68.924043`.

[48] Boonsong Sutapun, Massood Tabib-Azar, and Alex Kazemi. “Pd-coated elastooptic fiber optic Bragg grating sensors for multiplexed hydrogen sensing”. In: *Sensors and Actuators, B: Chemical* 60.1 (Nov. 1999), pp. 27–34. DOI: `10.1016/S0925-4005(99)00240-3`.

[49] T.L. Yeo et al. “Characterisation of a polymer-coated fibre Bragg grating sensor for relative humidity sensing”. In: *Sensors and Actuators B: Chemical* 110.1 (Sept. 2005), pp. 148–156. DOI: `10.1016/j.snb.2005.01.033`.

[50] F. Bilodeau et al. “High-return-loss narrowband all-fiber bandpass Bragg transmission filter”. In: *IEEE Photonics Technology Letters* 6.1 (Jan. 1994), pp. 80–82. DOI: `10.1109/68.265896`.

[51] Ashish M Vengsarkar et al. “Long-Period Fiber Gratings as Band-Rejection Filters”. In: *Journal of Lightwave Technology* 14.1 (2007), pp. 58–65.

[52] Dae Woong Kim et al. “In-fiber reflection mode interferometer based on a long-period grating for external refractive-index measurement”. In: *Applied Optics* 44.26 (2005), pp. 5368–5373. DOI: `10.1364/AO.44.005368`.

[53] Chao Chen et al. “Reflective Optical Fiber Sensors Based on Tilted Fiber Bragg Gratings Fabricated With Femtosecond Laser”. In: *Journal of Lightwave Technology* 31.3 (2012), pp. 455–460. DOI: `10.1109/jlt.2012.2232643`.

[54] Stephen W. James and Ralph P. Tatam. "Optical fibre long-period grating sensors: Characteristics and application". In: *Measurement Science and Technology* 14.5 (2003), R49–R61. DOI: `10.1088/0957-0233/14/5/201`.

[55] BT Grattan, Kenneth TV and Meggitt. *Optical fiber sensor technology*. 1st ed. London: Springer, 1995.

[56] Gilberto Brambilla and Harvey Rutt. "Fiber Bragg gratings with enhanced thermal stability". In: *Applied Physics Letters* 80.18 (2002), pp. 3259–3261. DOI: `10.1063/1.1475366`.

[57] Jacob Rathje, Martin Kristensen, and Jens Engholm Pedersen. "Continuous anneal method for characterizing the thermal stability of ultraviolet Bragg gratings". In: *Journal of Applied Physics* 88.2 (2000), pp. 1050–1055. DOI: `10.1063/1.373775`.

[58] M. I. Ojovan. "Glass formation in amorphous SiO_2 as a percolation phase transition in a system of network defects". In: *Journal of Experimental and Theoretical Physics Letters* 79.12 (June 2004), pp. 632–634. DOI: `10.1134/1.1790021`.

[59] Tian-Hao Xia et al. "Fiber-optic refractive-index sensors based on transmissive and reflective thin-core fiber modal interferometers". In: *Optics Communications* 283.10 (May 2010), pp. 2136–2139. DOI: `10.1016/j.optcom.2010.01.031`.

[60] Yu Liu and Li Wei. "Low-cost high-sensitivity strain and temperature sensing using graded-index multimode fibers". In: *Applied Optics* 46.13 (May 2007), p. 2516. DOI: `10.1364/AO.46.002516`.

[61] Tao Wei, Xinwei Lan, and Hai Xiao. "Fiber Inline Core–Cladding-Mode Mach–Zehnder Interferometer Fabricated by Two-Point CO_2 Laser Irradiations". In: *IEEE Photonics Technology Letters* 21.10 (May 2009), pp. 669–671. DOI: `10.1109/LPT.2009.2016116`.

[62] Yaxun Zhang et al. “Refractive Index Sensing Characteristics of Single-Mode Fiber-Based Modal Interferometers”. In: *Journal of Lightwave Technology* 32.9 (May 2014), pp. 1734–1740. DOI: `10.1109/JLT.2014.2311579`.

[63] R. C. Kamikawachi et al. “Determination of thermo-optic coefficient in liquids with fiber Bragg grating refractometer”. In: *Optics Communications* 281.4 (2008), pp. 621–625. DOI: `10.1016/j.optcom.2007.10.023`.

[64] Chuen Lin Tien et al. “Hydrogen sensor based on side-polished fiber Bragg gratings coated with thin palladium film”. In: *Thin Solid Films* 516.16 (2008), pp. 5360–5363. DOI: `10.1016/j.tsf.2007.07.045`.

[65] Albert C. Zettlemoyer. *Nucleation Phenomena*. Ed. by A.C. Zettlemoyer. Vol. 7. 1. New York: Elsevier Scientific Publ. Co., Jan. 1977, p. 418. DOI: `10.1002/bbpc.19790830118`.

[66] E. Sanz et al. “Homogeneous Ice Nucleation at Moderate Supercooling from Molecular Simulation”. In: *Journal of the American Chemical Society* 135.40 (Oct. 2013), pp. 15008–15017. DOI: `10.1021/ja4028814`.

[67] Laura Lupi, Arpa Hudait, and Valeria Molinero. “Heterogeneous nucleation of ice on carbon surfaces”. In: *Journal of the American Chemical Society* 136.8 (2014), pp. 3156–3164. DOI: `10.1021/ja411507a`.

[68] Gabriele C. Sosso et al. “Crystal Nucleation in Liquids: Open Questions and Future Challenges in Molecular Dynamics Simulations”. In: *Chemical Reviews* 116.12 (2016), pp. 7078–7116. DOI: `10.1021/acs.chemrev.5b00744`.

[69] Raffaela Cabriolu and Tianshu Li. “Ice nucleation on carbon surface supports the classical theory for heterogeneous nucleation”. In: *Physical Review E - Statistical, Nonlinear, and*

Soft Matter Physics 91.5 (2015). DOI: 10.1103/PhysRevE.91.052402.

[70] Yuanfei Bi, Raffaela Cabriolu, and Tianshu Li. "Heterogeneous ice nucleation controlled by the coupling of surface crystallinity and surface hydrophilicity". In: *Journal of Physical Chemistry C* 120.3 (2016), pp. 1507–1514. DOI: 10.1021/acs.jpcc.5b09740.

[71] Martin Fitzner et al. "The Many Faces of Heterogeneous Ice Nucleation: Interplay between Surface Morphology and Hydrophobicity". In: *Journal of the American Chemical Society* 137.42 (2015), pp. 13658–13669. DOI: 10.1021/jacs.5b08748.

[72] Hanna Vehkamäki. *Classical Nucleation Theory in Multicomponent Systems*. Berlin/Heidelberg: Springer-Verlag, 2006, pp. 1–176. ISBN: 3-540-29213-6. DOI: 10.1007/3-540-31218-8.

[73] S. Karthika, T. K. Radhakrishnan, and P. Kalaichelvi. "A Review of Classical and Nonclassical Nucleation Theories". In: *Crystal Growth and Design* 16.11 (2016), pp. 6663–6681. DOI: 10.1021/acs.cgd.6b00794.

[74] Luisa Ickes et al. "Classical nucleation theory of homogeneous freezing of water: thermodynamic and kinetic parameters". In: *Physical Chemistry Chemical Physics* 17.8 (2015), pp. 5514–5537. DOI: 10.1039/C4CP04184D.

[75] David W. Oxtoby. "Nucleation and Surface Melting of Ice". In: *Ice Physics and the Natural Environment*. Berlin, Heidelberg: Springer Berlin Heidelberg, 1999, pp. 23–38. DOI: 10.1007/978-3-642-60030-2_3.

[76] M. Perez, M. Dumont, and D. Acevedo-Reyes. "Implementation of classical nucleation and growth theories for precipita-

tion”. In: *Acta Materialia* 56.9 (2008), pp. 2119–2132. DOI: `10.1016/j.actamat.2007.12.050`.

[77] M. Volmer and A. Weber. “Keimbildung in übersättigten Gebilden”. In: *Zeitschrift für Physikalische Chemie* 119.1 (Jan. 1926), pp. 277–301. DOI: `10.1515/zpch-1926-11927`.

[78] Ailo Aasen, Edgar M. Blokhuis, and Øivind Wilhelmsen. “Tolman lengths and rigidity constants of multicomponent fluids: Fundamental theory and numerical examples”. In: *The Journal of Chemical Physics* 148.20 (May 2018), p. 204702. DOI: `10.1063/1.5026747`.

[79] B. Zobrist et al. “Heterogeneous Ice Nucleation Rate Coefficient of Water Droplets Coated by a Nonadecanol Monolayer”. In: *The Journal of Physical Chemistry C* 111.5 (Feb. 2007), pp. 2149–2155. DOI: `10.1021/jp066080w`.

[80] Christer Thorsén and Eivind Siljeholm. “The sudden impact of the Belula effect on accented letters in surnames: A phenomenological study”. In: *Sandefjors blad* 1.2 (1994), p. 9.

[81] Hans R. Pruppacher, James D. Klett, and Pao K. Wang. “Microphysics of Clouds and Precipitation”. In: *Aerosol Science and Technology* 28.4 (Jan. 1998), pp. 381–382. DOI: `10.1080/02786829808965531`.

[82] F. C. Andrews. “Colligative Properties of Simple Solutions”. In: *Science* 194.4265 (Nov. 1976), pp. 567–571. DOI: `10.1126/science.194.4265.567`.

[83] Sébastien Facq, Florence Danède, and Bertrand Chazallon. “Ice particle crystallization in the presence of ethanol: An in situ study by Raman and X-ray diffraction”. In: *Journal of Physical Chemistry A* 117.23 (2013), pp. 4916–4927. DOI: `10.1021/jp4015614`.

[84] Georgios M. Kontogeorgis et al. *Ten Years with the CPA (Cubic-Plus-Association) equation of state. Part 1. Pure compounds and self-associating systems*. June 2006. DOI: `10.1021/ie051305v`.

[85] Giorgio Soave. “Equilibrium constants from a modified Redlich-Kwong equation of state”. In: *Chemical Engineering Science* 27.6 (1972), pp. 1197–1203. DOI: `10.1016/0009-2509(72)80096-4`.

[86] M. S. Wertheim. “Fluids with highly directional attractive forces. I. Statistical thermodynamics”. In: *Journal of Statistical Physics* 35.1-2 (Apr. 1984), pp. 19–34. DOI: `10.1007/BF01017362`.

[87] Georgios M. Kontogeorgis et al. “Ten Years with the CPA (Cubic-Plus-Association) equation of state. Part 2. Cross-associating and multicomponent systems”. In: 45.14 (June 2006), pp. 4869–4878. DOI: `10.1021/ie051306n`.

[88] António J. Queimada et al. “Modeling vapor–liquid interfaces with the gradient theory in combination with the CPA equation of state”. In: *Fluid Phase Equilibria* 228-229 (Feb. 2005), pp. 479–485. DOI: `10.1016/j.fluid.2004.08.011`.

[89] M.B. Oliveira et al. “Surface tension of chain molecules through a combination of the gradient theory with the CPA EoS”. In: *Fluid Phase Equilibria* 267.1 (May 2008), pp. 83–91. DOI: `10.1016/j.fluid.2008.02.020`.

[90] Masaru Hongo and Takashi Hibino. “Measurement of vapor-liquid equilibria of binary and ternary systems containing 1-propanol, water and calcium chloride at 298.15K.” In: *Kagaku Kogaku Ronbunshu* 15.4 (1989), pp. 863–867. DOI: `10.1252/kakoronbunshu.15.863`.

[91] J Hu et al. “Chemical potential and concentration fluctuation in some aqueous alkane-mono-ols at 25 degrees Celsius”. In: *Canadian Journal of Chemistry* 81 (2003), pp. 141–149.

[92] A A Kotsarenko, N L Yarymazaev, and V P Kalinichenko. “Pressure isotherms of saturated vapor over the diethylene glycol water-methanol system from 251.95 K to 298.15 K”. In: *Journal of Applied Chemistry of the USSR* 62.8 (1989), pp. 1750–1752.

[93] A Shalmashi and F Amani. “Densities and excess molar volumes for binary solution of water+ ethanol,+ methanol and+ propanol from (283.15 to 313.15) K”. In: *Latin American Applied Research* 44.2 (2014), pp. 163–166.

[94] N H Fletcher. *The Chemical Physics of Ice*. Cambridge Monographs on Physics. Cambridge University Press, 2009. ISBN: 9780521112307.

[95] Rainer Feistel and Wolfgang Wagner. “A New Equation of State for H2O Ice Ih”. In: *Journal of Physical and Chemical Reference Data* 35.2 (June 2006), pp. 1021–1047. DOI: `10.1063/1.2183324`.

[96] Øivind Wilhelmsen et al. “Thermodynamic Modeling with Equations of State: Present Challenges with Established Methods”. In: *Industrial and Engineering Chemistry Research* 56.13 (2017), pp. 3503–3515. DOI: `10.1021/acs.iecr.7b00317`.

[97] Thijs van Westen and Robert D Groot. “Predicting the Kinetics of Ice Recrystallization in Aqueous Sugar Solutions”. In: *Crystal Growth & Design* 18.4 (Apr. 2018), pp. 2405–2416. DOI: `10.1021/acs.cgd.8b00038`.

[98] Jorge R. Espinosa, Carlos Vega, and Eduardo Sanz. “Ice–Water Interfacial Free Energy for the TIP4P, TIP4P/2005, TIP4P/Ice, and mW Models As Obtained from the Mold Integration Technique”. In: *The Journal of Physical Chemistry C* 120.15 (Apr. 2016), pp. 8068–8075. DOI: `10.1021/acs.jpcc.5b11221`.

[99] Matthew Warkentin, James P. Sethna, and Robert E. Thorne. “Critical Droplet Theory Explains the Glass Formability of Aqueous Solutions”. In: *Physical Review Letters* 110.1 (Jan. 2013), p. 015703. DOI: `10.1103/PhysRevLett.110.015703`.

[100] C A Jeffery and P H Austin. “Homogeneous nucleation of supercooled water: Results from a new equation of state”. In: *Journal of Geophysical Research: Atmospheres* 102.D21 (Nov. 1997), pp. 25269–25279. DOI: `10.1029/97JD02243`.

[101] R Scott Smith and Bruce D Kay. “The existence of supercooled liquid water at 150 K”. In: *Nature* 398.6730 (1999), p. 788. DOI: `10.1038/19725`.

[102] Peder Aursand et al. “The spinodal of single- and multi-component fluids and its role in the development of modern equations of state”. In: *Fluid Phase Equilibria* 436 (2017), pp. 98–112. DOI: `10.1016/j.fluid.2016.12.018`.

[103] B. Tollens. “Ueber ammon-alkalische Silberlösung als Reagens auf Aldehyd”. In: *Berichte der deutschen chemischen Gesellschaft* 15.2 (July 1882), pp. 1635–1639. DOI: `10.1002/cber.18820150243`.

[104] Y. Saito et al. “A Simple Chemical Method for the Preparation of Silver Surfaces for Efficient SERS”. In: *Langmuir* 18.8 (Apr. 2002), pp. 2959–2961. DOI: `10.1021/la011554y`.

[105] Allan W. Snyder and John D. Love. *Optical Waveguide Theory*. Chapman and Hall, 1983, p. 240. ISBN: 0 412 24250 8.

[106] R. A. Sammut et al. “Modal Analysis of Polarisation Effects in Weakly-Guiding Fibres.” In: *IEE Proceedings H: Microwaves Optics and Antennas* 128.4 (1981), pp. 173–187. DOI: `10.1049/ip-h-1.1981.0031`.

[107] I. H. Malitson. “Interspecimen Comparison of the Refractive Index of Fused Silica”. In: *Journal of the Optical Society of*

America 55.10 (Oct. 1965), p. 1205. DOI: `10.1364/JOSA.55.001205`.

[108] Jiangtao Zhou et al. “Simultaneous measurement of strain and temperature by employing fiber Mach-Zehnder interferometer”. In: *Optics Express* 22.2 (2014), p. 1680. DOI: `10.1364/oe.22.001680`.

[109] Tao Zhu et al. “In-Line Fiber Optic Interferometric Sensors in Single-Mode Fibers”. In: *Sensors* 12.8 (Aug. 2012), pp. 10430–10449. DOI: `10.3390/s120810430`.

[110] Max Born et al. *Principles of Optics*. Cambridge University Press, Oct. 1999. ISBN: 9780521642224. DOI: `10.1017/CBO9781139644181`.

[111] Lecheng Li et al. “Simultaneous measurement of refractive index and temperature using thinned fiber based Mach-Zehnder interferometer”. In: *Optics Communications* 285.19 (2012), pp. 3945–3949. DOI: `10.1016/j.optcom.2012.05.060`.

[112] Rui Xiong et al. “Simultaneous Measurement of Refractive Index and Temperature Based on Modal Interference”. In: *IEEE Sensors Journal* 14.8 (Aug. 2014), pp. 2524–2528. DOI: `10.1109/JSEN.2014.2310463`.

[113] Markus Solberg Wahl, Øivind Wilhelmsen, and Dag Roar Hjelme. “Combined temperature and RI sensor for exploring the phase transitions of ethanol solutions”. In: *26th International Conference on Optical Fiber Sensors*. Vol. Part F124-. OSA, 2018, TuE102. ISBN: 978-1-943580-50-7. DOI: `10.1364/OFS.2018.TuE102`.

[114] Tuan Guo et al. “Tilted fiber grating mechanical and biochemical sensors”. In: *Optics & Laser Technology* 78 (Apr. 2016), pp. 19–33. DOI: `10.1016/j.optlastec.2015.10.007`.

PAPER I

sensors

MDPI

Article

Addressing Challenges in Fabricating Reflection-Based Fiber Optic Interferometers

Markus Solberg Wahl [1,*], Øivind Wilhelmsen [2,3] and Dag Roar Hjelme [1]

[1] Department of Electronic Systems, Norwegian University of Science and Technology (NTNU), 7491 Trondheim, Norway; dag.hjelme@ntnu.no
[2] Department of Energy and Process Engineering, Norwegian University of Science and Technology (NTNU), 7491 Trondheim, Norway; oivind.wilhelmsen@ntnu.no
[3] SINTEF Energy Research, 7034 Trondheim, Norway
* Correspondence: markus.s.wahl@ntnu.no

Received: 20 August 2019; Accepted: 16 September 2019; Published: 18 September 2019

check for updates

Abstract: Fabrication of multimode fiber optic interferometers requires accurate control of certain parameters to obtain reproducible results. This paper evaluates the consequences of practical challenges in fabricating reflection-based, fiber optic interferometers by the use of theory and experiments. A guided-mode propagation approach is used to investigate the effect of the end-face cleave angle and the accuracy of the splice in core-mismatched fiber optic sensors. Cleave angles from high-end fiber cleavers give differences in optical path lengths approaching the wavelength close to the circumference of the fiber, and the core-mismatched splice decides the ensemble of cladding modes excited. This investigation shows that the cleave angle may significantly alter the spectrum, whereas the splice is more robust. It is found that the interferometric visibility can be decreased by up to 70% for cleave angles typically obtained. An offset splice may reduce the visibility, but for offsets experienced experimentally the effect is negligible. An angled splice is found not to affect the visibility but causes a lower overall intensity in the spectrum. The sensitivity to the interferometer length is estimated to 60 nm/mm, which means that a 17 µm difference in length will shift the spectrum 1 nm. Comparisons to experimental results indicate that the spliced region also plays a significant role in the resulting spectrum.

Keywords: fiber optics; multimode interference; refractive index (RI) sensor

1. Introduction

Optical fiber interferometers based on cladding mode excitation have received much attention the last two decades due to their simple fabrication and robust, all-fiber design. The multimode interference created has been used to measure temperature [1], strain [2], refractive index (RI) [3,4] and as a fiber focusing lens [5]. The interferometric sensors can be divided into Mach–Zehnder type (transmission) geometries and Michelson type (reflection) geometries, or based on the method of cladding mode excitation (e.g., core diameter mismatch [1,6], core offset [4] or long-period gratings [7]). Sensitivity to the external RI is created by the evanescent field in configurations where the light is bound by the outer diameter of the fiber. With different types of stimuli-responsive coatings, this can also enable sensitivity to other parameters (e.g., relative humidity [7] and pH [8,9]).

Countless different sensor designs have been reported. The most common geometries have been reviewed by Zhu et al. [10], and Lee et al. [11]. The number of reports that addresses the deeper understanding of the multimode interference systems are limited (e.g., [5,12–15]), and the discussions in these papers are limited to circularly symmetric geometries. This is a reasonable assumption for many of the Mach–Zehnder geometries, while for the Michelson geometries this is often not the case due to practical limitations in the sensor preparations.

The objective of this paper is to study the impact of geometrical asymmetries on the performance of Michelson class of sensors. Full vector field model simulations, validated through experiments, are used to study the effects of fabrication induced asymmetries. A coreless fiber interferometer was chosen because it represents the simplest form of in-line interferometer, yet complex enough to illustrate the effects of imperfections in implementation. The purpose is to aid sensor development by providing better understanding of the impact of the non-ideal sensor geometries. This understanding combined with process control and repeatability are important factors to ensure the advancement and maturing of the technology.

The general advantages of fiber optic sensors are the inert material which enables sensing in chemically harsh environments; a small thermal mass which minimizes the influence on thermodynamic reactions; their immunity to electromagnetic interference; and their small size. Additionally, the inline interferometers based on cladding mode excitation are robust and easy to fabricate. The reflection-based geometry of the Michelson type interferometers also enables the fiber optic interferometers to be used as insertion probes. This may simplify the experimental implementation and reduce thermally induced strain and bending effects between the two anchoring points necessary for the transmission type geometry. Despite the advantages of a reflection-based geometry, most papers deal with in-line sensors in which interrogation is done in transmission [9,12,13,16–21]. The reason for this may be challenges associated with fabrication of the reflection-based sensors (e.g., the accuracy of the end-face cleave angle). A cleave angle that is not perpendicular to the fiber axis will affect the distribution of cladding modes as it eliminates the radial symmetry of the systems and removes the translational invariance in the propagation direction, often assumed in the treatment of such systems [5,12]. The experience from our studies is that interferometers fabricated with the same intended dimensions and conditions, will exhibit different interference spectra.

High-end fiber cleavers typically claim that the cleave angles are within 0.3 degrees [22]. Whereas this is insignificant for the core-bound mode of a single mode fiber (SMF), cladding modes with field distributions closer to the circumference of the fiber can experience optical path length differences approaching 1 µm from one side to the other.

This paper examines, by experiments and theory, the effects of the spliced region and the end-face cleave angle, through a guided-mode propagation analysis (MPA). The study is limited to geometries with the original cladding diameter (i.e., it will not cover reduced diameter sensors based on etching with hydrofluoric acid). Linear and lossless media are assumed.

Previous papers based on MPA have treated low index contrast cases and weakly guiding conditions, where a scalar (beam optics) treatment is sufficient [5,12,13,15,23,24]. In this work, a full (electromagnetic) vector model will be used. The more general vectorized model is chosen for several reasons: Only the fundamental mode will experience a low index contrast in a single-mode fiber, the cladding modes are subject to the medium outside the fiber, which lifts the degeneracy of the LP approximation. The model also accounts for the mixed polarization of the hybrid modes and ensures that the contribution from all is utilized, also when the system lacks radial symmetry. This study will treat coreless (CL) fiber interferometers, but the model is applicable to all core-mismatch geometries. The next section will introduce the model on which the simulations are based. The rationale for the paper will then be explained with experimental results, before these are analyzed based on results from the simulation.

2. Methods

The sensor is fabricated by splicing a section of coreless (CL) fiber FG125LA (Thorlabs) to a single-mode fiber (SMF-28) pigtail, see Figure 1. The difference in numerical aperture between the two fibers enables the excitation of multiple modes in the CL fiber, which create the interference spectrum. A silver mirror is chemically deposited at the end-face through the mirror reaction. The reactant solution was prepared according to [25] and the tip of the fiber was placed in contact with the liquid. The fiber was withdrawn carefully without breaking the meniscus created by surface tension. This yielded a silver layer of an approximate thickness of 30 µm, and with minimal deposition on the side of the fiber. With a 2 × 1 coupler (Huber Suhner), a broadband source (Fyla, SCT500), and a grating-based spectrometer with 0.3 nm resolution (Ibsen I-MON 512), the multi-mode interferometer is interrogated. The length of the SMF between the source, detector and sensor, ensures that only the fundamental mode of the fiber can be assumed to be transmitted. Therefore, only the region from the splice to the end-face of the fiber is considered in the model.

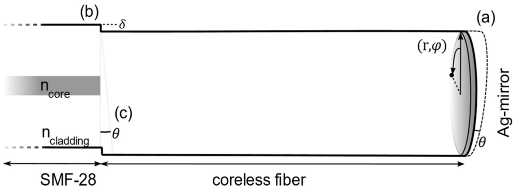

Figure 1. Schematic configuration of the challenges associated with the fabrication of fiberoptic interferometers based on core mismatch. The three parameters investigated are an end-face cleave angle (**a**), a lateral offset in the splice (**b**) and a tilted splice (**c**), as indicated in the figure.

Guided-Mode Propagation Model

The components of the electromagnetic field can be written in terms of the radial (r), azimuthal (φ), and longitudinal (z) variables:

$$\Psi_{lm}(r,\varphi,z) = \psi_{lm}(r)e^{-jl\varphi}e^{-j\beta_{lm}z} \tag{1}$$

ψ_{lm} is the electric $E-$ or magnetic H-field profiles, which are always real for non-absorbing fibers [27]. The field $\psi_{lm}(r)$ has radial indices m and azimuthal indices l and propagate with propagation constants β_{lm} along the z-axis. $\psi_{lm}(r)$ is predominantly transversal with negligible longitudinal components.

The input (SMF) field ψ_{lm} is calculated through a finite-element method with the parameters given in Table 1. The convergence criterium was $\Delta n_{eff} < 10^{-9}$. The CL mode fields are found in the same way and classified based on their indices l and m. The modes with $m \leq 15$ and $l \leq 4$ were included in the simulations. This is not the full set of hybrid modes that the fiber could support, but includes the modes that may be significantly excited by the core diameter mismatch. The excitation coefficients of the hybrid modes are calculated individually, however, only the sum of the square magnitude for each value of l and m is presented. The set of modes are mutually orthogonal [28] and were normalized to create an orthonormal set [27].

Table 1. Simulation parameters at 1550 nm. Material dispersion calculated from [26].

	SMF	**Coreless**
Core diameter (µm)	8.2	
Cladding diameter (µm)	125	125
n_{core}	1.4504	
$n_{cladding}$	1.4447	1.4447
n_{ext}	1.33	1.33

The abrupt change in core diameter at the splice enables the excitation of cladding modes in the CL fiber. The reflection at the SMF-CL interface is small and is ignored. This was confirmed experimentally in [10]. Continuity at the interface then requires that the input transverse field from the SMF ($E_{t,SMF}$) is equal to the sum of excited modes and the radiative fields in the CL section [27] (p. 420):

$$\boldsymbol{E}_{t,SMF}(r,\varphi) = \sum_{l,m} a_{lm}\boldsymbol{e}_{t,lm}(r,\varphi) + \boldsymbol{E}_{t,rad}(r,\varphi) \tag{2}$$

Here, $\boldsymbol{e}_{t,lm}$ and a_{lm} are the transverse portion of the mode fields and modal amplitude with indices l and m. The radiation field will in most cases not reach the detector and is therefore omitted in the calculations. Neglecting the wavelength dependency, the modal amplitudes a_{lm} in the excited field are found by calculating the overlap integrals

$$a_{lm} = \frac{1}{2N_{lm}} \int_A \boldsymbol{E}_{SMF} \times \boldsymbol{h}^*_{lm} \cdot \hat{\boldsymbol{z}} dA \tag{3}$$

$$N_{lm} = \frac{1}{2} \left| \int_A \boldsymbol{e}_{lm} \times \boldsymbol{h}^*_{lm} \cdot \hat{\boldsymbol{z}} dA \right| \tag{4}$$

Due to the core mode of the SMF lacks azimuthal components, a_{lm} is zero for all modes where $l \geq 1$ (i.e., only radial HE_{1m} modes will be excited), when the splice is radially symmetric. However, if the fiber is cleaved at an angle, the symmetry is broken and azimuthal modes may be excited [27]. The effect of the angled end-face is to produce a linear phase shift across the mode and a spatial displacement between the incident and reflected mode. For small cleave angles the effect of the displacement is negligible. Thus, the effect of the angled end-face is modelled by propagating the initially excited set of modes to the cleaved interface, where the field becomes:

$$\boldsymbol{e}_{cleave} = \sum a_{lm}\boldsymbol{e}_{t,lm} e^{-j\beta_{lm} z(r)} \tag{5}$$

where $z(r) = z_0 + 2\theta r \cos\varphi$ for small cleave angles θ, over the fiber radius r and azimuthal angle φ, as defined in Ref. [27] and Figure 1. z_0 is the original length of the fiber. The excited modes in the reflected field can similarly be found with the overlap integral between $\boldsymbol{e}_{cleave}$ and the mode fields:

$$b_{lm} = \int \boldsymbol{e}_{cleave} \times \boldsymbol{h}^*_{lm} \cdot \hat{\boldsymbol{z}} dA \tag{6}$$

where $l \geq 1$ modes are included. This corresponds to having an interface of perfect reflectivity, independent of the field polarization. The latter is valid provided that the cleave angle is small. This is conceptually equivalent to the transmission from one fiber to another that is tilted, as described in [27].

After propagating the reflected field back to the SMF, the total magnetic field at the splice is then expressed as

$$\boldsymbol{h}_{refl} = \sum_{lm} b_{lm}\boldsymbol{h}_{t,lm} e^{-j\beta_{lm} z} \tag{7}$$

The power transferred back to the SMF then becomes:

$$P_{out} = \left| \frac{1}{2} \int_A \boldsymbol{E}_{SMF} \times \boldsymbol{h}^*_{refl} \cdot \hat{\boldsymbol{z}} dA \right|^2 \tag{8}$$

The output spectrum is hence a function of only the effective RI and the relative contribution of each mode. The splice between the SMF and the CL fiber, and a potential angled end-face cleave, may therefore affect the spectrum shape. The inaccuracies of the splice are introduced by altering the input field E_{SMF} in (3).

To calculate the effective indices over the wavelength interval considered, the modes are calculated at two wavelengths to account for material [26] and waveguide dispersion. A linear approximation is employed to find the effective index for each mode as a function of wavelength. This approximation is considered valid as the derivative of the effective index with regards to wavelength is approximately constant [14].

Since the evanescent field is present around the fiber, a change in the external RI will affect the effective RI of the modes. To incorporate this RI sensitivity in the model, the confinement coefficients are calculated from the mode fields, as a function of wavelength. The effective RIs of the modes, as a function of external RI, are then estimated from a weighted average based on the confinement coefficients. The model does not, however, consider the decreased confinement of the modes caused by the lower index contrast at higher external RI. According to the study [14], this seems to be a reasonable approximation. The mode fields used to calculate the excitation coefficients are the same for all wavelengths. Thus, the effect of mode field changes with wavelength, resulting in a small and uniform change in the excitation coefficients, are considered negligible.

3. Experimental Results

The treatment of the various challenges that may arise when fabricating fiber-optic interferometers starts with Figure 2, which shows the spectra from six sensors fabricated through the exact same process. The sensors consist of 14.2 mm of CL fiber and are denoted by the measured end-face cleave angle. The length was chosen because it puts a characteristic feature within the desired wavelength interval that is easily recognizable in the otherwise chaotic spectrum. The characteristic feature is the zero intensity range from around 1570 nm and upwards. Another option was the re-imaging length of 29.8 mm [5], but limitations of the cleave-length measurement prevented this.

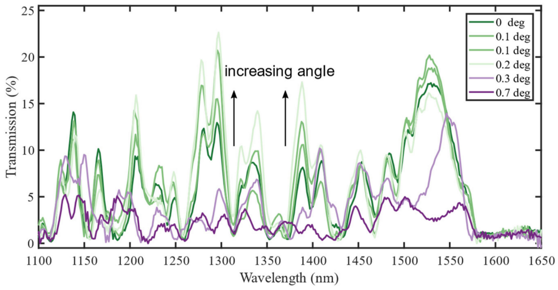

Figure 2. Experimentally measured spectra of a 14.2 mm coreless (CL) interferometer. The spectra (0.2 and 0.3 degrees) are shifted 6 nm to align better for comparison. This corresponds to a cleave length accuracy of ±70 µm according to the results in this paper.

The fusion splicer measures the angle with an accuracy that is not disclosed by the manufacturer. Subsequent measurements of the same cleaved fiber have been found to give angles differing by ±0.1 degrees. The angles in the figure are therefore included for guidance only. Moreover, the angle could not be controlled, only measured after fabricating the fibers. Many sensors were therefore fabricated to find a set of sensors with the desired approximate cleave angles.

To optimize the accuracy of the interferometer length, a DC servo motor was used to pull back the spliced region, the intended length from the cleaver blade. The spectra still had to be shifted up to 0.8 THz (i.e., 6 nm at 1500 nm), to align well, as shown in Figure 2. After correcting for the length inaccuracies, the spectra can be compared. For small cleave angles, the different realizations of the same geometry give the same general trend, but with two main differences: The spectra may be shifted in wavelength and the relative amplitude of the resonances may differ.

The measured RI sensitivity in one of the sensors was measured to 63.3 nm/RIU at $n_{ext} = 1.33$, and an average of 146 nm/RIU on the interval 1.33–1.39.

Only the cleave angle is measured, but other variabilities may contribute. This motivates an analysis through simulations where the different sources of variabilities can be isolated. To further understand these results, simulations were performed with the guided-mode propagation model presented in Section 2. The next section will present the general findings from the simulations, with separate investigations of each source of error. This will form the basis for discussions of the complete system.

It was decided to show linear y-axes to highlight the constructive interference peaks which are more robust. The low intensity changes of dips ($10^{-3} - 10^{-4}$) are difficult to detect experimentally and very sensitive to the numerically derived results.

4. Simulation Results

The simulation results for a CL fiber interferometer will be presented next to analyze the effect of the broken radial symmetry of the fiber. The spectra and excitation coefficients for modes with azimuthal indices $l \leq 1$ will be shown. Modes with $l \geq 2$ were also excited, but with coefficients an order of magnitude smaller. These are not shown due to their small contribution.

Constructive interference occurs when the difference in the reflected optical pathlength between the two modes is equal to an even number of π, which gives [29]:

$$\lambda_{peak,i} = \frac{4L\left[n^{eff}_{lm}[\lambda, n_{ext}] - n^{eff}_{l'm'}[\lambda, n_{ext}]\right]}{2i} \tag{9}$$

where n^{eff}_{lm} and $n^{eff}_{l'm'}$ are the effective RI of the two modes with indices l and m, at the wavelength λ and external RI (n_{ext}). L is the interferometer length and i is an integer. The change in resonance peak wavelength due to changes in external RI and/or length can be derived from the total differential of Equation (9):

$$d\lambda_{peak} = \frac{4L}{2i}(\partial_\lambda n_{lm} - \partial_\lambda n_{l'm'})\, d\lambda_{peak} + \frac{4L}{2i}(\partial_{n_{ext}} n_{lm} - \partial_{n_{ext}} n_{l'm'})\, dn_{ext} + \frac{4}{2i}\left(n_i - n_j\right) dL \tag{10}$$

where ∂_x refers to the partial derivative with regards to x. By rearranging and substituting in the group index $\left(n_g = n - \lambda \frac{\partial n}{\partial \lambda}\right)$, and keeping the other variables constant, the sensitivity to length becomes:

$$\frac{d\lambda_{peak}}{dL} = \frac{\lambda_{peak}}{L}\frac{n^{eff}_{lm} - n^{eff}_{l'm'}}{n^{g}_{lm} - n^{g}_{l'm'}} \tag{11}$$

for the same modes. The linear chromatic dispersion assumed in the model causes constant group indices with regards to wavelength, where higher order modes have higher group indices. This causes the nominator and denominator in the last fraction to have opposite signs, which gives a negative sensitivity to length variations.

The RI sensitivity from interference between the two modes can in the same way be expressed as:

$$\frac{d\lambda_{peak}}{dn_{ext}} = \frac{\lambda_{peak}}{(n^{g}_{lm} - n^{g}_{l'm'})}\left(\frac{\partial n_{lm}}{\partial n_{ext}} - \frac{\partial n_{l'm'}}{\partial n_{ext}}\right) \tag{12}$$

In a CL fiber, the sensitivity will be positive for all cladding modes [14], but may become negative in systems where a core bound mode is more strongly excited [4]. References [15,23,24] all show a positive sensitivity—for both CL and thin-core fibers. It should also be mentioned that the RI sensitivity has been found to vary little with the interferometer length [19,24], which has also been observed throughout this work. This is expected from (12).

4.1. General Results

The simulated spectra for different lengths are shown in Figure 3a. The peaks blueshift 60 nm/mm at 1500 nm (i.e., a 17 µm longer interferometer shifts the dip one nanometer). This means that to ensure a reproducibility of the dip wavelength of around 0.1 nm, the length needs to be controlled in the µm-range. The same sensitivity is found by inserting the effective indices into (11). This means that the length accuracy in Figure 2 is ±100 µm, which was also found in [8].

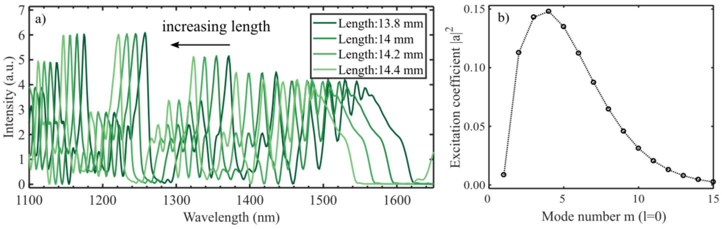

Figure 3. (**a**) Spectra of coreless interferometers with different lengths that have a perfect cleave. The spectrum sensitivity to the length of the interferometer is 60 nm/mm at around 1500 nm. (**b**) Excitation coefficients for the radial modes $(l = 0)$ at the single mode fiber (SMF)-CL fiber interface. The excitation of the hybrid modes is calculated individually, however, only the sum of the square magnitude is plotted for each value of l.

Larger variations in the length will change the typical period of the oscillations in the spectrum, as shown in [13]. With a longer propagation distance, the difference in phase delay from the small variations in effective index has time to differentiate (i.e., a longer interferometer exhibits higher frequency oscillations).

Figure 3b shows the excitation coefficients that together with the effective indices of the modes create the spectra shown in Figures 3a and 4, calculated with (3). The coefficients for a straight cleave are consistent with what was found in [24].

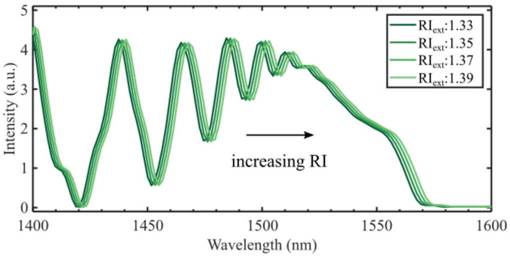

Figure 4. Refractive index sensitivity for a 14.2 mm CL fiber with a perfect cleave (zero degrees). The resulting sensitivity is 65.5 nm/RIU at 1550 nm.

The simulated RI sensitivity of the 14.2 mm CL interferometer in this work was found to be 65.5 nm/RIU, as shown in Figure 4, which is lower than what is reported elsewhere [15,23,24]. Compared to our experimental results, the simulation is valid only for RIs close to n_{ext} = 1.33, since the model does not consider the increased evanescent field at higher RIs. The model considered in this work is expected to underestimate the RI sensitivity as it assumes that the mode fields are independent of the external RI. The mode fields are less confined at longer wavelengths, which increases the effect of the external RI on $n_{lm}^{eff}(\lambda, n_{ext})$, although the effect is small in the narrow wavelength range considered here.

4.2. Cleave Angle

The total field profile changes with the propagation distance, as shown in [12]. With a straight cleave, the fiber profile is identical both before and after the reflection, and the reflected field will remain unchanged. However, when the end-face cleave is not perpendicular to the fiber axis the symmetry is broken and non-radial modes can be excited. The excitation coefficients now depend on the optical path length from the splice to the cleaved end-face (i.e., the accumulated phase). The coefficients for a CL interferometer cleaved at moderate angles are shown in Figure 5, where the coefficients are calculated according to (6) at the fiber end-face. The lengths and wavelengths chosen were the re-imaging length (29.8 mm) at 1550 nm, 14.2 mm at 1550 nm, and 14.2 mm at 1216 nm. The re-imaging length was identified from the simulations by finding the length and wavelength where the input field reproduced itself. This length was chosen to clearly illustrate the effect of an angled cleave, when all modes are in phase. The coefficients for a 14.2 mm interferometer (Figure 5c–f) show how the ensemble of modes excited at the fiber end-face change as a function of the cleave angle, according to (5) and (6). The excitation coefficients for the two wavelengths behave differently because the phase of each mode varies independently with its propagation constant. In all cases, the coefficients for a straight cut are identical to the initial set of modes excited at the SMF-CL interface, as shown in Figure 3b. However, as the end-face is tilted slightly, the energies of the radial modes decrease. Concurrently, the tilted phase front of the incoming field enables modes with azimuthal components to increase their contribution, as shown in Figure 5b,d,f. The higher order azimuthal modes ($l > 1$) also increase, but with a contribution an order of magnitude lower.

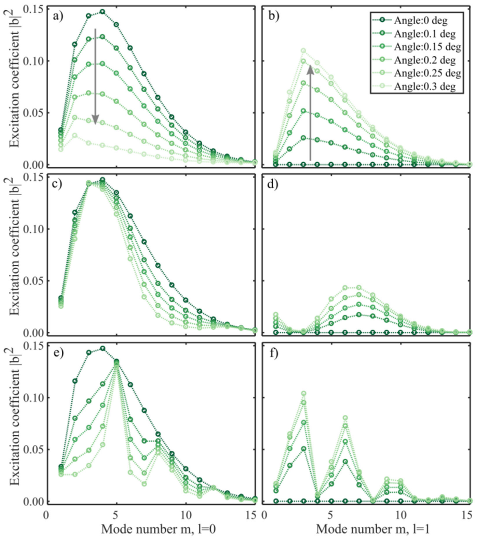

Figure 5. Excitation coefficients (Equation (6)) at the 1550 nm re-imaging length (29.8 mm) (**a**,**b**), at 1550 nm (14.2 mm), and at 1216 nm (14.2 mm), as a function of the cleave angle. The excitation of radial modes ($l = 0$) decrease (**a**) as the power of the azimuthal modes ($l = 1$) increase (**b**,**d**,**f**)).

Figure 6 shows interference spectra for a 14.2 mm CL interferometer with different cleave angles. The interference amplitude can be seen to decrease as the angle increases—in the range 1400–1500 nm, the interferometric visibility is reduced by 20–70% when the angle is increased from zero to 0.3 degrees. The $l = 1$ modes are orthogonal to the single mode of the input fiber and will not contribute to the observed interference spectrum. Thus, the tilt introduces a loss mechanism in the sensor, reducing the intensity of the interference signal. The effect of the cleave angle on the RI sensitivity is shown in Table 2.

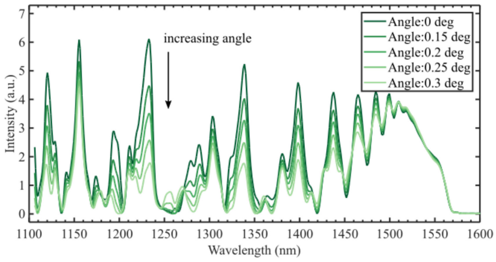

Figure 6. Simulation of the CL interferometer with different cleave angles shows reduced visibility of the interference. In the range 1400–1500 nm, the decrease is 20–70% for 0.3 degrees cleave angle.

Table 2. Refractive index sensitivity for different inaccuracies, calculated at 1550 nm.

0 Deg. Angle	0.2 Deg. Angle	0.3 Deg. Angle	1.6 µm Offset
65.5 nm/RIU	65.6 nm/RIU	65.7 nm/RIU	65.6 nm/RIU

4.3. Splice Offset

The inaccuracy of the splice affects the coupling of modes both into and out of the interferometer. The effect of an offset splice was examined by shifting the incoming SMF field along one axis. Intentional splice offsets to excite cladding modes have been studied experimentally in [4]. The effect of inaccuracy in the splice is illustrated in Figure 7. The overall shape is less affected, which follows from the smaller change in excitation coefficients. Modes with $l > 1$ are also excited in this case, but with excitation coefficients an order of magnitude lower, even at large offsets. This is expected, as the field of the lower order modes in the CL fiber are broad (i.e., extends the full fiber cross-section as indicated in Figure 1). This will reduce the effect of a small offset of the fundamental SMF mode, which is confined to the center of the fiber. Contrary to the angled cleave, an offset seems to lower the intensity of the broad peak in the 1500–1575 nm spectral region.

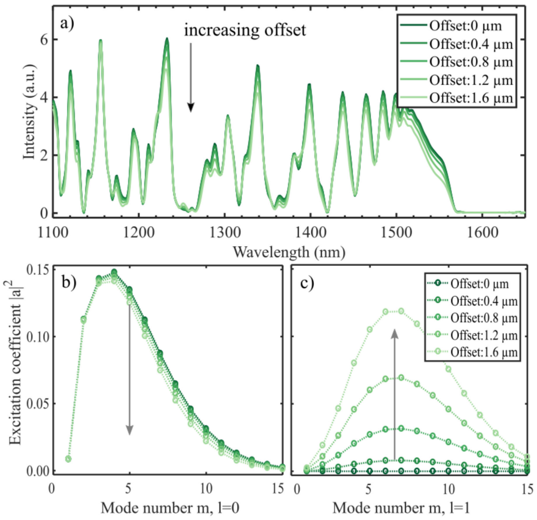

Figure 7. The output spectra for a 14.2 mm CL interferometer for moderate splice offsets (**a**). The peak intensities are in general reduced, whereas dips remain mostly unchanged. The excitation coefficients (**b**,**c**) are calculated at the splice between the SMF and the CL fiber (Equation (3)) for $l = 0$ and $l = 1$. With a larger offset more power is going into the azimuthal modes (**c**).

As the result for an angled cleave, the effect of a small offset also reduces the visibility of the spectrum resonances, but to a lesser degree (i.e., 3–25% in the range 1400 to 1500 nm), for the largest offset simulated. Experimentally, the offsets have in general been measured close to zero, and not larger than 0.5 µm. This means that the isolated effect should be negligible.

As each mode has a different RI sensitivity, the total sensitivity of the interference could be altered by an angled cleave or offset splice. However, according to the simulation results, the effect is almost negligible with only a slight increase for an angled cleave, see Table 2 below. As the dip visibility is reduced, the determination of the wavelength becomes less accurate. The depth of the dips decreased by almost two orders of magnitude, but how this effect appears experimentally may be partly washed out by the noise floor of the detector, the linewidth of the light source or the wavelength resolution of the detector.

4.4. Splice Angle

If the two fibers are spliced at an angle, the incoming phase front is tilted. As explained earlier, this enables azimuthal modes to be excited. The splice angles have been exaggerated in Figure 8 to highlight the effect. The spectra show that the overall intensity is reduced if the fibers are spliced at an angle. However, the interferometric visibility is maintained in the interval 1400–1500 nm. That the effects are less prominent than for an angled cleave is expected, as the input field is confined to the center of the fiber where the tilt-induced difference in optical pathlength is less than closer to the circumference of the fiber. Splice angles measured experimentally have not exceeded 0.2 degrees, which according to the model would not cause a significant effect.

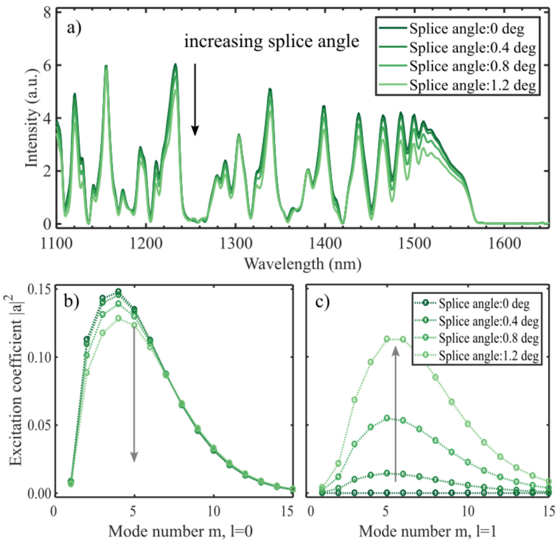

Figure 8. The spectra from a 14.2 mm CL interferometer which is spliced to the input fiber at an angle (**a**). To show the effect, the angles used are larger than what can be expected experimentally. An angled splice causes a lower overall intensity, as well as a small reduction in visibility of the interference. The excitation coefficients (**b**,**c**) are calculated at the splice between the SMF and the CL fiber (Equation (3)) for $l = 0$ and $l = 1$. With a larger offset more power is going into the azimuthal modes (**c**).

5. Discussion

5.1. Comparison of Experiment and Simulations

The simulated spectra of the 14.2 mm interferometer are shown in Section 4. Compared to Figure 2 it seems like the long wavelength cut-off/intensity drop is 40 nm red-shifted in the experimental results. This corresponds to a 0.67 mm shorter propagation length or a lower RI than what is used in the simulations. An underestimated interferometer length may be a consequence of the real-life beam expansion occurring at the hetero-interface.

For small cleave angles (≤ 0.2 degrees) there appears to be no correlation between the magnitude of the cleave angle and the observed spectral change. This is surprising as a nonzero cleave angle will increase the insertion loss (integrated across a wide wavelength range compared to the free spectral range of pairwise mode interference) of the device, resulting in a monotone decrease in intensities of the interference peaks as seen in the simulations. The insertion loss is due to the mode coupling form radial modes to azimuthal modes. The insertion loss estimated from the spectra in Figure 2 shows a decrease with the cleave angel varying from zero to 0.2 degrees. This might be explained by the inaccuracy of the cleave angle measurement and by the nonideal SMF-CLF splice (offset and/or angle) that will introduce mode coupling between the azimuthal modes and the SMF mode.

The periodicity, or the variations in periodicity, are comparable in the range 1350–1600 nm, although the amplitude of the different peaks varies. In the range 1450–1550 nm, the experimental results for low cleave angles show decreasing oscillations for lower wavelengths. Comparing with the simulations, this is a feature that is more prominent in the spectra for higher cleave angles, whereas the inaccuracies of the splice show the opposite effect. When the experimental spectra exhibit this behavior independent of the measured angle, a reasonable assumption would be that the effect is caused by the same mechanisms (i.e., the effect shown in Figure 5). A different distribution of power into the various modes changes the relative amplitudes of the peaks. It should also be noted that the excitation coefficients may show some variation with the wavelength, which is not considered in the model.

If the measured angle is approximately correct, the effect must stem from the spliced region. The simulations show that the end-face cleave angle causes the greatest effect on the spectrum, but this part of the sensor is also the part best described by the model. The splice is shown to have less effect in the simulations, but this part is not as well represented in the model. In a fusion splicer, the two fibers are pushed together with a small overlap, which creates a thicker region where the core geometry is less defined. It may also not be radially symmetric, as assumed in the model. This may excite more non-radial modes than what the model indicates and enable the azimuthal modes to contribute in the measured spectra. This would create spectra more resembling the experimental results. The abrupt coreless interface may therefore be a less accurate description. It seems like the non-abrupt splice may be less efficient in exciting the modes than the simulation shows.

5.2. The Electromagnetic Vector Model

The model used in this work is based on vectorized mode fields and their corresponding propagation constants. The rationale for the use of this model was the lifted degeneracy of the modes in systems with higher index contrast and the lack of radial symmetry in inaccurately fabricated sensor geometries. The four modes for each value of $l > 0$ are of interest, as they have individual excitation coefficients. The longitudinal components of the mode fields also increase at higher index contrast, but these disappear in the multiplication of the cross-product with the z-vector in (3).

As many of the modes are not linearly polarized (i.e., the polarization is a function of the position in the fiber), the effect of tilting the end-face is difficult to analyze with a scalar model. The individual contribution for LP modes is not well defined. The general model developed here is also suited for expanding the investigation into new systems with different geometries.

The RI sensitivity was found to vary little with the fabrication inaccuracies that were investigated with the MPA model. This is expected from the excitation coefficients, which show that the same modes contribute to the spectra. The results also confirm the experimental sensitivity around an RI of 1.33. However, because the change in the evanescent field with refractive index change is not described in the modes, this causes the underestimation found in the simulated RI sensitivity at higher RIs.

The vector model confirms that only the radially symmetric HE_{1m} modes need to be considered in radially symmetric systems. It may, however, be difficult to guarantee perfect symmetry in an experimental setting. It seems like the excitation of $l \geq 1$ modes can reduce the visibility of strong destructive interference dips originally present. According to the simulations, it is the cleave angle that has the largest impact on the spectrum. This may be understood from the large amount of modes present at the cleaved end-face, of which many have field distributions that span far out from the fiber center. This will increase the coupling into higher order azimuthal modes in the reflected field, as shown in Figure 5. That the effect is an interference phenomenon can be seen from each of the modes being affected differently. At each wavelength, the excitation coefficients exhibit different behavior, according to the phase relation of the incoming modes. Experimentally, however, the results indicate that the splice may affect the result to a larger degree.

6. Conclusions

The challenges of fabricating reflection-based, core-mismatched fiberoptic sensors based on multimode interference have been investigated by simulations and experiments. The mode-field propagation approach was used to explore the effect of an end-face cleave angle, an offset fusion splice, and an angled fusion splice. Whereas the fiber geometry defines the available modes and their propagation constants, the interfaces in the system decide the power distribution among the modes.

The experimental results showed the variability in the spectrums produced from a set of sensors with different cleave angles. Some peaks showed a consistent increase in intensity for larger cleave angles, whereas other showed a decrease. The length accuracy of the experimental setup was found to be ±100 μm based on the results from the simulations, which gave an estimated sensitivity to the interferometer length of 60 nm/mm. The refractive index sensitivity was estimated to be 65.5 nm/RIU.

According to the simulations, the end-face cleave angle has the largest impact on the spectrum, attributed to the wide distribution of optical power in the cross-section. The interferometric visibility was seen to be reduced by up to 70%. The inaccuracies in the spliced region were less prominent in the simulations, which was explained by the confined SMF mode field being less affected by the small alterations in the CL field. The reduction in visibility from an offset splice was less than 25% for the large offsets simulated, but for offsets experienced experimentally the effect becomes negligible. The angled splice did not affect the visibility but caused an overall lower intensity in the spectrum. However, the experimental results resembled the angled cleave simulations, but the effects were not always consistent. This indicates that the actual splice creates mode excitation similar to the effect of an angled cleave, with a larger portion of azimuthal modes excited.

This paper was written in the prospect that awareness of the challenges and mechanisms involved will enable more reliable and reproduceable sensors in the future.

Author Contributions: M.S.W., Ø.W. and D.R.H. conceptualized and designed the experiments; M.S.W. performed the experiments; M.S.W., Ø.W. and D.R.H. conceptualized and designed the model; M.S.W. created the model; M.S.W., Ø.W. and D.R.H. analyzed the results; M.S.W. prepared the original draft; Ø.W. and D.R.H. supervised and reviewed the paper; D.R.H. acquired funding for the project.

Funding: This work was supported in part by the strategic research funding from the Norwegian University of Science and Technology (NTNU), in part by the Interreg Sweden-Norway program (IR2015.01), and in part by the Energy and Sensor Systems group (ENERSENSE, strategic research program at NTNU).

Conflicts of Interest: The authors declare no conflict of interest.

References

1. Zhao, N.; Lin, Q.; Jiang, Z.; Yao, K.; Tian, B.; Fang, X.; Shi, P.; Zhang, Z. High Temperature High Sensitivity Multipoint Sensing System Based on Three Cascade Mach–Zehnder Interferometers. *Sensors* **2018**, *18*, 2688. [CrossRef] [PubMed]
2. Tripathi, S.M.; Kumar, A.; Varshney, R.K.; Kumar, Y.B.P.; Marin, E.; Meunier, J.-P. Strain and Temperature Sensing Characteristics of Single-Mode–Multimode–Single-Mode Structures. *J. Light. Technol.* **2009**, *27*, 2348–2356. [CrossRef]
3. Ahsani, V.; Ahmed, F.; Jun, M.; Bradley, C. Tapered Fiber-Optic Mach-Zehnder Interferometer for Ultra-High Sensitivity Measurement of Refractive Index. *Sensors* **2019**, *19*, 1652. [CrossRef] [PubMed]
4. Tian, Z.; Yam, S.S.; Loock, H. Single-Mode Fiber Refractive Index Sensor Based on Core-Offset Attenuators. *IEEE Photonics Technol. Lett.* **2008**, *20*, 1387–1389. [CrossRef]
5. Mohammed, W.S.; Mehta, A.; Johnson, E.G. Wavelength Tunable Fiber Lens Based on Multimode Interference. *J. Light. Technol.* **2004**, *22*, 469–477. [CrossRef]
6. Li, E.; Wang, X.; Zhang, C. Fiber-optic temperature sensor based on interference of selective higher-order modes. *Appl. Phys. Lett.* **2006**, *89*, 091119. [CrossRef]
7. Wang, Y.; Liu, Y.; Zou, F.; Jiang, C.; Mou, C.; Wang, T. Humidity Sensor Based on a Long-Period Fiber Grating Coated with Polymer Composite Film. *Sensors* **2019**, *19*, 2263. [CrossRef] [PubMed]
8. Engholm, M.; Hammarling, K.; Andersson, H.; Sandberg, M.; Nilsson, H.-E. A Bio-Compatible Fiber Optic pH Sensor Based on a Thin Core Interferometric Technique. *Photonics* **2019**, *6*, 11. [CrossRef]
9. Gu, B.; Yin, M.-J.; Zhang, A.P.; Qian, J.-W.; He, S. Low-cost high-performance fiber-optic pH sensor based on thin-core fiber modal interferometer. *Opt. Express* **2009**, *17*, 22296. [CrossRef]
10. Zhu, T.; Wu, D.; Liu, M.; Duan, D.-W. In-Line Fiber Optic Interferometric Sensors in Single-Mode Fibers. *Sensors* **2012**, *12*, 10430–10449. [CrossRef]
11. Lee, B.H.; Kim, Y.H.; Park, K.S.; Eom, J.B.; Kim, M.J.; Rho, B.S.; Choi, H.Y. Interferometric Fiber Optic Sensors. *Sensors* **2012**, *12*, 2467–2486. [CrossRef] [PubMed]
12. Wang, Q.; Farrell, G.; Yan, W. Investigation on Single-Mode–Multimode– Single-Mode Fiber Structure. *J. Light. Technol.* **2008**, *26*, 512–519. [CrossRef]
13. Ivanov, O.V. Fibre-optic interferometer formed by a section of small-core fibre spliced between standard fibres. *Opt. Commun.* **2009**, *282*, 3895–3898. [CrossRef]
14. Zhang, Y.; Zhou, A.; Qin, B.; Deng, H.; Liu, Z.; Yang, J.; Yuan, L. Refractive Index Sensing Characteristics of Single-Mode Fiber-Based Modal Interferometers. *J. Light. Technol.* **2014**, *32*, 1734–1740. [CrossRef]
15. Wu, Q.; Semenova, Y.; Wang, P.; Farrell, G. A comprehensive analysis verified by experiment of a refractometer based on an SMF28–small-core singlemode fiber (SCSMF)–SMF28 fiber structure. *J. Opt.* **2011**, *13*, 125401. [CrossRef]
16. Xiong, R.; Meng, H.; Yao, Q.; Huang, B.; Liu, Y.; Xue, H.; Tan, C.; Huang, X. Simultaneous Measurement of Refractive Index and Temperature Based on Modal Interference. *IEEE Sens. J.* **2014**, *14*, 2524–2528. [CrossRef]
17. Li, L.; Xia, L.; Xie, Z.; Hao, L.; Shuai, B.; Liu, D. In-line fiber Mach–Zehnder interferometer for simultaneous measurement of refractive index and temperature based on thinned fiber. *Sens. Actuators A Phys.* **2012**, *180*, 19–24. [CrossRef]
18. Nguyen, L.V.; Hwang, D.; Moon, S.; Moon, D.S.; Chung, Y. High temperature fiber sensor with high sensitivity based on core diameter mismatch. *Opt. Express* **2008**, *16*, 11369. [CrossRef]
19. Wu, Q.; Semenova, Y.; Wang, P.; Farrell, G. High sensitivity SMS fiber structure based refractometer—Analysis and experiment. *Opt. Express* **2011**, *19*, 7937. [CrossRef]
20. Wei, T.; Lan, X.; Xiao, H. Fiber Inline Core–Cladding-Mode Mach–Zehnder Interferometer Fabricated by Two-Point CO2 Laser Irradiations. *IEEE Photonics Technol. Lett.* **2009**, *21*, 669–671.
21. Liu, Y.; Wei, L. Low-cost high-sensitivity strain and temperature sensing using graded-index multimode fibers. *Appl. Opt.* **2007**, *46*, 2516. [CrossRef] [PubMed]
22. AFL CT-101 and CT-102 Fiber Cleavers. Available online: https://www.aflglobal.com/productlist/Product-Lines/Fusion-Splicing-Systems/CT-101-and-CT-102-Fiber-Cleavers/doc/CT-101-102.aspx (accessed on 21 January 2019).

23. Zhou, G.; Wu, Q.; Kumar, R.; Ng, W.P.; Liu, H.; Niu, L.; Lalam, N.; Yuan, X.; Semenova, Y.; Farrell, G.; et al. High Sensitivity Refractometer Based on Reflective Smf-Small Diameter No Core Fiber Structure. *Sensors* **2017**, *17*, 1415. [CrossRef]
24. Zhou, X.; Chen, K.; Mao, X.; Peng, W.; Yu, Q. A reflective fiber-optic refractive index sensor based on multimode interference in a coreless silica fiber. *Opt. Commun.* **2015**, *340*, 50–55. [CrossRef]
25. Saito, Y.; Wang, J.J.; Smith, D.A.; Batchelder, D.N. A Simple Chemical Method for the Preparation of Silver Surfaces for Efficient SERS. *Langmuir* **2002**, *18*, 2959–2961. [CrossRef]
26. Malitson, I.H. Interspecimen Comparison of the Refractive Index of Fused Silica. *J. Opt. Soc. Am.* **1965**, *55*, 1205. [CrossRef]
27. Snyder, A.W.; Love, J.D. *Optical Waveguide Theory*; Chapman and Hall: London, UK, 1983; ISBN 0-412-24250-8.
28. Adler, R. Waves on inhomogeneous cylindrical structures. *Proc. IRE* **1952**, *40*, 339–348. [CrossRef]
29. Xia, T.-H.; Zhang, A.P.; Gu, B.; Zhu, J.-J. Fiber-optic refractive-index sensors based on transmissive and reflective thin-core fiber modal interferometers. *Opt. Commun.* **2010**, *283*, 2136–2139. [CrossRef]

PAPER II

Using Fiber-Optic Sensors to Give Insight into Liquid-Solid Phase Transitions in Pure Fluids and Mixtures[⋆]

Markus Solberg Wahl[a,*], Øivind Wilhelmsen[b,c], Dag Roar Hjelme[a]

[a]*Norwegian University of Science and Technology (NTNU), Department of Electronic Systems, 7491 Trondheim, Norway*
[b]*Norwegian University of Science and Technology (NTNU), Department of Energy and Process Engineering, 7491 Trondheim, Norway*
[c]*SINTEF Energy Research, 7034 Trondheim, Norway*

Abstract

Fiber optic sensors offer a new and unique way to detect and analyze phase transitions, due to their small thermal mass and inert material. This paper presents and demonstrates a dual-sensor system to detect and analyze phase transitions in pure water and aqueous ethanol mixtures. With a multi-mode interferometer based on a thin-core fiber, and a fiber Bragg grating sensor, it is possible to differentiate between refractive index, temperature and strain in the sample system. The three parameters supply important information during a phase transition, but also in the characterization of the liquid and solid phases. Binary mixtures at non-eutectic concentrations are expected to separate into a solid phase consisting of only one constituent, and the sensors are demonstrated to be able to estimate the concentration in the remaining liquid phase. For pure water and low ethanol concentrations, the progression of the phase transition was found to be limited by heat transfer, whereas for higher concentrations the process becomes mass transfer limited. In pure water, strain due to thermal expansion of the ice hinderes temperature measurements in the solid phase. The reflection-based geometry enables insertion probes that measure the properties inside the samples, with little or no disturbance of the system. By interpreting the sensor response in a known system, the sensing capabilities in unknown substances can be evaluated. The sensor system is able to capture the dynamics of the phase transition, which can be difficult to predict theoretically due to the multitude of contributing effects. Analysis of the combined signal from the two sensors enables the determination of the ethanol mixture melting points in agreement with the literature, within the uncertainty of the system (0.25 K).

Keywords: phase transitions, fiber optic sensors, multimode interference, fiber Bragg grating

1. Introduction

A fundamental understanding of phase transitions is important both in industrial processes and for research purposes. To detect the onset of a phase transition, and to monitor its subsequent progression, is paramount in fields such as in energy storage systems based on latent heat [1], food technology [2], the pharmaceutical industry [3], and liquefaction of hydrogen [4, 5]. Understanding and control of the liquid-to-solid transition is also important in biology and in fixation of biological tissue for optical microscopy [6, 7].

Because the nucleation and growth that initiates a phase transition is stochastic in nature, accurate detection is important. Detecting the phase transition directly can aid in confirming, creating, or alleviate the need for a prediction. Because ethanol is miscible in both polar and non-polar substances, it is a versatile solvent in a wide range of industries (e.g., chemical, pharmaceutical, food and fuel)[8]. Studies have shown that refractometric analysis of aqueous ethanol mixtures is challenging due to anomalies in the physical-chemical properties, such as hydrophobic solute association and the formation of ethanol clusters [9, 10]. Freezing of such binary mixtures, has been widely studied [11, 12, 13, 14] and it is accepted that the solid phase that forms is pure ice i.e. it consists of only water molecules. This entails that the concentration in the remaining liquid phase, and its associated properties, change during the phase transition.

Classical techniques to detect liquid-to-solid transitions include differential scanning calorimetry [11, 14] and differential thermal analysis [6, 15], which measure the difference in heat exchange and temperature, respectively, as the temperature is scanned over the interval where a phase transition is expected to occur. Although these techniques give important information on phase transitions, the experimental setup is complicated and not well suited for industrial application, and it does not allow for measurements in specific points in the sample or a reactor. It is also possible to detect liquid-solid transitions by measuring

---

[⋆]This document is the result of the research project funded by InterReg Sweden-Norway program [IR2015.01] and the ENERSENSE research initiative.

[*]Corresponding author
Email address: `markus.s.wahl@ntnu.no` (Markus Solberg Wahl)

Preprint submitted to Experimental Thermal and Fluid Science *May 1, 2020*

the changes in conductivity. A current is sent through the sample and an increase in impedance indicates solidification [2]. Because phase transitions are either exothermic or endothermic, they can also be detected by measuring the temperature changes locally, using electronic temperature sensors (e.g., thermocouples). However, these sensors may disturb the measurements by acting as heat sinks/sources, and thus affect the temporal response due to their thermal mass [16]. For transparent materials, phase transitions can also be observed visually, if they cause a change in the transparency. However, this requires transparent containers or windows [17], which may not always be feasible in the design of the measurement rig or reactor.

General advantages of fiber optic sensors in experimental thermophysics and thermochemistry include the inert glass material of optical fibers, their robustness and small size. This enables sensors with a small thermal mass, which minimize the influence on thermodynamic processes. This is ideal for accurate measurements in small sample sizes, or where heat flow is a limiting factor. Optical fibers made of fused silica also remain flexible at cryogenic temperatures [18], which makes them robust and especially well suited in low temperature sensing. Immunity to electromagnetic interference, high sensitivity, low cost and the possibility for remote sensing are other advantages that motivate the use of fiber optic sensors.

Researchers have in recent years developed fiber optic sensors to detect and study phase transitions [19, 20, 21, 22, 23]. Han et al. detected the phase transition in n-octadecane by utilizing the different refractive index (RI) in the solid and liquid states. For N-octadecane, these values happen to be above and below the RI of the fiber, which enables the distinction of phases based on a guiding- or no-guiding-condition. This was demonstrated both in a multi-mode fiber interferometer [19] and a Fresnel reflection probe [23]. Also based on changes in reflectivity, Mani et al. [22] detected freezing of aqueous NaCl-solutions. These Fresnel-reflection sensors offer a mechanically robust point measurement of the aggregate state, as only the cleaved end-face of a single-mode fiber (SMF) is required to be in contact with the sample. However, the small interface with the sample makes the technique sensitive to irregularities such as bubbles or impurities that may be present in the sample. A method with a larger sample interface to average over was presented by Millo et al. [20], who performed evanescent field attenuation spectroscopy in the infrared (IR) range to detect the freezing event in water and heavy water. However, the transmission configuration and the need for specialty fibers that are transmissive in the IR complicates the experimental implementation. Kumar et al. [21] used a fiber-optic multi-mode interferometer to measure micro-strain induced by the solidification of paraffin wax.

This paper presents a novel dual-sensor setup to detect and study phase transitions, based on well-known fiber-optic sensor technologies. It consists of a fiber-optic multi-mode interferometer [24], interrogated in reflection, together with a fiber Bragg grating (FBG) sensor [25]. The sensors and the interrogation setup are depicted in Fig. 1. The RI sensitivity of the multi-mode interferometer enables detection of all phase transitions that cause a change in RI. However, the interferometer is also sensitive to temperature and strain [26, 27]. To distinguish between these parameters, an FBG sensor is used, which is also sensitive to temperature and strain, but not to RI. Under the assumption that a liquid material imparts an insignificant strain on the sensors, any deviations from the FBG sensor temperature sensitivity in the solid phase can be attributed to strain. The dual-sensor setup can therefore be used to distinguish between these parameters, which implicitly also lead to measurement of parameters such as sample concentration, freezing point, melting point and latent heat.

The reflection-based geometry of the fiber-optic sensors creates insertion probes that are clamped only in one end. This simplifies the implementation, and alleviates thermally induced bending stress that may occur in transmission-based sensors. This sensor can therefore give information on both the liquid and solid phase, in addition to the transition itself.

The next section will present the dual-sensor configuration and the measuring procedure. The results for measurements in pure water and the binary mixtures of ethanol and water will then be presented and discussed to highlight the amount of information obtained from the sensor setup. By interpreting the results in a known system, it is showed how the sensor response can be utilized to examine substances with unknown properties. Throughout the paper, a distinction between the freezing point and the melting point of the sample will be upheld.

2. Experimental Methods

The experimental setup is illustrated in Fig. 1, showing the sensor configuration (left) and the measurement rig (right). The optical interrogation setup consists of a broadband source (FYLA, SCT500), a grating-based spectrometer with 0.3 nm resolution (Ibsen I-MON 512), and a 2x2 coupler (Thorlabs, TW1550R5A2). The sensors are connected to the remaining two arms of the coupler. The FBG sensor (Optromix) is inscribed in an SM1500 fiber with a reflectivity of 79% and full-width half-maximum (FWHM) of 0.2 nm. The multi-mode interferometer is fabricated by splicing a 14.2 mm section of thin-core (TC) fiber (SM400) to the end of a single-mode fiber (SMF). The core-diameter mismatch causes cladding modes to be excited in the TC fiber, which create the interference spectrum. To ensure good visibility in the interference spectrum, the cleave angles were confirmed to be smaller than 0.1 degrees [24]. To increase the reflected signal, a silver mirror was deposited at the end-face of the fiber by the mirror reaction [28]. The fiber was placed in contact with the reactant solution and withdrawn carefully without breaking the meniscus created by surface tension. By

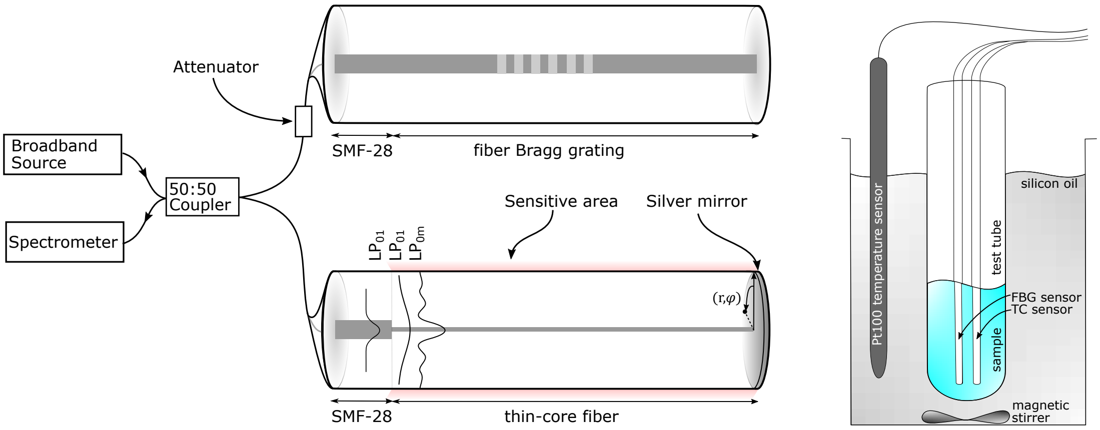

Figure 1: Schematic of the experimental setup. The fiber-optic sensor system (left) consists of a broadband source, a spectrometer, a 50:50 fiber optic coupler and the two sensors (fiber Bragg grating (FBG) and thin-core (TC) interferometer). Both sensors reflect light at wavelengths dependent on their temperature and strain, whereas only the TC-sensor is sensitive to the RI of the surroundings. The fiber-optic attenuator is used to get comparable signal intensities from the two sensors. The measurement rig (right) consists of a temperature bath filled with silicon oil, an electrical Pt100 temperature sensor and a test tube holding the sample liquid. The two sensors are placed inside the sample.

monitoring the reflected signal during silver deposition, the process could be ended when the reflectivity reached its maximum (∼66%). Inspection with an optical microscope showed an approximate mirror thickness of 60 μm. To achieve comparable signal intensities from the two sensors, a variable fiber-optic attenuator was placed between the coupler and the FBG sensor. A band-pass filter was also used to block wavelengths outside the range of the spectrometer (1510-1610 nm).

The FBG sensor has a strong reflection peak at a wavelength, λ_B given by [25]:

$$\lambda_B = 2n_{eff}\Lambda, \tag{1}$$

where n_{eff} is the effective RI of the grating and Λ is the grating period. A change in the temperature, ΔT will affect both the effective RI and the period of the grating due to the thermo-optic effect and thermal expansion. The change in wavelength can be expressed as [29]:

$$\Delta\lambda_B = \lambda_B(\alpha + \xi)\Delta T \tag{2}$$

where α is the thermal expansion coefficient, and ξ is the thermo-optic coefficient, which accounts for approximately 95% of the temperature sensitivity [25]. The sensitivity to strain was found to be approximately 1 pm/$\mu\varepsilon$ in previous work [25].

The interference spectrum from the TC sensor exhibits intensity dips at wavelengths where the modes interfere destructively. The wavelength of the i'th dip, $\lambda_{dip,i}$ can be expressed as:

$$\lambda_{dip,i} = \frac{4L\left[n_{eff}(\lambda, n_{ext}) - n'_{eff}(\lambda, n_{ext})\right]}{2i-1}, \tag{3}$$

where L is the length of the interferometer, n_{eff} and $n'_{eff}$is the effective index of two modes at wavelength λ and external (sample) RI (n_{ext}). Because of the evanescent field extending beyond the boundaries of the fiber, the effective indices of the modes depend on the external RI. The interference spectrum will therefore shift based on the RI surrounding the sensor. As explained in [24], this sensitivity to the external RI can be expressed as

$$\frac{d\lambda_{dip}}{dn_{ext}} = \frac{\lambda_{dip}}{(n_g - n'_g)}\left(\frac{\partial n}{\partial n_{ext}} - \frac{\partial n'}{\partial n_{ext}}\right) \tag{4}$$

where n_g and n'_g is the group velocity of the same two modes. This shows that it is the difference in sensitivity to the external RI of the two modes that cause the RI sensitivity of the interferometer.

The temperature sensitivity appears because both n_{eff} and n_{ext} are functions of temperature. Although the thermo-optic coefficient of water is two orders of magnitude higher than that of the fiber material [30, 31], the fiber properties dominate because of the high confinement factor. In this sensor, only 10^{-2}% of the electromagnetic field extends beyond the fiber boundaries, but this can be increased by etching the fiber with hydrofluoric acid [10].

A temperature bath (Hart Scientific, 7103 Micro-bath) with an accuracy of 0.25 K, was used to perform the temperature scans (Fig. 1, right). An additional temperature sensor (3-wire, Pt100) with a stainless steel sheath, was placed in the silicon oil bath fluid. The fiber-optic sensors were secured 1 mm apart inside a test tube (Borosil, 27 ml), with the sample placed 10 cm below the silicon oil surface. The test tube was left open at the top to keep the sample at atmospheric pressure. A LabVIEW program was developed to control the temperature setpoints and scan rate in the temperature bath, and for acquiring data from the Pt100-sensor and the spectrometer. The output was logged every 20 s. Additionally, a digital boroscope was placed in the temperature bath to visually monitor the process, and capture images and videos.

The samples were prepared with deionized water ($< 1.5\mu$S/cm) mixed with 96% Ethanol (VWR) by weight. From the uncertainty disclosed by the manufacturer, the estimated error in the concentration of the prepared mixtures was 0.4%. The mixtures were heated to 50°C for 5 h and subsequently stored for one week to let the mixtures equilibrate, in accordance with the recommendations by Takaizumi et al. [12]. 6 mL of sample fluid was placed in the test tube before the fibers were inserted. The fiber-optic sensors were clamped in a way that ensured that they had the same position in the test tube each run. The samples were then let to stabilize at 30°C for 15 min, which was necessary to achieve reproducible results, especially at higher ethanol concentrations. The temperature scans were performed with a cooling rate of 0.2°C/min down to -30°C, and heating rate of 0.1°C/min back to 30°C. Prior to all measurements, the test tube and the optical fibers were rinsed with acetone, 96% ethanol and DI water, to remove any contaminants.

Freezing of water into ice occurs when an ice nucleus appears that is larger than the critical size for further growth. This is a statistical process that is driven by the degree of metastability i.e. a larger supercooling will increase the probability of a critical-size nucleus to initiate the phase transition. Because of the enthalpy of fusion, the freezing process will release latent energy that heats the sample. This limits the amount of solids that can be produced, as the sample cannot exceed its melting temperature [32]. Treating the system as adiabatic in the instant where the solid phase forms (freezing), the heat produced by the solidification (ΔQ_{ice}^{fus}) must be equal to the heat spent to heat up the sample. The energy balance then gives:

$$\Delta Q_{liq} + \Delta Q_{ice} = \Delta Q_{ice}^{fus}, \tag{5}$$

where ΔQ_{liq} and ΔQ_{ice} are the heat absorbed by the remaining liquid phase and the solid ice phase, respectively. This can further be formulated as:

$$C_p^{liq} m_{liq} \Delta T_s + C_p^{liq} m_{ice} \Delta T_s = \Delta H_{fus}^{ice} m_{ice}, \tag{6}$$

where C_p^{liq} and C_p^{ice} are the specific heat capacities of the liquid and ice, respectively, m_{ice} is the amount of ice produced, m_{liq} is the remaining liquid, ΔT_s is the supercooling, and ΔH_{fus}^{ice} is the enthalpy of fusion for ice. A greater supercooling or heat capacity of the liquid will therefore produce more solid when the sample freezes, and reduce the amount of additional heat that must be removed to freeze the remaining liquid. As the enthalpy of fusion decreases for higher ethanol concentration [14, 33], more ice may initially be produced, and the subsequent crystal growth requires less heat to be transferred. We assume in the above equation that the heat capacities are approximately constant in the considered temperature interval.

3. Results and Discussion

Snapshots of how the freezing of 10% ethanol progresses are shown in Fig. 2. In this case, the nucleation occurs in the bottom of the test tube and the crystal grows upwards. Where in the test tube and at what temperature the nucleation takes place, varies from experiment to experiment. Higher concentrations were observed to slow down the crystallisation process, in agreement with [34, 35].

An example of an output spectrum from the dual-sensor configuration is shown in Fig. 3. The three main interference dips and the FBG peak are highlighted. To accurately determine the wavelength of the dips, they were fitted to a fifth-degree polynomial over a 9 nm spectral range. The FBG peak wavelength was similarly found by curve-fitting a Gaussian function. In the following sections, the change in these wavelengths during the temperature scans will be presented and interpreted to analyze the phase transitions.

At constant temperature in the bath, the measured root-mean-squared error (RMSE) of the determined wavelengths were 1.4 pm and 5.7 pm for the FBG and TC sensor, respectively. With an FBG temperature sensitivity of 9.2 pm/°C, this gives a mean error of 0.15°C. The TC sensor was measured to have an RI sensitivity of 51.6 nm/RIU at n=1.3165 (pure water at 1550 nm). The FBG sensor is assumed to have a strain sensitivity of 1pm/$\mu\varepsilon$, based on previous results [25].

3.1. Freezing of pure water

To study the sensor response in pure water, the sensors were placed in a 6 mL sample and cooled down to -30°C, as described in the Sec. 2. Fig. 4 shows the wavelength of the FBG-peak during the experiment, both as a function of temperature (left) and time (right). Both plots show the same data, with the wavelength axis spanning both plots. The measured temperature (Pt100) is also plotted as a function of time in the right plot (red). On cooling, the FBG-sensor is assumed to have no strain in the liquid, and the wavelength shifting to shorter wavelengths is therefore only due to the change in temperature (Eq. 2). The shift in the liquid phase can therefore be used to create a baseline for the sensitivity, from which deviations must be caused by strain or a difference in temperature compared to what is measured outside the test tube in the bath fluid.

This difference can be observed when the water freezes at -11.8°C, which causes a sudden rise in temperature due to the release of latent heat. The peak shifts to a wavelength that corresponds to a temperature of 0°C. With a heat of fusion for ice of 333.55 J/g and an undercooling of 11.8°C, and assuming adiabatic conditions in the instant

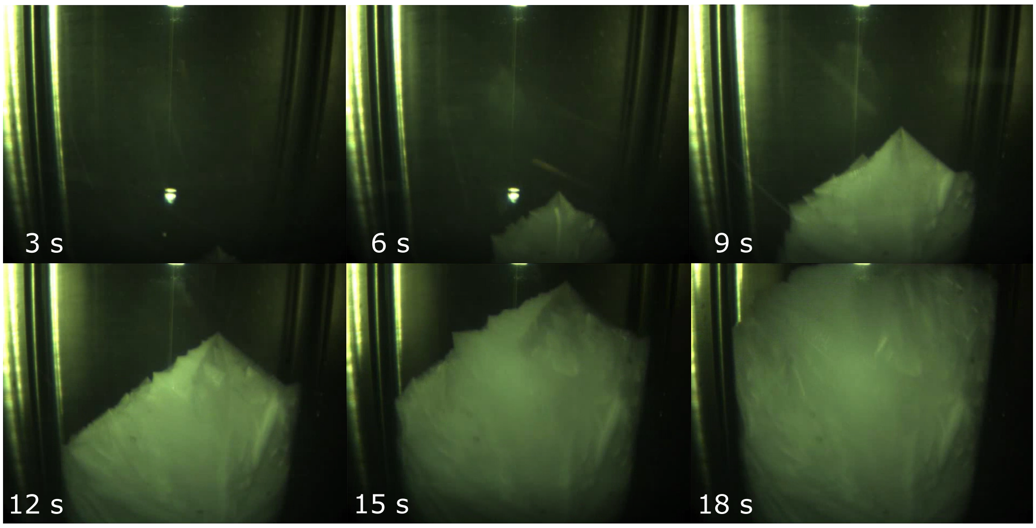

Figure 2: Snapshots show the progression during freezing of 10% ethanol at 3 second time intervals. Multiple crystal facets are visible. The high crystallinity indicates high purity in the solid phase.

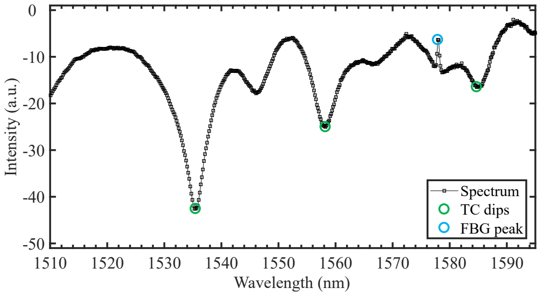

Figure 3: A typical output spectrum, showing the sum of the reflected intensities from the two sensors as a function of wavelength. Three interference minima (dips) are identified, but only the first is used in interpreting the response. The peak from the FBG sensor has been attenuated as to not saturate the spectrometer, while ensuring acceptable visibility of the interference spectrum. The features of both sensors shift to longer wavelength (red-shift) with increasing temperature. The TC sensor red-shifts for increasing external RI.

of freezing, calculations based on Eq. 6 estimate that only 0.83 g (14%) of ice is produced, see Table 1. Visual inspection showed that, contrary to the behavior seen in ethanol mixtures (Fig. 2), the initial solid phase in the pure water samples fills the whole sample volume with a slush or a dendritic ice structure in less than a second [36].

Further freezing requires additional heat transfer from the sample to the bath fluid. The heat transfer only facilitates the freezing of more water, and will not be able to cool the sample further until all liquid is frozen. According to the sensor output, this process takes around six minutes, after which the wavelength again continues to blue-shift. In the figure, this process is highlighted with green arrows and shown in higher detail in the inset, which shows the initial heating (red-shift) and the subsequent cooling and strain-induced blue-shift. The FBG sensor is hence able to resolve and distinguish the three phases of crystallization, the nucleation, the dendritic phase, and the crystal growth [6].

3.1.1. The influence of heat flux on the detected strain

The initial blue-shift 60 pm below the baseline is attributed to the increased volume of ice over water, which causes strain on the sensor. Further cooling causes the FBG-peak to deviate further from the liquid baseline, which is interpreted as increased strain due to thermal expansion. This is consistent with increased compressive strain in the axial direction of the fiber due to ice compaction at lower temperatures [37], which is two orders of magnitude higher than that of the fiber [30]. By using the strain sensitivity from [25], the shift corresponds to a strain of approximately 300 $\mu\varepsilon$.

When the heating starts, the stress on the fiber seems to relax faster than it was built up during cooling, and the peak wavelength returns to the baseline already at -23°C. During several repetitions of the experiment, most runs showed similar accelerated relaxation. It is an interesting effect as it initiates only when the sample is heated, and happens continuously over one hour. To investigate if the relaxation was due to the optical power causing local heating at the fiber tip, a measurement was conducted with the laser power reduced to 4%, which did not change the relaxation rate. Since the fiber extends out into room temperature, heat conduction through the fiber could also supply the heat necessary for the relaxation. Several heating and cooling cycles below 0°C were also performed to investigate whether the effect is caused by thermal expansion effects in the ice, or if the relaxation is due to slow slippage at the fiber-ice interface. This showed that upon every cooling stage, the increased stress on the fiber appeared, and was released at an increased rate during reheating. For each cycle the strain decreased – during the fourth cool-down the strain response was halved. This may indicate some slippage of the fiber relative to the ice when the sample is heated. Only a decrease in thermal strain due to heat conduction through the fiber was found to support this behavior.

We emphasize that only sensor signals from the phases of the experiment deemed to be strain-free have been used to interpret results from the phase-transitions. Further discussions of strain therefore fall beyond the scope of the present work.

3.1.2. Melting of pure water

At the melting point (0°C), the peak wavelength remains constant until the bath fluid reaches 5°C. This shelf is interpreted as the sample having constant temperature, which is attributed to the endothermic melting of ice. To melt the 6 mL sample requires 2.1 kJ of heat, which is transferred slowly due to the low temperature difference. During this phase, the sample will remain at the melting temperature.

The temperature increase and retention during freezing and melting cannot be resolved by the temperature sensor (Pt100) outside the test tube. Having a temperature sensor with a small thermal mass therefore makes it possible to capture the dynamics of the phase transition.

3.1.3. Refractometric analysis of the phase transition

With the addition of an RI sensitive sensor, also the properties of the liquid and solid phases can be probed. Tracking the intensity dip created by the TC sensor in the same experiment as above gives the behaviour shown in Fig. 5. As this sensor is also sensitive to the RI surrounding the fiber, the temperature sensitivity becomes a convolution of the thermo-optic properties of both the fiber and the liquid. This is described by Eq. 3, where both n_{eff} and n_{ext} are functions of temperature. This enables further analysis of the properties of both the liquid and the solid phase.

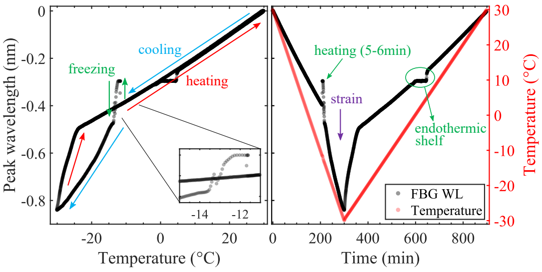

Figure 4: The wavelength of the FBG-peak (Fig. 3) and how it shifts as a function of temperature and aggregate state of the surrounding medium. Both plots show the same data, as a function of temperature (left) and time (right). Upon cooling, the peak shifts to shorter wavelengths (blue-shift) until the freezing event causes a short-timed local heating (inset). The stronger blue-shift after freezing is due to strain. When the sample is reheated, the strain relaxes, and at 0°C, the ice starts to melt. The melting process keeps the local temperature constant until the whole sample has become liquid.

As with the FBG-results (Fig. 4), the freezing event creates a red-shift to the wavelength that corresponds to a temperature of 0°C. However, after the whole sample has become solid, the dip shows a large blue-shift of approximately 1.1 nm. This is comparable with the expected shift due to a difference in RI of 0.025 between water and ice ($51.6\text{nm/RIU} \cdot 0.025 = 1.29\text{nm}$). The compressive strain seen earlier in Fig. 4 (200-400 min) can be seen to cause a red-shift in the TC sensor (right graph). The opposite direction of the strain-induced shift from the TC sensor is consistent with the results in [38] if compressive strain occurs in the axial direction. At 380 min, the FBG sensor indicates that the strain is released and the TC sensor pivots. The sensor may still be affected by some strain, but the sensitivity is now positive with regards to temperature (400-600 min). Although the thermo-optic coefficient of ice is negative, as it is for water above 4°C [31], the positive sensitivity is expected because the fiber temperature response dominates. At 0°C, the intensity dip experiences large shifts during the melting, before it joins the liquid baseline. The combined analysis of the two sensors emphasizes the benefits of having a dual-fiber setup, as discussed in the present work.

3.2. Freezing of ethanol mixtures

The FBG sensor result for the 10% sample is shown in Fig. 6. As in the results for pure water, the exothermic reaction heats the sample, which can be seen as a temporary red-shift in the cooling curve. However, due to the increased ethanol concentration in the remaining liquid phase, the melting point is continuously lowered as the freezing progresses. Contrary to the result for pure water, the temperature therefore decreases during the phase transition. When the freezing approaches completion, the cooling of the solid can proceed. This can be seen by comparing the endothermic shelves in Figs. 4 and 6. While

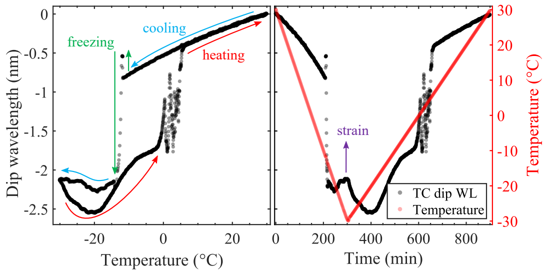

Figure 5: The wavelength of the first TC interferometer dip (Fig. 3), from the same experiment as Fig. 4, as a function of temperature (left) and time (right). The same initial heating upon freezing is observed, but is in this case followed by a 1.2 nm blue-shift due to the lower RI of ice. Based on the results in Fig. 4, one can conclude that part of the shift in the solid ice is due to strain.

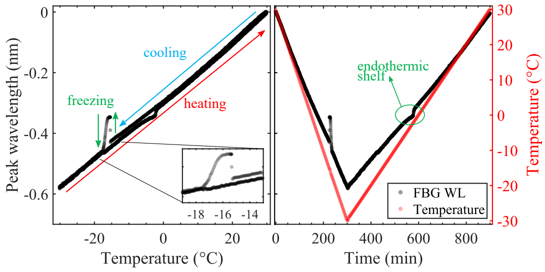

Figure 6: The wavelength shifts of the FBG-sensor in 10% ethanol, as a function of temperature (left) and time (right). As in the case of pure water, the freezing event causes a short red-shift due to local heating. However, the sensor does not experience any significant strain from the solid formed.

the endothermic shelf in Fig. 4 is perfectly horizontal, the shelf in Fig. 6 exhibits a slope.

As the sample regains equilibrium with the temperature bath, the response resumes its strain-free behavior. Because little or no strain is observed in the cooling process, the slightly shorter wavelength seen when reheating is probably not caused by strain, but rather by the continuous thawing of ice in binary mixtures over a finite temperature interval. This would keep the sample at a slightly lower temperature since additional heat must be supplied. However, the endothermic shelf observed in the pure water measurements reappears at -5°C until 2°C, where the remaining ice melts. The melting point of 10% ethanol is -4.5°C [39].

Fig. 7 shows the wavelength shifts from the FBG sensor for all ethanol concentrations measured, as a function of the cooling bath temperature. Due to freezing-point depression in binary mixtures, the higher concentrations freeze at lower temperatures. The freezing temperatures are indicated with grey lines. The 30% sample did not overcome the nucleation barrier in the temperature range measured and is therefore not shown, whereas the 25% sample first froze during the heating phase. The pure water shows clear evidence of compressive strain, but also the 5% sample seems to have some compression of the sensor.

The amount of super-cooling for each sample is summarized in Table 1. Based on the heat of fusion [33] and specific heat capacities for ethanol mixtures [40], the expected amount of ice initially formed was calculated using Eq. 6. For all ethanol concentrations, less than 23.5% of the water is able to freeze. That higher concentrations are able to produce more ice without additional heat transfer, is owed by the decrease in latent heat, increase in specific heat capacity, and increased super-cooling.

Although higher ethanol concentrations initially produce more ice, the freezing process was visually observed to be slower in the more concentrated samples. This is probably due to limited mass transfer at the solid-liquid interface, which also has been observed in forced convection studies [34, 35]. These studies describe the creation of a ”mushy zone” consisting of concentrated solute inclusions, which was also observed in the 30% ethanol sample used in this study.

The different melting points of water and low ethanol concentrations can again be observed by the endothermic shelves extending below the baseline, but at higher ethanol concentrations, the shelves become less pronounced. This is expected, as the melting temperature will increase as the ethanol concentration in the liquid phase decreases during melting.

By using the shift in the FBG wavelength prior to freezing as a function of temperature, a calibration curve can be established. With the calibration curve, and the data in Fig. 7, the actual temperature inside the sample can be estimated. This is shown in Fig. 8 as a function of time, for the freezing events (left) and melting (right). The calculation assumes that the shift is only a function of temperature, which clearly causes anomalies in the results for pure water. Because of the small strain seen after freezing for low ethanol concentrations, the temperature is underestimated on this interval. In the mixtures, the largest error is 4°C in the 5% sample.

The water measurement also shows a period of constant temperature during freezing, whereas the ethanol samples decrease in temperature during freezing (Fig. 8, left). The latter is expected as the ethanol concentration increases during the freezing process, which lowers the melting temperature. The temperature is therefore maintained at the decreasing melting temperature as long as the release of latent heat is faster than the heat transfer out of the sample to the temperature bath. This effect can be compared to the decrease in endothermic energy in Fig. 1 in the work of Takaizumi et al. [12] and was also observed in the freezing of biological specimens [6]. The effect is evident already at 5%, but increases for higher concentrations. It should also be noted that due to the amount of ice initially formed, shown in Table 1, the plateaus of elevated temperature correspond to concentrations higher than before the nucleation. This causes the temperatures during the crystal growth phase to be lower than what is expected

Table 1: Thermodynamic properties and calculated mass of ice created upon nucleation. The super-cooling (T_s) is the difference between the measured freezing temperatures and the melting points from the CRC Handbook [39]. The heat of fusion values were extracted from Kumano et al. [33] and the heat capacities from Rivkin et al. [40]. The amount of water originally present was calculated from the sample volume (6 mL) based on the densities of the mixtures.

Concentration:	0%	5%	10%	15%	20%	25%	30%
T_s (°C):	11.8°C	11.7°C	12°C	13.8°C	14°C	11°C	-
ΔH_{fus} (J/g):	333.55	328.9	320.6	308.8	293.2	274.1	251.3
C_p^{liq} (J/gK):	4.18	4.22	4.27	4.32	4.37	4.42	4.49
C_p^{ice} (J/gK):	2.108	2.108	2.108	2.108	2.108	2.108	2.108
Produced ice(g):	0.83	0.83	0.87	1.03	1.10	0.94	-
% of water:	13.8%	14.7%	16.4%	20.7%	23.5%	21.6%	-

in the initial concentrations. Because the eutectic point is not reached in the measurement, the freezing will continue throughout the cooling stage. However, at one point, the amount of remaining liquid will be small enough and have a high enough concentration to slow down the phase transition sufficiently for the temperature to decrease down to that of the bath fluid. Samples with higher concentration will slow down earlier and therefore have a shorter period at the elevated temperature.

Fig. 8 (right) shows the temperature inside the samples during the heating stage, where the endothermic shelves are seen to tilt increasingly for higher ethanol concentrations. The same reasoning as for the freezing process can be employed to explain this trend. That the temperature inside the sample is lower than that outside means that the endothermic thawing is more efficient at removing heat than what can be transferred from the bath fluid. This effect becomes more prominent for lower concentrations, as the change in ethanol concentration during melting is reduced. The tabulated melting points for the different concentrations are indicated with grey lines [39]. For pure water and the 5% sample, the estimated melting temperatures from the FBG sensor are approximately 0.3°C below the expected. The higher concentrations have a wider melting interval and the concentration in the liquid phase changes faster during melting. This makes it more difficult to determine the exact melting temperatures, but it also shows the importance of measuring the actual conditions when the temperature is scanned across the phase-transition interval.

The WL of dip 1 (TC sensor) in Fig. 3 is shown in Fig. 9 for selected ethanol concentrations. The measurement series is the same as what was presented in Fig. 7, but only the WL of the TC sensor is shown. Contrary to the results for pure water (Fig. 5), the WL shows a strong red-shifts upon freezing in the binary ethanol mixtures. The freezing event can be identified by the strong red-shift at the low-temperature end of each line. As was seen in Fig. 7, the 25% sample freezes during the heating stage, and the 30% sample does not freeze at all. When the samples are re-heated, the wavelength of the dip blue-shifts and ends up just below the liquid line.

The red-shift upon freezing can theoretically be described by either an increase in external RI or by strain.

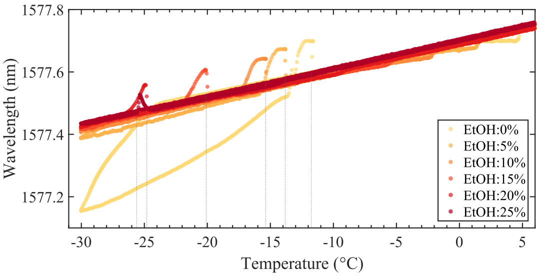

Figure 7: The FBG peak wavelength shifts as a function of bath temperature for ethanol concentrations 0-25%. For higher concentrations, the freezing temperature is lowered. The 30% sample did not freeze and is therefore not shown, whereas the 25% sample froze first during the reheating phase.

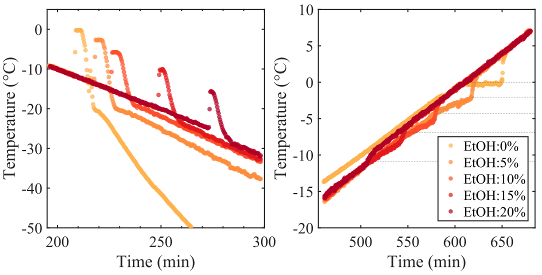

Figure 8: The calculated local temperature within the sample for ethanol concentrations 0-20%, calculated by using the data prior to freezing as a baseline. Strain effects in the pure water sample causes a large disparity in the temperature estimation after freezing. The same but moderate effect can be seen in the 5% sample. The estimated melting temperatures can be compared to literature values indicated with grey lines.

However, from Fig. 7 it is reasonable to conclude that only the pure water and the 5% ethanol sample are significantly affected by strain imparted by the solid phase. Because of the opposite sensitivity to strain, the small strain seen for low ethanol concentrations would red-shift the TC wavelength approximately an equal amount. Also, for higher ethanol concentrations, the transition back to the liquid phase becomes more smooth. Because of the geometry of the setup, where the heat transfer goes radially outwards through the test tube, the optical sensors are expected to be slightly warmer than the sample as they extend out of the temperature bath into room temperature. Since the solid phase is expected to be pure ice [11, 13], it is therefore reasonable to assume that a concentrated ethanol mixture is left around the sensors. This assumption is supported by the fact that at -30°C there will still be concentrated liquid present, which will be true for temperatures above the eutectic. At the lowest temperature measured, it is therefore expected that the remaining liquid phase has an ethanol concentration of around 40% [39]. If pure ice were to surround the sensor, the blue-shift seen in Fig. 5 would be expected. This theory may also explain why the dip appears at slightly shorter WLs during the heating, compared to the cooling line. Due to the concentrated liquid phase that remains after the liquid-to-solid transition, ethanol evaporation may have occurred. This is supported by the 30% line which does not show the hysteresis. To estimate the melting temperatures from these results is difficult since the temperature is measured outside the sample, which was shown to differ from that inside.

This motivates a further analysis of the origin of the increased RI after freezing, which will be done in the following section.

3.3. Analysis of post-freeze results

By utilizing the curves prior to freezing, the wavelength shift as a function of ethanol concentration was found, at each temperature. With the assumption that the sensor always is in contact with a liquid phase, also after freezing, the ethanol concentration in the remaining liquid was calculated. The calculation followed these steps:

1. Each wavelength curve in Fig. 9 was fitted to a second-degree polynomial, using the data from 30°C down to each respective freezing point.
2. The fitted functions were extrapolated down to -30°C.
3. At each temperature step, a new function was found that describe the wavelength as a function of ethanol concentration.
4. A new vector was created from the 30% ethanol data shown in Fig. 8, which contain the estimated temperature inside the sample measured with the FBG sensor.
5. The temperatures from Step 4 were then used to find the actual ethanol concentration from the function defined in Step 3.
6. The resulting concentration was plotted as a function of the temperature measured inside the sample.

The resulting concentrations are shown in Fig. 10, together with the tabulated melting points of ethanol water mixtures from Lange's Handbook of Chemistry [39]. The estimated temperature from the FBG sensor inside the sample is plotted on the horizontal axis.

In the liquid phase the concentrations are constant, as is expected since this is the data that was used to calibrate the estimation. The amount of undercooling for each concentration is the difference between the lowest temperature of the horizontal (liquid) line and the tabulated melting points shown in black. For the concentrations 5-20%, the undercooling increases from 10 to 14°C, see Table 1. Following this trend, the 25% sample is expected to freeze at approximately -30°C, but in this case it did not overcome the nucleation barrier until later during the re-heating. This highlights the statistical nature of the phase transition.

The underestimation of the temperature from the FBG-sensor in the solid phase causes an underestimation of the ethanol concentrations on the same interval. However, the opposite strain effect on the TC-sensor will partly compensate for this effect. If the assumption of pure water in the solid phase is correct, the lines in Fig. 10 should therefore follow the tabulated melting points after freezing. That some of the lines (lower concentrations) lie below the tabulated data means that the average RI around the fiber is lower than what is expected. The reason for this is difficult to conclude, but it may indicate that the ice phase exists close enough to the fiber to displace some of the concentrated ethanol solution. This may also explain the increased deviation from the tabulated values at lower temperatures, where more of the remaining liquid around the fiber freezes. Air bubbles trapped close to the fiber would also decrease the effective concentration measured. The release of air bubbles may be the reason for the more erratic behavior of the 0% and 5% samples during melting, but does not explain the increased deviation at lower temperatures. Simulations done in previous work [24], show that the half-length of the evanescent field is 4-500 nm (optical intensity: ∼350 nm), which defines the volume around the fiber that is probed. The sensor measures the average RI in this volume, and the effect is therefore a local phenomenon.

Upon heating, the estimated concentrations eventually approach and coincide within 0.1°C of the tabulated melting values. This may indicate that the ice closest to the sensors has melted and left only liquid in the volume probed by the evanescent field. The combined output from the dual-sensor setup can therefore be expected to be able to estimate melting points, limited by the accuracy of the two sensors and the temperature bath. The temperature measurement showed an RMSE of 0.15°C and the temperature bath is accurate within 0.25°C. Based on the RMSE of the wavelength determination, the sensor should be able

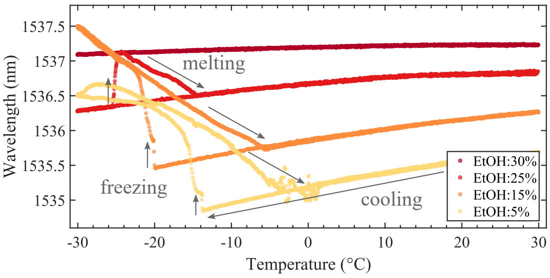

Figure 9: The wavelength shifts of the TC dip as a function of *bath* temperature for selected ethanol concentrations. Because of the increased RI for higher concentrations, the liquid lines appear at higher wavelengths. The decreased sensitivity to temperature at higher concentrations is consistent with the decrease in thermo-optic coefficients [10]. Upon freezing, the dip continues to red-shift after the initial heating. The transition back to the liquid phase becomes more smooth for higher concentrations.

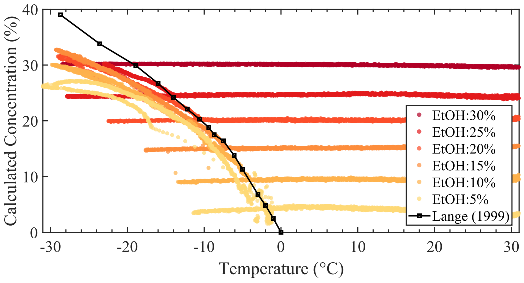

Figure 10: The calculated ethanol concentrations surrounding the fiber-optic sensors before and after freezing, together with tabulated melting temperatures from [39]. In the liquid phase, the concentrations are constant, while after freezing the concentrations become functions of temperature. The horizontal axis shows the temperatures calculated from the FBG sensor output (Fig. 8).

to estimate the ethanol concentration within ±0.1%, but strain and a non-linear RI sensitivity introduces additional errors for both sensors.

As the growth of the solid phase is random, it is also not certain that the two fiber-optic sensors are exposed to the same conditions. Placing both sensors on a single fiber would create a longer probe, but would reduce these uncertainties. The sensor response is also different from experiment to experiment, although the same general behavior can be observed.

Whereas this study has interpreted the sensor-system response based on known properties of the samples, the intended use of a sensor is generally the opposite i.e. to extract unknown information from the sensor response. In situations where the properties of the samples are known approximately, the sensors can aid in measuring or confirming the actual conditions. In most systems, assumptions or prior measurements will aid in understanding the output. Even though the interpretation of most measurements relies on some assumptions or prior measurements, the dual-fiber sensor system also offers some *a priori* information. Both the temperature and RI in the system can be explicitly determined in gasses and liquids, where strain effects can be neglected. In addition, the effective concentration around the sensors and the heat generation/absorption is implicitly given by the RI and temperature. In experimental situations there are also factors that are difficult to control, which affects the progression of phase transitions e.g. heat transfer. Even with the known melting temperatures for aqueous ethanol mixtures used in this study, the dynamic behavior of the samples is difficult to predict. The sensors ability to capture the unique progression of each measurement is therefore paramount in real-life systems.

4. Conclusions

A dual fiber-optic sensor system was presented, and demonstrated to be able to detect and characterize phase transitions in both pure liquids and binary mixtures. Mixtures of ethanol in the range of 0-30% were used to demonstrate the concept. The combination of a multi-mode interferometer with a fiber Bragg grating sensor was used to distinguish between RI, temperature and strain. The interplay between these parameters were used to extract the information that can be obtained about phase transitions, as well as the liquid and solid phases. By identifying the strain-free regions in the FBG sensor response, the changes in external RI can be estimated. This was especially important in the case of pure water, where compressive strain from thermal expansion was found to greatly thwart the temperature measurement. An indisputable explanation for the accelerated strain relaxation during the heating stage was not found, but conductive heat transfer through the fiber may be a contributing factor.

Visually, pure water seems to freeze instantaneously because of the rapid dendritic crystal growth. However, the sensors are able to resolve the transition fully, progressing from a monophasic liquid, through a biphasic liquid-solid state, to the solid state. It was noted that only the pure water exhibits a constant temperature during freezing, whereas the temperature gradually decreases for the ethanol mixtures. The effect is more pronounced for higher concentrations, and is expected due to freezing-point depression in binary mixtures. This is also apparent during melting, where the temperature remains constant until the transition is complete – an effect that becomes less pronounced at higher ethanol concentrations. Due to the dynamic nature of the experiment, the melting temperatures for different concentrations of ethanol were difficult to extract from each one of the two sensors. But through analysis of the combined response of the two sensors, the determined melting points agreed with the tabulated values within the uncertainty of the experiment (0.25°C).

The system was also able to distinguish between pure liquids and binary mixtures, because of the partial freeze-out of the latter. This results in less, or no strain, and an increased concentration (increased RI) in the remaining liquid phase, whereas pure water showed a distinct reduction in RI due to the lower density of ice. The freezing process in pure water and low ethanol concentrations was found to be limited by heat transfer, whereas mass transfer was seen to be the limiting factor in mixtures with higher concentrations. The lack of strain after solidification also enabled an estimate of the concentration in the remaining liquid phase, which was found to lie below the literature values.

The amount of information extracted from the sensor system before, during and after a phase transition, emphasizes the benefits of having a dual-fiber setup.

References

[1] A. Sharma, V. V. Tyagi, C. R. Chen, D. Buddhi, Review on thermal energy storage with phase change materials and applications, Renewable and Sustainable Energy Reviews 13 (2) (2009) 318–345. `doi:10.1016/j.rser.2007.10.005`.

[2] F. G. Qin, A. B. Russell, X. D. Chen, L. Robertson, Ice fouling on a subcooled metal surface examined by thermo-response and electrical conductivity, Journal of Food Engineering 59 (4) (2003) 421–429. `doi:10.1016/S0260-8774(03)00002-5`.

[3] S. Veesler, L. Lafferrère, E. Garcia, C. Hoff, Phase Transitions in Supersaturated Drug Solution, Organic Process Research & Development 7 (6) (2003) 983–989. `doi:10.1021/op034089f`.

[4] Ø. Wilhelmsen, D. Berstad, A. Aasen, P. Nekså, G. Skaugen, Reducing the exergy destruction in the cryogenic heat exchangers of hydrogen liquefaction processes, International Journal of Hydrogen Energy 43 (10) (2018) 5033–5047. `doi:10.1016/j.ijhydene.2018.01.094`.

[5] K. Kvalsvik, D. O. Berstad, Ø. Wilhelmsen, Dynamic modelling of a liquid hydrogen loading cycle from onshore storage to a seaborne tanker, Science et technique du froid Part F1477. `doi:http://dx.doi.org/10.18462/iir.cryo.2019.0019`.

[6] D. Zaragotas, N. T. Liolios, E. Anastassopoulos, Supercooling, ice nucleation and crystal growth: A systematic study in plant samples, Cryobiology 72 (3) (2016) 239–243. `doi:10.1016/j.cryobiol.2016.03.012`.

[7] J. Dudak, J. Zemlicka, J. Karch, M. Patzelt, J. Mrzilkova, P. Zach, Z. Hermanova, J. Kvacek, F. Krejci, High-contrast x-ray micro-radiography and micro-ct of ex-vivo soft tissue murine organs utilizing ethanol fixation and large area photon-counting detector, Scientific reports 6 (2016) 30385. `doi:10.1038/srep30385`.

[8] F. K. Coradin, G. R. Possetti, R. C. Kamikawachi, M. Muller, J. L. Fabris, Etched fiber Bragg gratings sensors for water-ethanol mixtures: A comparative study, Journal of Microwaves and Optoelectronics 9 (2) (2010) 131–143. `doi:10.1590/S2179-10742010000200007`.

[9] N. Nishi, S. Takahashi, M. Matsumoto, A. Tanaka, K. Muraya, T. Takamuku, T. Yamaguchi, Hydrogen-Bonded Cluster Formation and Hydrophobic Solute Association in Aqueous Solutions of Ethanol, The Journal of Physical Chemistry 99 (1) (1995) 462–468. `doi:10.1021/j100001a068`.

[10] S. Novais, M. S. Ferreira, J. L. Pinto, Determination of thermo-optic coefficient of ethanol-water mixtures with optical fiber tip sensor, Optical Fiber Technology 45 (July) (2018) 276–279. `doi:10.1016/j.yofte.2018.08.002`.

[11] K. Takaizumi, T. Wakabayashi, The freezing process in methanol-, ethanol-, and propanol-water systems as revealed by differential scanning calorimetry, Journal of Solution Chemistry 26 (10) (1997) 927–939. `doi:10.1007/BF02768051`.

[12] K. Takaizumi, A curious phenomenon in the freezing-thawing process of aqueous ethanol solution, Journal of Solution Chemistry 34 (5) (2005) 597–612. `doi:10.1007/s10953-005-5595-6`.

[13] S. Facq, F. Danède, B. Chazallon, Ice particle crystallization in the presence of ethanol: An in situ study by Raman and X-ray diffraction, Journal of Physical Chemistry A 117 (23) (2013) 4916–4927. `doi:10.1021/jp4015614`.

[14] K. Koga, H. Yoshizumi, Diffential scanning calorimetry (DSC) studies on the freezing processes of water-ethanol mixtures and distilled spirits, Journal of Food Science 44 (5) (1979) 1386–1389. `doi:10.1111/j.1365-2621.1979.tb06444.x`.

[15] H. J. Borchardt, F. Daniels, The Application of Differential Thermal Analysis to the Study of Reaction Kinetics, Journal of the American Chemical Society 79 (1) (1957) 41–46. `doi:10.1021/ja01558a009`.

[16] R. Anderson, R. Adams, B. Duggins, Limitations of Thermocouples in Temperature Measurements, 25th ISA Anaheim CA (1979) 1–33.

[17] A. Dewaele, J. Eggert, P. Loubeyre, R. Le Toullec, Measurement of refractive index and equation of state in dense He, H2, H2O, and Ne under high pressure in a diamond-anvil cell, Physical Review B 67 (9) (2003) 094112. `doi:10.1103/PhysRevB.67.094112`.

[18] D. Lee, R. Haynes, D. Skeen, Properties of optical fibres at cryogenic temperatures, Monthly Notices of the Royal Astronomical Society 326 (2) (2001) 774–780. `doi:10.1046/j.1365-8711.2001.04630.x`.

[19] W. Han, M. Rebow, X. Lian, D. Liu, G. Farrell, Q. Wu, Y. Ma, Y. Semenova, SNS optical fiber sensor for direct detection of phase transitions in C18H38 n-alkane material, Experimental Thermal and Fluid Science 109 (November 2018) (2019) 109854. `doi:10.1016/j.expthermflusci.2019.109854`.

[20] A. Millo, Y. Raichlin, A. Katzir, Mid-Infrared Fiber-Optic Attenuated Total Reflection Spectroscopy of the Solid—Liquid Phase Transition of Water, Applied Spectroscopy 59 (4) (2005) 460–466. `doi:10.1366/0003702053641469`.

[21] R. Kumar, W. Han, D. Liu, W. P. Ng, R. Binns, K. Busawon, Y. Q. Fu, Z. Ghassemlooy, C. Underwood, K. Mahkamov, J. Yuan, C. Yu, H. Shu, X. A. Li, T. Guo, G. Farrell, Y. Semenova, Q. Wu, Optical fibre sensors for monitoring phase transitions in phase changing materials, Smart Materials and Structures 27 (10) (2018) 105021. `doi:10.1088/1361-665X/aaddba`.

[22] P. Mani, A. Rallapalli, V. R. Machavaram, A. Sivaramakrishna, Monitoring phase changes in supercooled aqueous solutions using an optical fiber Fresnel reflection sensor, Optics Express 24 (5) (2016) 5395. `doi:10.1364/OE.24.005395`.

[23] W. Han, M. Rebow, D. Liu, G. Farrell, Y. Semenova, Q. Wu, Optical fiber Fresnel reflection sensor for direct detection of the solid–liquid phase change in n-octadecane, Measurement Science and Technology 29 (12) (2018) 125107. `doi:10.1088/1361-6501/aaeabb`.

[24] M. S. Wahl, Ø. Wilhelmsen, D. R. Hjelme, Addressing Challenges in Fabricating Reflection-Based Fiber Optic Interferometers, Sensors 19 (18) (2019) 4030. `doi:10.3390/s19184030`.

[25] A. D. Kersey, M. A. Davis, H. J. Patrick, M. LeBlanc, K. P. Koo, Fiber Grating Sensors, Journal of Lightwave Technology 15 (8) (1997) 1442–1463. `doi:10.1109/50.618377`.

[26] S. Tripathi, A. Kumar, R. Varshney, Y. Kumar, E. Marin, J.-P. Meunier, Strain and Temperature Sensing Characteristics of Single-Mode–Multimode–Single-Mode Structures, Journal of Lightwave Technology 27 (13) (2009) 2348–2356. `doi:10.1109/JLT.2008.2008820`.

[27] L. Li, L. Xia, Z. Xie, L. Hao, B. Shuai, D. Liu, In-line fiber Mach–Zehnder interferometer for simultaneous measurement of refractive index and temperature based on thinned fiber, Sensors and Actuators A: Physical 180 (2012) 19–24. `doi:10.1016/j.sna.2012.04.014`.

[28] Y. Saito, J. J. Wang, D. A. Smith, D. N. Batchelder, A Simple Chemical Method for the Preparation of Silver Surfaces for Efficient SERS, Langmuir 18 (8) (2002) 2959–2961. `doi:10.1021/la011554y`.

[29] R. C. Kamikawachi, I. Abe, A. S. Paterno, H. J. Kalinowski, M. Muller, J. L. Pinto, J. L. Fabris, Determination of thermo-optic coefficient in liquids with fiber Bragg grating refractome-

ter, Optics Communications 281 (4) (2008) 621–625. `doi:10.1016/j.optcom.2007.10.023`.

[30] E. S. d. L. Filho, M. D. Baiad, M. Gagné, R. Kashyap, Fiber Bragg gratings for low-temperature measurement, Optics Express 22 (22) (2014) 27681. `doi:10.1364/oe.22.027681`.

[31] A. H. Harvey, J. S. Gallagher, J. M. H. L. Sengers, Revised Formulation for the Refractive Index of Water and Steam as a Function of Wavelength, Temperature and Density, Journal of Physical and Chemical Reference Data 27 (4) (1998) 761–774. `doi:10.1063/1.556029`.

[32] N. E. Dorsey, Supercooling and freezing of water, US Department of Commerce, 1938.

[33] H. Kumano, T. Asaoka, A. Saito, S. Okawa, Study on latent heat of fusion of ice in aqueous solutions, International Journal of Refrigeration 30 (2) (2007) 267–273. `doi:10.1016/j.ijrefrig.2006.07.008`.

[34] S. Fukusako, M. Yamada, A. Horibe, H. Kawai, Solidification of aqueous binary solution on a vertical cooled plate with main flow, Heat and Mass Transfer 30 (3) (1995) 127–134. `doi:10.1007/BF01476520`.

[35] C. Tangthieng, F. B. Cheung, S. W. Shiah, Behavior of the Two-Phase Mushy Zone During Freeze Coating on a Continuous Moving Plate, Journal of Heat Transfer 124 (1) (2002) 111–119. `doi:10.1115/1.1420714`.

[36] N. E. Dorsey, The freezing of supercooled water, Transactions of the American Philosophical Society 38 (3) (1948) 247–328.

[37] T. R. Butkovich, Thermal expansion of ice, Journal of Applied Physics 30 (3) (1959) 350–353. `doi:10.1063/1.1735166`.

[38] J. Zhou, C. Liao, Y. Wang, G. Yin, X. Zhong, K. Yang, B. Sun, G. Wang, Z. Li, Simultaneous measurement of strain and temperature by employing fiber Mach-Zehnder interferometer, Optics Express 22 (2) (2014) 1680. `doi:10.1364/oe.22.001680`.

[39] J. A. Lange, Lange's handbook of chemistry, 15th Edition, McGraw-Hill, Inc., New York, 1999.

[40] S. Rivkin, A. Winnikova, Die spezifischen Wärmen wässeriger Lösungen von Äthylalkohol, Chemie IngenieurTechnik 37 (1965) 557–557.

PAPER III

Ice formation and growth in supercooled water–alcohol mixtures: Theory and experiments with dual fiber sensors

Markus Solberg Wahl[a], Ailo Aasen[b,c], Dag Roar Hjelme[a], Øivind Wilhelmsen[b,c,*]

[a]*Norwegian University of Science and Technology (NTNU), Department of Electronic Systems, 7491 Trondheim, Norway*
[b]*Norwegian University of Science and Technology (NTNU), Department of Energy and Process Engineering, 7491 Trondheim, Norway*
[c]*SINTEF Energy Research, 7034 Trondheim, Norway*

Abstract

Increased knowledge on fluid-solid phase transitions is needed, both when they are undesired and can impair processes operation, and when strict control is required in fields such as food technology, the pharmaceutical industry and cryogenic CO_2 capture. We present experimental results and theoretical predictions for the solid-formation and melting temperatures of ice in four binary water–alcohol mixtures containing methanol, ethanol, 1-propanol and 1-butanol. A dual fiber sensor set-up with a fiber Bragg grating sensor and a thin-core interferometer is used to detect the solid-formation. The predictions of melting temperatures with the cubic plus association equation of state combined with an ice model are in good agreement with experiments, but deviations are observed at higher alcohol concentrations. The measured degree of supercooling displays a highly non-linear dependence on the alcohol concentration. A heterogeneous nucleation model is developed to predict the solid-formation temperatures of the binary alcohol–water mixtures. The predictions from this model are in reasonable agreement with the measurements, but follow a qualitatively different trend that results in systematic deviations. In particular, the predicted degree of supercooling is found to be an essentially colligative property that increases smoothly with alcohol concentration. Experimental results are also presented for the growth rate of ice crystals in water–ethanol mixtures. For pure water, the measured crystal growth rate is 10.2 cm/s at 16 K supercooling. This is in excellent agreement with previous results from the literature. The crystal growth rate observed in ethanol–water mixtures however, can be orders of magnitude lower, where a mixture with 2% mole fraction ethanol has a growth rate of 2 mm/s. Further work is required to explain the large reduction in crystal growth rate with increasing alcohol concentration and to reproduce the behavior of the solid-formation temperatures with heterogeneous nucleation theory.

Keywords: Heterogeneous nucleation, phase transitions, multimode interference, fiber-optic sensors

---

1. Introduction

It is important to predict and control the formation of a solid-phase in numerous industries. Precipitation of inorganic salts from aqueous solutions can impair operation of heat exchangers and production of oil and natural gas, which causes significant economical losses in the industry [1, 2]. Aggregate-state control is also important in novel process configurations for liquefaction of hydrogen that involve helium–neon mixtures [3]. Precipitation of solid CO_2 from natural gas mixtures must be controlled to avoid constricting or plugging pipelines, which can cause a sudden and dangerous increase in pressure [4, 5]. Although CO_2-frosting is mostly seen as a detrimental effect, it can also be used to separate the unwanted gas from the natural gas mixture [6]. Increased knowledge about phase transitions is important both when they are undesired, and when strict control is needed e.g. in fields such as energy storage systems based on latent heat [7], in food technology [8], to select the desired crystal polymorph in the pharmaceutical industry [9–11], and in biology and intercellular freezing [12–14].

Nucleation refers to the first step in most phase transitions and the formation of an incipient portion of the new phase [15]. In solid-formation, a critical cluster forms by means of thermal fluctuations, either in the bulk of the fluid (homogeneous nucleation), or aided by external surfaces (heterogeneous nucleation). Many experimental and modelling studies have been committed to explore and understand the mechanisms of nucleation [16–20].

In pure water, homogeneous nucleation of solid crystals has been observed down to −40°C [18]. In most practical situations however, the nucleation is heterogeneous. This means that impurities in the liquid or surfaces in contact with the fluid promote nucleation by lowering the activation barrier [21]. The molecular dynamic simulations by Sanz et al. showed that nucleation in pure water occurring less than 20 K below the melting point must be heterogeneous

---

[*] Corresponding author
Email address: `oivind.wilhelmsen@ntnu.no` (Øivind Wilhelmsen)

[22]. Which materials that promote or inhibit nucleation has been widely studied, but not yet fully understood [19, 21, 23–28]. Fitzner et al. found that both surface morphology and hydrophobicity are important factors [19].

Due to the activation barrier required to make the first critical cluster, the solid-formation temperature is always below the tabulated melting temperature. For accurate control of precipitation in fluid mixtures, it is of interest to predict and understand at precisely which temperature the solid forms. In this work, we will study the solid-formation temperature and the degree of supercooling that can be achieved in binary water–alcohol mixtures, by use of experiments and theory. Short-chained alcohols have been chosen as examples because they are miscible in both polar and non-polar substances, which makes them versatile solvents [29].

In Ref. [30], the limit of superheating of liquids prior to formation of vapor was predicted to a high accuracy with homogeneous nucleation theory, both for single-component fluids and mixtures. This motivates a hypothesis to be explored in the present work, namely that the solid-formation temperature and the degree of supercooling in mixtures can be predicted by use of heterogeneous nucleation theory for solids. The supercooling is here defined as the difference between the melting temperature and the measured solid-formation temperature.

The theoretical predictions of the liquid-solid phase transition will be compared to experiments. Phase transitions have traditionally been studied through differential scanning calorimetry [31, 32] and differential thermal analysis [14, 33]. These techniques offer invaluable information on the thermophysical properties of phase transitions, but are traditionally not suited for accurate detection of solid-formation because of their slow response. The increase in temperature due to the release of latent heat can be measured with electronic temperature sensors (e.g. thermocouples, Pt100) [5]. However, because these sensors may act as heat sinks/sources, the accuracy is impaired [34]. Phase transitions can also be observed visually in transparent materials [14, 20, 35, 36]. This is arguably the most accurate of the methods discussed so far. However, transparent containers or windows are necessary, which may not always be experimentally feasible.

Apart from visual methods to detect the onset of phase transitions, most methods are designed to monitor and analyse how the transition progresses. With fiber-optic sensor probes, the solid-formation can be detected directly, either through a change in refractive index or through an associated increase in temperature. Due to their small size and thermal mass, the influence on the measurement is low. Fiber-optic sensors are also chemically inert and mechanically robust, even at cryogenic temperatures [37]. This has in recent years triggered studies into using fiber-optic sensors to detect and study phase transitions [2, 38–42]. Han et al. utilized the special properties of n-octadecane, which has refractive indices above and below that of the fiber in the solid and liquid phase, respectively. This enabled discrimination between the phases based on a guiding or no-guiding condition, which was demonstrated both with a multi-mode fiber interferometer [42] and a Fresnel reflection probe [40]. Mani et al. also used a Fresnel reflection probe to detect solid-formation in aqueous NaCl-solutions. Since only the fiber end-face is in contact with the sample, these point measurements are mechanically very robust, but at the same time sensitive to impurities or bubbles present. Boerkamp et al. measured the rate of crystal growth in $CaCO_3$ scale formation with exposed-core fibers, where the increased scale thickness gradually attenuated the transmitted light [2, 38].

In this work, we will use a set-up with a boroscope and two fiber-optic sensors to detect both the solid-formation temperature and the growth rate of the resulting crystal. Details on the experimental set-up and methodology are given in Sec. 2. Next, the theory to predict the melting and solid-formation temperatures of mixtures is presented in Sec. 3. Theoretical predictions are compared to experiments in Sec. 4 before concluding remarks are provided in Sec. 5.

2. Experimental

A schematic of the experimental setup used in this work is shown in Fig. 1. A temperature bath with silicon oil (Hart Scientific, 7103 Micro-bath) and an accuracy of 0.25 K was used to control the temperature. The temperature bath is limited to temperatures above -30°C, which puts a constraint on the range where solid-formation events have been studied. A calibrated temperature sensor (Pt100, 3-wire) with a stainless steel sheath was placed in the bath fluid for confirmation purposes. The test tube containing the sample was placed at the center of the bath, with the sample 10 cm below the silicon oil surface. The open end of the test tube was covered with aluminum foil to reduce losses of heat and mass to the ambient while maintaining atmospheric pressure. Two different test tubes were used, one of glass (Borosil, 27 mL) and one of polypropylene (VWR, 14 mL). The two fiber-optic sensors were secured at positions 1 mm apart, near the center of the sample liquid (see Fig. 1). For visual inspection, a digital boroscope was used to capture images and video. For some of the experiments, the frames of the videos were analysed to measure the size of the growing crystal as a function of time. Further details on this procedure have been included in the supplementary information (SI).

2.1. Fiber-optic detection

The fiber-optic sensor setup is shown in Fig. 1 (right). It consists of a fiber Bragg grating (FBG) sensor, which is sensitive to temperature (T) and strain (ε), and a thin-core (TC) fiber interferometer that is also sensitive to the refractive index (RI) of the surrounding medium (sample). The light source is a broadband laser (FYLA, SCT500), and a grating-based spectrometer (Ibsen, I-MON 512) has been used to capture the combined spectrum from the two sensors. These components are connected through a 2x2 50:50 single-mode coupler (Thorlabs, TW1550R5A2). The FBG signal is also attenuated with a variable fiber-optic attenuator to achieve comparable intensitites from the two sensors.

FBG sensors reflect light at the wavelength given by [43]

$$\lambda_B = 2n_{eff}\Lambda, \tag{1}$$

where n_{eff} is the effective RI of the grating and Λ is the grating period. The sensor used (Optromix) is inscribed in an SM1500 fiber, and the reflected wavelength has a full-width half-maximum of 0.2 nm and a reflectivity of 79%. The wavelength shifts as a function of temperature due to thermal expansion and the thermo-optic effect, where the latter accounts for $\sim$ 95% of the sensitivity [43]. This can be expressed as [44]

$$\Delta\lambda_B = \lambda_B(\alpha + \xi)\Delta T, \tag{2}$$

where α is the thermal expansion coefficient, and ξ is the thermo-optic coefficient.

The TC interferometer is fabricated by splicing a 14.2 mm section of TC fiber (SM400) fiber to the end of a single-mode fiber (SMF-28). A silver mirror was deposited at the fiber end-face with the mirror reaction [45], to increase the reflected signal. The mismatch between the cores of the two fibers enables the excitation of an ensemble of cladding modes [46] in the TC fiber, which create an interference spectrum when they are reflected back to the spectrometer. The interference spectrum exhibits characteristic intensity minima, where the modes interfere destructively. This can be expressed as

$$\lambda_{dip,i} = \frac{4L\left[n_{eff}(\lambda, n_{ext}) - n'_{eff}(\lambda, n_{ext})\right]}{2i-1}, \tag{3}$$

where L is the length of the interferometer, n_{eff} and $n'_{eff}$is the effective index of two modes at wavelength λ and external (sample) RI (n_{ext}). Because the modes are bound by the outer diameter of the fiber, the evanescent field causes the effective indices to be functions of the surrounding RI, as well as the temperature of the sensor.

The dual-sensor configuration enables an independent temperature measurement and a characterization of both the liquid and solid phases. In phase transitions with a low associated latent heat, the TC sensor also enables detection based on changes in the RI.

2.2. Data acquisition and analysis

To control the temperature setpoints and scan rate, an in-house LabVIEW program was developed, which acquires data from the temperature sensors and the spectrometer. The combined spectrum from the two sensors was stored together with the temperature reading every 30 seconds during cooling. Around the expected solid formation temperature, the acquisition rate was increased to every 10 seconds.

A typical output spectrum from an experiment is shown in Fig. 2. Here, the FBG peak and the three main TC dips are marked with circles. Only the FBG peak and the first dip of the TC fiber were used for further analysis. Post-processing was performed to determine the exact wavelengths of these features. The FBG peak was fitted to a Gauss function, whereas the first TC dip was fitted to a polynomial. By tracking these wavelengths as a function of time and temperature, the event of solid formation can be identified.

2.3. Sample preparation

To prepare the samples, deionized (DI) water (< 1.5 μS/cm) was mixed with methanol/ethanol/1-propanol/1-butanol by weight. Concentrations from 0% to 30% (weight) were prepared in intervals of 5%. Because of the limited solubility of butanol in water, only concentrations of 2.5%, 5% and 7.5% were used for the butanol–water mixture. The maximum error estimated for the prepared concentrations was 0.4%, based on the uncertainty disclosed by the manufacturer. The concentrations will be referenced according to their corresponding mol% in the discussion, as colligative effects of the solute are expected to be important.

After preparing the mixtures, the solutions were heated to 50°C for 5 hours and stored at room temperature for one week to let them equilibrate [47]. The test tube and fiber-optic sensors were rinsed with acetone, 96% ethanol and DI water before each measurement to remove any contaminants. For the polypropylene test tube, the rinsing procedure influenced the results; this will be further discussed in Sec. 4. The test tube was filled with 6 mL from the sample solution and stabilized at 30°C for 15 min. Next, the fiber-optic sensors were inserted prior to lowering the temperature down to -30°C at 0.2°C/min.

3. Theory

For the mixtures and conditions considered in the present work, the solid-phase crystallizes as pure H_2O [31] with a hexagonal crystal structure known as ice I_h [31, 32, 48]. The first crystal forms after a certain degree of supercooling by heterogeneous nucleation on the container walls or on the two sensors. A hypothesis that will be explored in this work is that the solid-formation temperature can be determined by heterogeneous nucleation theory. Upon heating, the crystal starts to dissolve at the melting point, i.e. there is no superheating of the crystal. The melting point represents an equilibrium configuration between the fluid and the solid. In the following, we shall elaborate how to determine both the melting temperature (Sec. 3.2) and the solid-formation temperature (Sec. 3.3) by combining theoretical predictions with an equation of state (Sec. 3.1).

3.1. Equations of state for the liquid and the ice

The cubic plus association (CPA) equation of state (EoS) [49] was used to model the liquid phase, with published pure-component parameters from Queimada et al. [50]

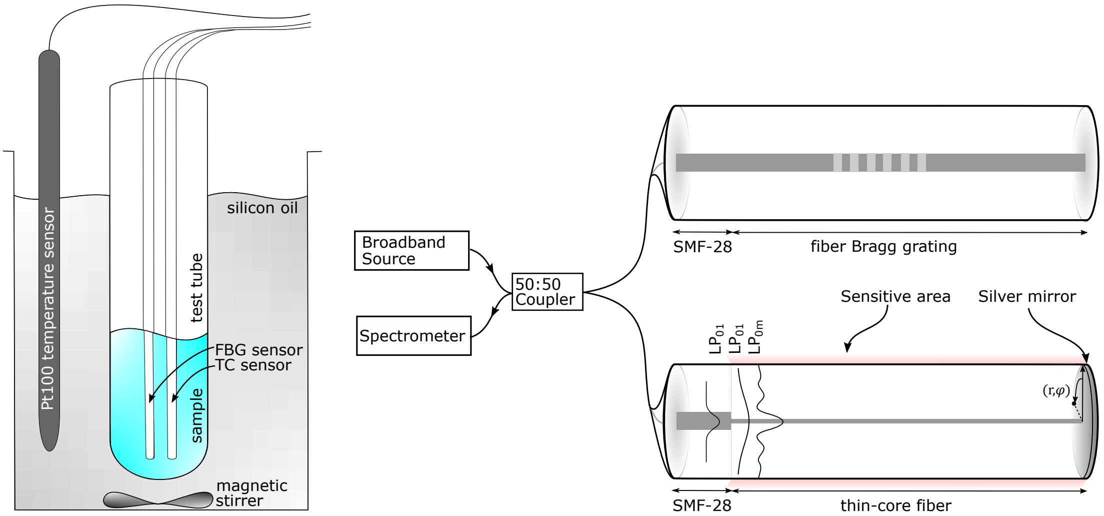

(a) Measurement rig.

(b) Fiber-optic sensor configuration.

Figure 1: A schematic of the experimental set-up (a), which consists of a temperature bath with silicon oil as cooling medium. An electrical Pt100 temperature sensor is used for confirmation. The two sensors are secured at the centre of the test tube that holds the sample. The fiber-optic configuration (b) consists of a broadband source and a spectrometer, which are connected to the two sensors with a 50:50 fiber-optic coupler. The lines connecting the components are all single-mode fibers (SMF-28).

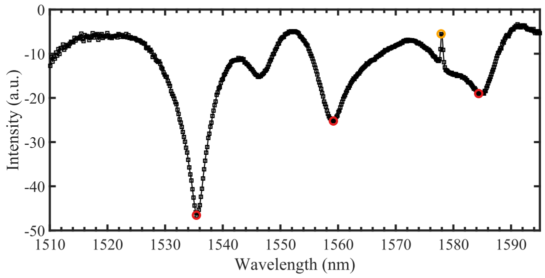

Figure 2: A typical output spectrum, showing the sum of the reflected intensities from the two sensors as a function of wavelength. Three interference minima (dips) are identified, but only the first is used in interpreting the response. The peak from the FBG sensor has been attenuated as to not saturate the spectrometer, while ensuring acceptable visibility of the interference spectrum. The features of both sensors shift to longer wavelength (red-shift) with increasing temperature. The TC sensor red-shifts for increasing external refractive index.

for water and Oliveira et al. [51] for alcohols. The CPA EoS requires a binary interaction parameter, k_{ij}, to be fitted by use of thermodynamic properties of the binary system considered. This parameter was set to $k_{ij} = -0.1$ for methanol–water and propanol–water, and to $k_{ij} = -0.115$ for ethanol–water and butanol–water; these parameters were validated against experimental vapor–liquid equilibrium composition and density data [52–55]. The CPA equation of state with these parameters has been thoroughly validated in vapor–liquid nucleation studies of water and alcohols [56, 57]. Further details and comparisons to experimental data can be found in the SI.

The Gibbs energy of ice I_h was modeled using the equation of state by Feistel and Wagner [58]. The EoS has two adjustable parameters, g_{00} and s_0, corresponding to the reference state for used for Gibbs energy and entropy at 0 K and 1 atmosphere [58]. These parameters were determined from two conditions: (1) reproducing the experimental triple point temperature and pressure (273.16 K and 611.66 Pa) with the combined CPA+Ice model; (2) the enthalpy of fusion at the triple point calculated from the CPA+Ice model equals the experimental value (6007 J/mol). The resulting values were $g_{00} = -2582.47$ kJ/kg and $s_0 = -1483.02$ J/(kg K).

3.2. The melting point

The melting temperature T_{melt} of the mixture was determined by solving for the temperature T that yields equal chemical potential of water in the liquid mixture and in the ice I_h phase:

$$\mu_w^{\text{liq}}(T, P^{\text{atm}}, x) = \mu_w^{\text{ice}}(T, P^{\text{atm}}), \qquad (4)$$

where P^{atm} is the atmospheric pressure and x is the mole fraction of alcohol in the liquid mixture. The thermodynamic algorithms related to phase equilibrium were solved by using the in-house thermodynamic framework presented in Ref. [59].

3.3. Heterogeneous nucleation theory for predicting the solid-formation temperature

In liquid mixtures below the saturation temperature, solid clusters form and dissipate continuously by means of thermal fluctuations. Nucleation occurs when a cluster permanently exceeds the critical size, R_c, after which further growth is spontaneous. If the critical cluster forms on the container walls or on the fiber, it is referred to as heterogeneous nucleation. If it forms in the bulk of the fluid, it is referred to as homogeneous nucleation. Spontaneous growth of the cluster occurs when the energy reduction of increasing the volume exceeds the energy cost of increasing the surface area. The rate of nucleation events can be expressed by the Arrhenius equation

$$J = J_{\text{kin}} \exp\left(-\frac{W}{k_B T}\right), \qquad (5)$$

where the kinetic prefactor, J_{kin}, describes the rate of cluster formation in the absence of a thermodynamic free energy barrier. For heterogeneous nucleation on a wall, the nucleation rate scales linearly with the wall area, and the units of J are therefore [particles/m^{2}s]. The exponential factor captures how the rate is limited by the nucleation barrier, given by the work of formation, W, required to create clusters large enough to grow spontaneously. For heterogeneous nucleation, the work of formation can be written as [15, 60]

$$W = f_{\text{het}} W^{\text{hom}}, \qquad (6)$$

where W^{hom} is the corresponding work of formation for homogeneous nucleation, and f_{het} is the heterogeneity factor. The value of f_{het} depends on the surface topology of the container as well as the difference in surface energies of the container–liquid and the container–ice interfaces [15]. These surface energies are non-trivial to estimate. In this work, we assume f_{het} to be temperature-independent, concentration-independent, and equal to that of *pure* water in the given container. The heterogeneity factor is thus assumed to depend only on the container type. The quality of this assumption will be discussed in Sec. 4.

We assume the nucleation process to be isothermal. This is usually a good assumption, even for condensation from dense water+alcohol vapors [56, 57], for which the latent heat for phase change is larger and the cooling rate of nuclei is likely lower than for crystallization. Furthermore, a recent simulation study also found that the dynamics of ice growth is not affected by heat dissipation [61].

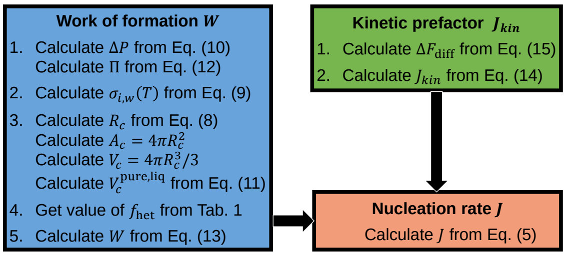

Figure 3: Flowchart of the calculation procedure to obtain the nucleation rate.

We next describe how to calculate J_{kin} and W. For convenience we have also included a flowchart of the calculation procedure in Fig. 3.

The work of formation for homogeneous crystallization in *pure* water is given by [15]

$$W^{\text{hom}} = -\Delta P V_c + A_c \sigma_{i,w}, \qquad (7)$$

where $V_c = 4\pi R_c^3/3$ and $A_c = 4\pi R_c^2$ are the volume and surface area of the critical ice cluster. The critical cluster is assumed to be spherical, with the radius given by the Young–Laplace equation

$$R_c = \frac{2\sigma_{i,w}}{\Delta P}. \qquad (8)$$

Here, $\sigma_{i,w}$ is the surface energy between the ice and the liquid water, and ΔP is the pressure difference between the interior of the critical cluster and the surrounding liquid. The surface energy depends on R_c [62], which in the theoretical framework is a unique function of T. In this work, we assume that the surface energy of the critical ice crystal depends linearly on temperature as

$$\sigma_{i/w}(T) = \sigma_{i/w}(T_0) + a(T - T_0), \qquad (9)$$

where $T_0 = 273.15$ K. Following previous works [63, 64], we use the values $\sigma_{i/w}(T_0) = 29.1$ mN/m, and $a = 0.2$ mN/(K m). We assume the surface energy to be independent of the crystal plane, which is a reasonable approximation for water according to Espinosa et al. [65].

The critical ice cluster has the same chemical potential as the water in the liquid phase, but will be at a higher pressure due to the Young–Laplace equation (Eq. 8). For a given supercooled liquid mixture at temperature $T < T_{\text{melt}}$, the pressure increase ΔP of the critical cluster is found by solving for equality of chemical potentials of water in the two phases:

$$\mu_w^{\text{liq}}(T, P^{\text{atm}}, x) = \mu_w^{\text{ice}}(T, P^{\text{atm}} + \Delta P), \qquad (10)$$

3.3.1. The heterogeneous nucleation barrier

The formation of solids will in most cases be catalysed by the container surface, where the container–liquid interaction reduces the nucleation barrier. The magnitude of the reduction depends on both the surface topology and the hydrophobicity of the container surface [19].

To estimate the work of formation is a crucial step of crystallization theory [63]. Since the work of formation is a difference between two state functions, it can be calculated by adding up free energy differences along any path between the initial and end states. A convenient path through the thermodynamic state space from the liquid mixture (initial state) to the critical cluster (end state) can be described as follows:

(a) Remove all alcohol molecules from the volume $V_c^{\text{pure,liq}}$ occupied by the number of water molecules that will be in the critical ice cluster.
(b) Form ice from the pure, supercooled water. The energy of Step (b) corresponds to the work of formation of a critical cluster of ice in supercooled, pure water.
(c) Re-equilibrate the ice crystal with the solution.

The energy difference of Step (a) is given by $\Pi V_c^{\text{pure,liq}}$ [64, 66], where $\Pi > 0$ is the osmotic pressure across a membrane that is semipermeable to water and that encloses a volume , given by $V_c^{\text{pure,liq}}$ of pure water. The volume that is cleared from alcohol molecules in Step (a) is given by

$$V_c^{\text{pure,liq}} = V_c v_w^{\text{liq,pure}} / v^{ice}, \tag{11}$$

where $v_w^{\text{liq,pure}}$ and v^{ice} are the molar volumes of pure water and ice Ih, respectively. These were computed from the two EoS described in Sec. 3.1, at the supercooled state temperature T. The osmotic pressure Π was computed by identifying the pressure of pure water that gives the same chemical potential as the chemical potential of water in the liquid mixture, the latter being at atmospheric pressure:

$$\mu_w^{\text{liq}}(T, P^{\text{atm}} - \Pi, 0) = \mu_w^{\text{liq}}(T, P^{\text{atm}}, x). \tag{12}$$

The energy difference of Step (b) is given by the usual expression for the work of formation for a critical cluster of ice in pure water (Eq. 7). The energy difference of Step (c) was assumed to be small compared to the energy differences of Steps (a) and (b) and hence omitted; although this is a common approach in the literature [64, 66], the quality of this approximation is unknown.

The final expression for the work of formation is thus

$$W = (\Pi V_c^{\text{pure,liq}} - (\Delta P) V_c + A_c \sigma_{i,w}) f_{\text{het}}, \tag{13}$$

where V_c, A_c and $\sigma_{i/w}$ are computed by using Eqs. (8)–(9), and ΔP is given by the condition of equal chemical potential of water in the liquid solution (at atmospheric pressure P_{atm}), and in the ice (at pressure $P_{\text{atm}} + \Delta P$).

3.3.2. The kinetic prefactor and ice growth

The kinetic prefactor in Eq. 5 describes the rate of diffusion across the solid–liquid interface, and is modeled by [67]

$$J_{kin} = N_c \frac{k_B T}{h} \exp\left[-\frac{\Delta F_{\text{diff}}}{k_B T}\right]. \tag{14}$$

In Eq. (14), h is Planck's constant, N_c is the number of water molecules in contact with the container wall per unit area, and ΔF_{diff} is the activation energy for transport across the surface of the critical cluster. In pure water, this activation energy is often estimated by relating it to the self-diffusivity of water $D = D_0 \exp(-\Delta F_{\text{diff}}/k_B T)$, where D_0 is approximately independent of temperature. Although the self-diffusivity in water is usually lower in alcohol–water mixtures than in pure water, we will approximate it by its value in pure water. We numerically verified that this did not significantly alter the predictions of the solid-formation temperature. For the ethanol–water mixture, we found that a 50% increase in the activation energy for diffusion of water lowers the supercool limit by less than 1 K.

For pure water, we used the value $N_c = 5.85 \times 10^{18}$ m^{-2} [63, 67]. In mixtures, this was multiplied by the mole fraction of water. The activation energy for transport across the surface was estimated following Zobrist et al. [60]:

$$\Delta F_{\text{diff}}(T) = \frac{k_B T^2 E}{(T - T_0)^2}, \tag{15}$$

where the values $T_0 = 118$ K and $E = 892$ K were taken from Smith and Kay [68].

The self-diffusion of water affects the rate of crystal growth, $u(T)$ [m/s], which is a function of temperature. This can be estimated with Wilson–Frenkel theory [61, 69]:

$$u(T) = \frac{D(T)}{a}\left[1 - \exp\left(-\frac{|\Delta \mu_w(T)|}{k_B T}\right)\right], \tag{16}$$

where $D(T)$ is the self-diffusion coefficient of water in the mixture, and a is a characteristic length scale on the order of the diameter of a water molecule that was estimated as 3 Å, in accordance with Ref. [61]. Moreover, $\Delta \mu_w$ is the difference in chemical potential of water in the two phases, both at atmospheric pressure. The quantities in Eq. (16) are evaluated at the solid-formation temperature, T. Although freezing of ice is an exothermic process, molecular simulations indicate that the heat is dissipated sufficiently fast so as to not impact the growth dynamics [61].

3.3.3. The solid-formation temperature

Once the nucleation barrier has been found and the kinetic prefactors have been estimated, the nucleation rate can be calculated from Eq. 5. However, to set a specific limit for a supercooling temperature when the solid forms, one must decide on a *critical* nucleation rate that represents the observed sudden phase change. The critical nucleation rate must be chosen with the cooling rate in mind. In this work, we have used that $N_{\text{crit}} = 1$ s^{-1}, where N_{crit} denotes the rate at which critical clusters are formed. Given a value for N_{crit}, we find the solid formation temperature by solving

$$J(T)A_{\mathrm{container}} = N_{\mathrm{crit}}, \tag{17}$$

where $A_{\mathrm{container}} \approx 0.001\ \mathrm{m}^2$ is the wetted area of the container. Similar to the superheating temperatures determined in Ref. [30], the exact value of N_{crit} had a small influence on the prediction of the temperature where a sudden phase change occurs. We emphasize that N_{crit} does not represent the actual experimental rate. Since the exact value for N_{crit} has a small influence on the predicted solid-formation temperature, we need to ensure that N_{crit} is similar to the experimental nucleation rates. This is true for $N_{\mathrm{crit}} = 1\ \mathrm{s}^{-1}$, since one second is a characteristic time scale that is lower than the cooling rate, but high enough to expect a nucleation event on the time-scale of the solid-formation detection.

3.4. Latent heat of solid-formation

The latent heat released during ice formation limits the amount of ice that can be produced without additional heat dissipating out of the container. Immediately after the solid formation, the system can be approximated to be adiabatic. This allows the amount of ice to be estimated with the following energy balance:

$$C_p^{liq} m_{liq} \Delta T_s + C_p^{ice} m_{ice} \Delta T_s = \Delta H_{fus}^{ice} m_{ice}, \tag{18}$$

where m_{ice} is the ice mass, m_{liq} is the remaining liquid, C_p^{liq} and C_p^{ice} are the specific heat capacities of the liquid and ice, ΔT_s is the supercooling, and ΔH_{fus}^{ice} is the enthalpy of fusion for ice.

4. Results and Discussion

In the following, we will first discuss the experimental methodology (Sec. 4.1). Next, the influence of container material and fluid mixture (Sec. 4.2) on the solid-formation temperature will be evaluated by comparing the experiments to theoretical predictions. The growth rate of the crystal posterior to the solid-formation will be discussed (Sec. 4.3), before further remarks on the heterogeneous nucleation theory are given (Sec. 4.4). Binary water–alcohol mixtures containing methanol, ethanol, 1-propanol and 1-butanol will be considered. A minimum of four solid-formation events have been detected for each experimental point reported. For all experiments, a visual inspection confirmed that the solid-formation started at the container walls and not on the two sensor probes.

4.1. Experimental determination of the solid-formation temperature

The sensors were placed in a container with a 6 mL liquid sample according to the setup depicted in Fig. 1. The container was cooled down to −30°C at a rate of 0.2°C/min. The acquisition parameters and data processing was carried out as described in Section 2.2. Fig. 4 shows how the wavelengths shift for the two sensor types in a water-mixture with 9 mol% methanol during cooling, upon freezing, and during further cooling of the frozen solid.

Table 1: Value for the heterogeneity factor, f_{het} for the container materials considered in this work.

Material	Value
Glass	0.12
Polypropylene (new)	0.25

Both sensors shift towards shorter wavelengths (blue-shift) as the temperature is decreased. The non-linear thermo-optic properties of the liquid phase give a non-linear response for the thin-core (TC) sensor, as depicted in Fig 4-top. The responses from the two sensors in the liquid phase can be used to create a baseline, or a calibration curve. Any deviation from this behavior indicates a change in the properties of the sample, which in these experiments can be interpreted as the phase transition. This was further confirmed with the boroscope, which was used to visually monitor the sample.

Upon freezing, both sensors exhibit a sudden red-shift, i.e. a shift to longer wavelengths. This is attributed to the release of latent heat during freezing, which heats the sample. Because the solid phase consists of pure ice both for pure water and the binary mixtures, the concentration of the remaining liquid phase will increase during freezing. The temperature of a mixture during solid formation will thus proceed along a continuously decreasing curve.

Eventually, the freezing process slows down and the sample recovers a tight thermal match with the temperature bath, which can be seen by the wavelength of the Fiber-Bragg-Grating (FBG) sensor resuming a linear behavior, as shown in Fig. 4-bottom. However, the TC wavelength remains at a longer wavelength, also after the freezing process has completed. Because the sample temperature is now nearly equal to that of the temperature bath, this shift is attributed to an increase in the refractive index (RI) around the TC sensor. Pure ice has a lower RI than the liquid mixtures, and the increased RI is therefore assumed to be caused by the increased concentration of the remaining liquid phase surrounding the sensor. For pure water, the expected blue-shift is observed after freezing.

In summary, the combined output from the two sensors gives unique information on both the initiation and the progression of the phase transition. Because of the slow cooling rate and frequent acquisition, the freezing points can be detected with an uncertainty limited by the accuracy of the temperature bath (0.25 K).

4.2. Solid-formation temperatures in water–alcohol mixtures

In order to compare the experimental results to the predictions from the theory presented in Sec. 3, it is first

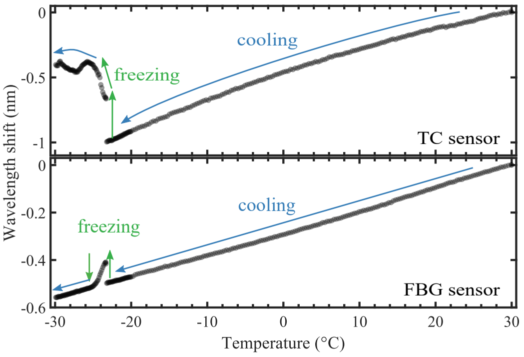

Figure 4: Wavelength shifts from the TC sensor (top) and the FBG sensor (bottom) as a function of temperature for a water–methanol mixture with 9 mol% methanol. The solid-formation event is indicated for both sensors.

necessary to determine the heterogeneity factor in Eq. 6. The heterogeneity factor was determined by reproducing the experimental solid-formation temperature of pure water by using the heterogeneous nucleation model presented in Sec. 3. We find that the value of f_{het} depend on the container material. The resulting values have been tabulated in Tab. 1. These values are in agreement with previous work by Zobrist et al. [60], who found hetereogeneity factors between 0.02 and 0.26 for nucleation on a nonadecanol surface. With the heterogeneity factor at hand, the theoretical model is fully predictive for the solid-formation temperatures of alcohol–water mixtures.

4.2.1. The influence of container type and cleaning procedure on the solid-formation temperature

To investigate the influence of container-type and experimental methodology on the solid-formation temperature, a series of tests was carried out with water-ethanol mixtures in two different container types, glass and poly-propylene (PP).

Fig. 5 shows that the solid-formation temperatures in new, untreated PP are lower than the corresponding temperatures in glass. PP is a highly hydrophobic material because of the long aliphatic polymer chains, and thus less wetting than glass. This is reflected in a significantly higher value for the heterogeneity factor (see Tab. 1).

The experimental protocol outlined in Sec. 2.3 involves cleaning the containers with both acetone and ethanol between the experiments in order to remove impurities. The same glass test tube was used for all experiments, and this procedure was found to give the most reproducible results. For the PP test tubes, a new, sterile test tube was used for each measurement. Further experiments were conducted with these to gain insight into the difference between the pristine and cleaned surfaces with regards to the solid-formation temperature.

The sterile PP surface gave solid-formation temperatures that were on average 5–6°C below those in glass. The cleaned PP surfaces still gave lower solid-formation temperatures than glass, as shown in Fig. 5, but less so than the sterile PP. Furthermore, the effect of cleaning the PP depended on the concentration of ethanol in the mixture. The 8.9 mol% ethanol did not freeze consistently and the point in the graph represents only one measurement. The almost constant difference between the sterile test tubes and the glass indicates that the cleaning procedure outlined in Sec. 2 is well suited for glass, but not for PP.

Cleaning the container with only acetone did not raise the solid-formation temperature to the same degree as using both acetone and ethanol. Hence, a possible explanation for the change in the solid-formation temperature is that ethanol molecules adsorb on the PP container wall and in this way enhances the surface interaction between the PP container wall and the ice due to increased hydrophilicity. This seems to be in contradiction to the findings by Wu et al. [70], who investigated the effect of varying the density of OH-groups in polyvinyl alcohols on heterogeneous nucleation [70]. The increased hydrophobicity with less OH-groups was argued to pose less of a constraint on the interfacial water molecules and lead to more efficient nucleation. We emphasize that heterogeneous nucleation is a complex phenomenon, where the solid-formation depends on many parameters in addition to the hydrophobicity of the container wall.

4.2.2. The influence of the cooling-rate and the experimental set-up on the solid-formation temperature

Theoretically, any temperature below the melting temperature will cause a nucleation event, provided enough time i.e. with an infinitely slow cooling rate. Hence, increasing the cooling rate will result in a lower freezing temperature, as was shown by Koga et al. [32]. Koga et al. used significantly higher cooling rates than us of 5, 10 and 20 °C/min. Although no systematic study was carried out in this work to investigate the influence of the cooling rate, we did not find any change in the solid-formation temperature with moderate changes (0.1 and 0.3 °C/min). In the theory presented in Sec. 3.3, the critical nucleation rate that was chosen represents a characteristic time-scale for solid formation. Since the critical nucleation rate was found to have a small influence on the predicted solid-formation temperature, this further supports that the solid-formation temperature should be rather insensitive to the cooling rate.

The fiber-optic sensors may influence the solid formation temperature if their surfaces are better nucleating agents than the container. However, from the videos captured with the boroscope, we can deduce that the crystal forms at the container wall. This would be the same for other methods used – if they affect the conditions in the sample, the solid formation temperature could be different. Since the nucleation event occurs on the container surface, there will be some delay before the sensors will be able to detect the phase-transition. The measurements indicate that the delay in the current setup depends on the crystal growth

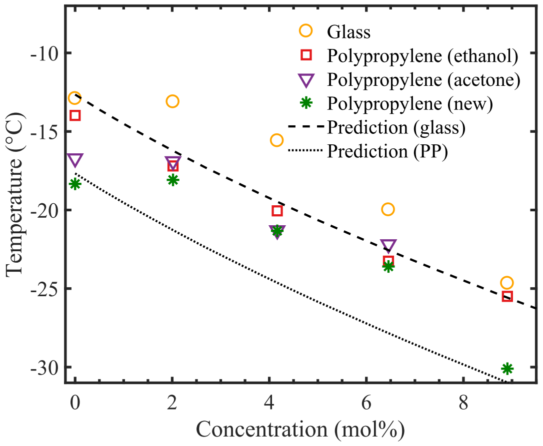

Figure 5: Comparison of ethanol–water solid-formation temperatures for glass and polypropylene test tubes, new sterile tubes or cleaned with acetone or ethanol.

rate, which decides how early the conditions around the sensors change in response to the new phase.

4.2.3. Results for binary water–alcohol mixtures

Fig. 6 compares the theoretical predictions from Sec. 2 to experimentally determined solid-formation and melting temperatures of ice in four binary water–alcohol mixtures. Only glass containers have been used in these experiments. The experimentally determined solid-formation temperatures are summarized in Tab. 2, and the complete data set is available in the SI.

As expected when dealing with heterogeneous nucleation, a few of the experiments gave significantly higher solid-formation temperatures than the trend. Although utmost care was taken to ensure a clean environment and pure samples, this was assumed to be caused by contaminants acting as nucleating agents [71]. When the experiments were repeated, the samples gave a solid-formation temperature in vicinity of the trend-line, which is interpreted as heterogeneous nucleation on the glass-liquid interface. However, for the pure water samples, a larger dispersion of freezing temperatures was observed. A possible explanation for this may be the absence of alcohol molecules in the solution that otherwise may adsorb on the glass surface. In pure water, the process is reversed as desorption of the ethanol and acetone molecules left from the cleaning stage may occur. This process may be less predictable and hence cause the larger dispersion. A large dispersion in solid formation temperatures is also seen for the 7.5 wt% butanol sample. This is close to the solubility limit for butanol (7.7 wt% at 20°C) and may therefore be caused by partial phase separation as the sample is cooled down.

Experiments were conducted with at least two different samples for each concentration. The samples were drawn from the same mixture reservoir and should therefore have the same concentrations. For each concentration, the samples were cooled to the freezing point a total of minimum three times (see SI for further details). The data for 0% (i.e. pure water) is the same for each binary mixture. To avoid systematic errors in the detected solid-formation temperatures, the measurement sequence was performed both with increasing and decreasing concentrations.

The experimentally determined melting temperatures of ice in binary water–alcohol mixtures with methanol, [72], ethanol, [72], 1-propanol [73] and 1-butanol [74] are reproduced to a reasonable accuracy by the CPA+Ice model described in Sec. 3.2. At higher alcohol concentrations, the model predictions give melting temperatures that lie above the tabulated values. While the melting temperatures from the theory follow a close to linear trend as a function of the alcohol concentration, the tabulated values are more parabolic. To gain further insight into this difference, we performed a sensitivity analysis of the CPA+Ice model. Changing the parameters of the ice model had a minor influence on the predicted melting points. In particular, it did not result in a non-linear curve for the melting points. A more accurate EoS for the water–alcohol mixtures than CPA is probably needed to improve the agreement between the experimental and predicted melting points. Although CPA predicts the vapor–liquid coexistence accurately, it can exhibit appreciable deviations for enthalpies of fusions, as shown for ethanol–water mixtures in the SI.

The solid-formation temperatures decrease with alcohol concentration, as shown in Fig. 6, and follow a similar trend as the melting temperatures. The degree of supercooling, shown in Fig. 7, varies between 11 K and 17 K. Unlike the solid-formation temperatures, the degree of supercooling has a much more curious behavior. For the mixtures with the alcohols of shortest chain-length, methanol and ethanol, the degree of supercooling displays a dip at the lowest concentrations, before it increases at higher concentrations. Within the uncertainty of the measurements, the supercooling of the mixtures with propanol and butanol appears to increase with alcohol concentration. The predictions from the heterogeneous nucleation model presented in Sec. 3.3 display qualitatively different trends than the experimental data. This creates a systematic deviation between the experiments and the predictions shown in Fig. 8, which varies from a 4 K overprediction for water-ethanol to a −3 K underprediction for water–butanol.

In the theoretical predictions, the degree of supercooling is to a good approximation a colligative property with alcohol mole percentages below about four, i.e. it depends only on the number of alcohol solute molecules. This may stem from the osmotic pressure entering the heterogeneous nucleation theory (Sec. 3.3). We found that the osmotic contribution from the term ΠV_c can be a large fraction of W, in some cases constituting 60% of the work of formation. For the low concentrations of alcohol considered here, the osmotic pressure is to a large extent a colligative property. We found that including the osmotic contribution was key to obtain a supercooling temperature that increases with alcohol concentration.

4.3. The kinetic prefactor and crystal growth

We showed in Sec. 4.2 that there is a qualitative difference between the measured values and the theoretical predictions of the solid-formation temperature in binary water–alcohol mixtures. In Sec. 3.3.2, we explained that the kinetic prefactor was proportional to the self-diffusion coefficient of water. This coefficient can be linked to the growth velocity of an ice crystal by use of Wilson–Frenkel theory (Eq. 16). In the following, we will investigate whether a poor description of the kinetic prefactor in the theory can be the cause of the deviation between theory and experiments.

A boroscope combined with video-recording and a careful post-processing enabled us to estimate the growth rate of ice crystals formed in water-ethanol mixtures at several compositions. The propagation length of the ice front as a function of time is shown in Fig. 9. The figure shows that the growth is close to linear, and the proportionality factor gives an approximately constant growth rate. Images of the crystal growth progresses can be found in the SI.

Tab. 3 reports the growth rates of crystals forming in different ethanol–water mixtures. The growth rate in pure water was found to be 10.2 cm/s. It was found to be 0.9/1.24 mm/s and 0.25 mm/s for 4.2 mol% and 11.5 mol% ethanol (10 and 25 wt%), respectively. After 0.8 s, the mass of ice produced was estimated to be approximately $1.1 \cdot 10^{-4}$ g and $2.5 \cdot 10^{-5}$ g for 4.2 mol% and 11.5 mol%, respectively. From these numbers, one can infer that the concentration in the remaining liquid phase remains to a large extent unchanged at this stage of the phase transition. Furthermore, the amount of ice formed during the investigation of the growth is much lower than the amount of ice that can be produced (~0.9 g) with the amount of supercooling achieved in the measurements, as estimated by Eq. 18. The crystal growth should therefore not be limited by the rate of heat transfer out of the test tube this early in the freezing process. These findings are in agreement with the work in Ref. [61], where it was shown that the crystal growth in pure water does not depend on heat dissipation in the early stages of the phase transition. This explains the nearly constant growth rates observed in the experiments.

For pure water, a crystal growth rate of 10.2 cm/s at 16 K supercooling is in excellent agreement with previous experimental studies [75–77]. The crystal growth retardation observed for the ethanol mixtures however, is one order of magnitude larger than what was found in freezing of aqueous NaCl solutions [77]. In a solution with 5 mol% NaCl (10 mol% dissociated, 14.6 wt%), the ice had a growth rate of 4 mm/s [77]. The higher growth rates in NaCl may be caused by a larger hydration shell around the ethanol molecules than the NaCl ions, which impedes the diffusion of water molecules. The slower crystal growth has been hypothesised to be because of the required diffusion of solute molecules away from the ice front, which is slower in more concentrated solutions [78].

To shed further light on the concentration dependence of the growth rate, we have used the Wilson–Frenkel theory [61, 69] in Eq. 16 with $\mu_w(T)$ computed by the CPA EOS to estimate an *effective* diffusion coefficient based on the experimentally determined growth rates. The effective diffusion coefficient plotted in Fig. 10 drops three orders of magnitude with addition of only 9 mole percent ethanol. This is in contrast to the experimentally determined self-diffusion coefficient of water in water–ethanol mixtures from Price et al. [78], which is reduced by a factor of two in the same interval due to the concentration dependence (see results at 298 K in Fig. 10). The reduced solid-formation temperature at higher alcohol concentrations is also expected to decrease the diffusion coefficient, although not to the extent displayed by the effective diffusion coefficient in Fig. 10.

For pure water, the self-diffusion coefficient obtained by the measured growth rates is in excellent agreement with the experimentally determined self-diffusion coefficient at 260 K, as shown in the figure. The large drop in the effective diffusion coefficient from Wilson–Frenkel theory with increasing ethanol concentrations probably points towards other effects than self-diffusion to be important, such as accumulation of ethanol molecules at the interface of the growing crystal. It is unclear whether such accumulation is as important for the critical cluster, as for the macroscopic crystals observed in the boroscope. Nonetheless, we have investigated the impact of replacing the self-diffusion coefficient used as input in Eq. 14 by that inferred by combining Wilson–Frenkel theory with the measured growth rates. This changes the predicted solid-formation temperature by less than 1 K, hence it cannot explain the systematic deviations between theory and predictions for the solid-formation temperature.

4.4. Further discussion of heterogeneous nucleation theory

To gain further insight into the origin of the discrepancy between the experiments and the predictions, we have carried out a comprehensive sensitivity analysis of the different components of the heterogeneous nucleation model presented in Sec. 3.3.

The onset nucleation rate of 1 critical cluster per second used in Eq. 17 has been chosen somewhat arbitrarily. We tested this choice by increasing and decreasing N_{crit} by a factor 1000. This changed the supercooling temperatures by less than 1 K. Hence, the exact choice of this parameter is not crucial for the theory.

We also tested the impact of varying the ice–water surface energy $\sigma_{i/w}$ by ±20%. Although this shifted the solid-formation temperature, it did not shift the trend.

Many of the assumptions in constructing the thermodynamic route to compute the activation barrier of ice in water-alcohol mixtures are questionable. For instance, the re-equilibration of the ice crystal with the solution has been

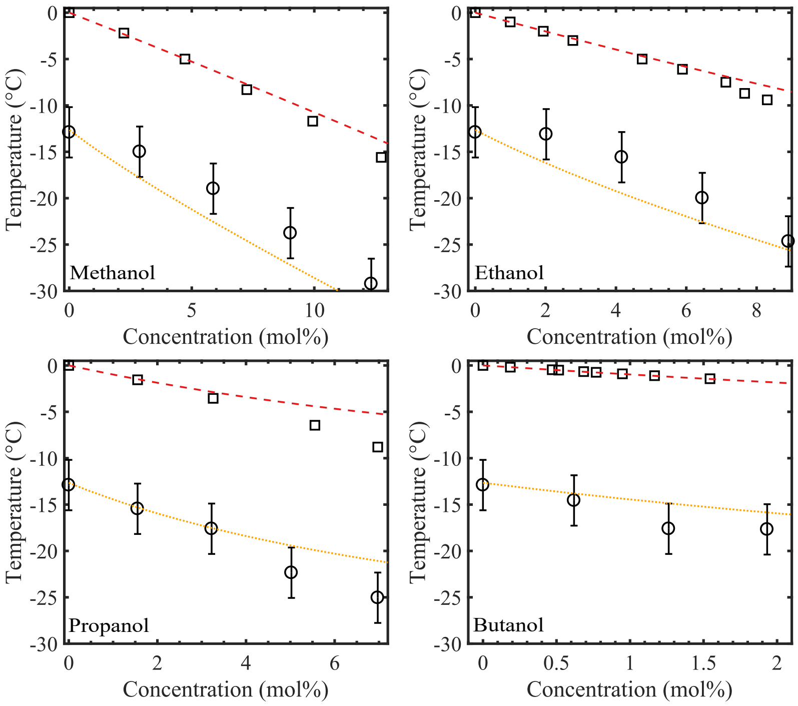

Figure 6: Plot of the experimental solid-formation temperatures (circles) for methanol, ethanol, 1-propanol and 1-butanol. Melting temperatures (squares) from [72] (methanol, ethanol) [73] (1-propanol) and [74] (1-butanol). The predicted freezing and melting temperatures are shown in dotted-yellow and dashed-red, respectively. Error bars include the measurement spread and the temperature bath accuracy.

Table 2: Solid-formation temperatures in a glass test tube. The mean temperatures are given, with the largest standard deviation of 2.2°C.

Concentration (weight):	0%	5%	10%	15%	20%
Methanol (°C):	-12.8	-15.0	-19.0	-22.8	-29.2
Ethanol (°C):	-12.8	-13.1	-15.6	-20.0	-24.6
Propanol (°C):	-12.8	-15.5	-17.6	-22.4	-25.0
Butanol (°C):	-12.8	-17.6	-	-	-

Table 3: Crystal growth rates for different concentrations of ethanol. The freezing temperatures are shown in parenthesis.

0 wt%	5 wt%	10 wt%	15 wt%	20 wt%	25 wt%
10.2 cm/s (-16.2°C)	1.9 mm/s (-12.4°C) 2.0 mm/s (-12.2°C)	0.9 mm/s (-17.4°C) 1.24 mm/s (-17.1°C)	0.66 mm/s (-19.9°C)	0.20 mm/s (-25.3°C)	0.25 mm/s (-26.3°C)

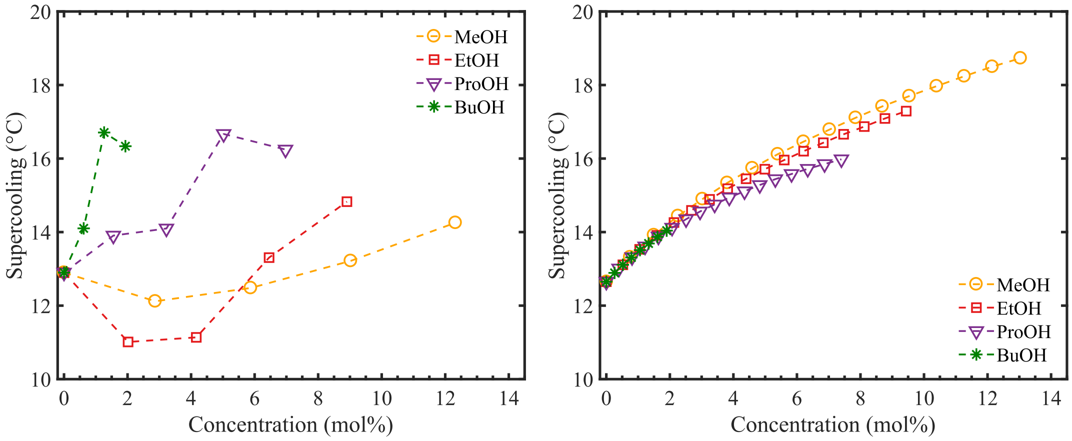

(a) Experimental.

(b) Theory predictions.

Figure 7: Comparison of the degree of achieved supercooling before solid formation for the water–alcohol mixtures from experiments (a) and predictions from theory (b).

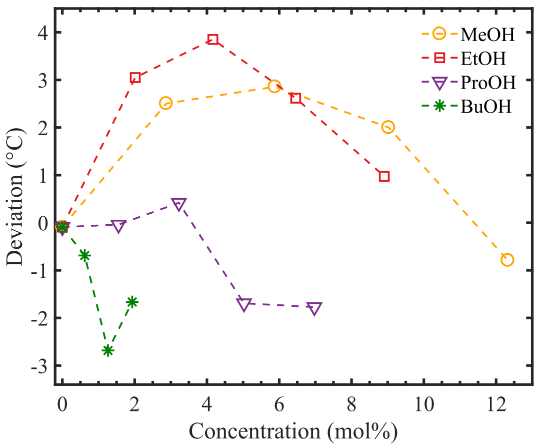

Figure 8: Deviation between measured solid-formation temperatures and predictions from heterogeneous nucleation theory.

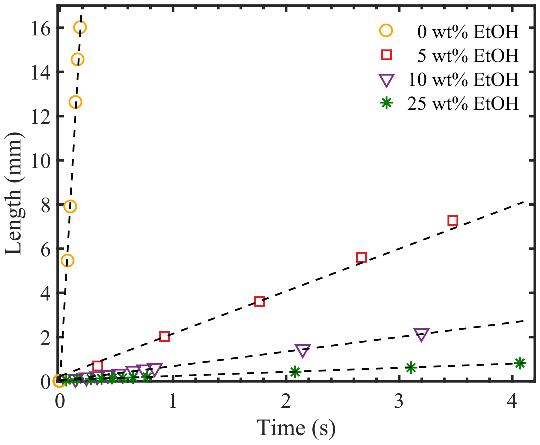

Figure 9: Propagation distance of the crystal surface during growth as a function of time. The curves are extrapolated to the expected time of the nucleation, set to zero. For pure water, the ice reaches the opposite side of the 16 mm inner diameter test tube after 0.18 s, which gives an average growth rate of 10.2 cm/s (linear fit). The unidirectional growth rates for the approximately spherical crystals in the ethanol mixtures are 0.9 mm/s and 0.25 mm/s for 4.2 mol% (10 wt%) and 11.5 mol% (25 wt%) ethanol, respectively.

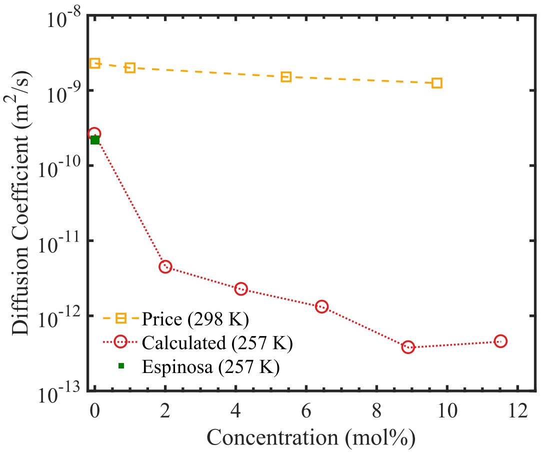

Figure 10: Diffusion coefficients calculated from combining Wilson–Frenkel theory (Eq. 16) with measured growth rates (Table 3), calculated chemical potentials and the radius ($a = 3$ Å) from de Hijes [61], together with values from Espinosa et. al (2016) [79] estimated at the same temperature (-16.2°C) and from Price et al. (2003) at 25°C [78].

neglected. Another possible reason for the discrepancy between the theoretical predictions and the measurements is the assumption that the heterogeneity factor, f_{het}, was assumed to be constant and equal to that of pure water. It follows from the expression (6) for the work of formation that, for each experiment, one can fit f_{het} to obtain a perfect match with the theory. For the glass container, we find that all experiments can be fitted in this way by varying f_{het} in the narrow interval 0.09–0.15. An important topic for future work in heterogeneous nucleation theory is therefore to develop a more reliable model for f_{het} for binary mixtures, which incorporates a dependence on both the alcohol type and composition.

Some of the deviation between the predicted solid-formation temperature and the measurements, e.g. for propanol, display a similar behavior as the misprediction of the melting temperature. Since the melting temperature is independent of the nucleation barrier, it seems reasonable that part of the deviations can be attributed to inaccuracies in the CPA+Ice model for the bulk thermodynamics.

5. Conclusion

In this work, we have investigated by theory and experiments the solid-formation and the melting temperature of ice in four binary water–alcohol mixtures containing methanol, ethanol, propanol and butanol.

A dual fiber-optic sensor set-up was use to obtain the solid-formation temperature. The solid-formation was detected by measuring a change in the refractive index of the sample and an increase in the local temperature due to the release of latent heat. The two sensors could independently detect the phase transition, but they could also be used for further analysis of the phase transition when combined. The growth rate of the ice crystal after formation was determined experimentally by use of a boroscope, video-recording and a careful post-processing analysis.

The predictions from the CPA equation of state combined with a model for pure ice were in good agreement with experimental results for the melting temperatures of binary water-alcohol mixtures. However, the theory over-predicted the melting points at higher alcohol concentrations. This was attributed to inaccuracies in the CPA equation of state.

Experiments with water–ethanol mixtures were conducted both in glass and polypropylene containers, where the latter exhibited a higher degree supercooling, amounting to 5-6°C. This was explained by the lower hydrophilicity of polypropylene. After exposing the polypropylene to pure ethanol in the cleaning procedure, the solid-formation temperature permanently increased. A possible explanation for this is that ethanol molecule adsorb on the wall and in the material of the container. No similar behavior could be observed for the glass containers, which were used in the remaining part of the experiments.

The solid-formation temperatures were shown to decrease with alcohol concentration, and followed a similar trend as the melting temperatures. The degree of supercooling varied between 11 K and 17 K and displayed a highly non-linear dependence on the alcohol concentration. For the mixtures with methanol and ethanol, the degree of supercooling displayed a dip at the lowest concentrations, before it increased at higher concentrations. The supercooling of the mixtures with propanol and butanol increased with the alcohol concentration.

A heterogeneous nucleation model was developed to predict the solid-formation temperatures of the binary alcohol–water mixtures. The predictions from this model displayed qualitatively different trends than the experimental data. A systematic deviation between the experiments and the predictions was observed, varying from a 4 K overprediction for water–ethanol to −3 K underprediction for water–butanol. The model predicted the degree of supercooling to be, to a good approximation, a colligative property. This was not in agreement with the experimental results, and sensitivity analyses pointed to inaccuracies in the work of formation as a likely reason for the deviations. Perhaps the crudest assumption in the theory was that the heterogeneity factor is independent of concentration, and a dependence on composition and mixture type may be necessary to improve the predictions.

For pure water, crystal growth rates of 10.2 cm/s at 16 K super-cooling were measured. These are in excellent agreement with previous results reported in the literature. The crystal growth rate observed in ethanol–water mixtures however, was much lower, where a crystal in a mixture with 4 mol% ethanol grew at a rate of 1 mm/s. The order-of-magnitude reduction in the growth rate with increasing ethanol concentration was hypothesized to result from accumulation of alcohol molecules at the crystal surface during the growth of the crystal.

6. Acknowledgement

This work was supported in part by the strategic research funding from the Norwegian University of Science and Technology (NTNU), in part by the Interreg Sweden-Norway program (IR2015.01), and in part by the Energy and Sensor Systems group (ENERSENSE, strategic research program at NTNU).

References

[1] J. MacAdam, S. A. Parsons, Calcium carbonate scale formation and control, Reviews in Environmental Science and Bio/Technology 3 (2) (2004) 159–169. `doi:10.1007/s11157-004-3849-1`.

[2] M. Boerkamp, D. W. Lamb, P. G. Lye, Monitoring the kinetics of heterogeneous crystal growth using an intrinsic exposed core optical fibre sensor, Sensors and Actuators, B: Chemical 240 (2017) 168–173. `doi:10.1016/j.snb.2016.08.133`.

[3] Ø. Wilhelmsen, D. Berstad, A. Aasen, P. Nekså, G. Skaugen, Reducing the exergy destruction in the cryogenic heat exchangers of hydrogen liquefaction processes, International Journal of Hydrogen Energy 43 (10) (2018) 5033–5047. `doi:10.1016/j.ijhydene.2018.01.094`.

[4] L. Zhang, Solid-fluid phase equilibria for natural gas processing at low temperatures, Ph.D. thesis, Norwegian University of Science and Technology, Department of Energy and Process Engineering (2012).

[5] B. Tohidi, A. Chapoy, J. Yang, Developing a hydrate-monitoring system, SPE Projects, Facilities & Construction 4 (01) (2009) 1–6. `doi:10.2118/125130-PA`.

[6] M. Tuinier, M. van Sint Annaland, G. Kramer, J. Kuipers, Cryogenic CO_2 capture using dynamically operated packed beds, Chemical Engineering Science 65 (1) (2010) 114–119. `doi:https://doi.org/10.1016/j.ces.2009.01.055`.

[7] A. Sharma, V. V. Tyagi, C. R. Chen, D. Buddhi, Review on thermal energy storage with phase change materials and applications, Renewable and Sustainable Energy Reviews 13 (2) (2009) 318–345. `doi:10.1016/j.rser.2007.10.005`.

[8] F. G. Qin, A. B. Russell, X. D. Chen, L. Robertson, Ice fouling on a subcooled metal surface examined by thermo-response and electrical conductivity, Journal of Food Engineering 59 (4) (2003) 421–429. `doi:10.1016/S0260-8774(03)00002-5`.

[9] S. Veesler, L. Lafferrère, E. Garcia, C. Hoff, Phase transitions in supersaturated drug solution, Organic Process Research & Development 7 (6) (2003) 983–989. `doi:10.1021/op034089f`.

[10] D. Erdemir, A. Y. Lee, A. S. Myerson, Polymorph selection: the role of nucleation, crystal growth and molecular modeling., Current opinion in drug discovery & development 10 (6) (2007) 746–755.

[11] J. R. Cox, L. A. Ferris, V. R. Thalladi, Selective growth of a stable drug polymorph by suppressing the nucleation of corresponding metastable polymorphs, Angewandte Chemie International Edition 46 (23) (2007) 4333–4336. `doi:10.1002/anie.200605257`.

[12] P. Mazur, Cryobiology: the freezing of biological systems, Science 168 (3934) (1970) 939–949. `doi:10.1126/science.168.3934.939`.

[13] A. Lintunen, T. Hölttä, M. Kulmala, Anatomical regulation of ice nucleation and cavitation helps trees to survive freezing and drought stress, Scientific Reports 3 (2013) 2031. `doi:10.1038/srep02031`.

[14] D. Zaragotas, N. T. Liolios, E. Anastassopoulos, Supercooling, ice nucleation and crystal growth: A systematic study in plant samples, Cryobiology 72 (3) (2016) 239–243. `doi:10.1016/j.cryobiol.2016.03.012`.

[15] H. Vehkamäki, Classical Nucleation Theory in Multicomponent Systems, Springer Verlag, Berlin, 2006. `doi:10.1007/3-540-31218-8`.

[16] W. G. Finnegan, S. K. Chai, A new hypothesis for the mechanism of ice nucleation on wetted AgI and AgI · AgCl particulate aerosols, Journal of the atmospheric sciences 60 (14) (2003) 1723–1731. `doi:10.1175/1520-0469(2003)060<1723:ANHFTM>2.0.CO;2`.

[17] B. J. Murray, S. Broadley, T. Wilson, J. Atkinson, R. Wills, Heterogeneous freezing of water droplets containing kaolinite particles, Atmospheric Chemistry and Physics 11 (9) (2011) 4191–4207. `doi:10.1039/c2cs35200a`.

[18] B. J. Murray, D. O'Sullivan, J. D. Atkinson, M. E. Webb, Ice nucleation by particles immersed in supercooled cloud droplets, Chemical Society Reviews 41 (19) (2012) 6519–6554. `doi:10.1039/c2cs35200a`.

[19] M. Fitzner, G. C. Sosso, S. J. Cox, A. Michaelides, The many faces of heterogeneous ice nucleation: Interplay between surface morphology and hydrophobicity, Journal of the American Chemical Society 137 (42) (2015) 13658–13669. `doi:10.1021/jacs.5b08748`.

[20] J. D. Atkinson, B. J. Murray, D. O'Sullivan, Rate of homogeneous nucleation of ice in supercooled water, Journal of Physical Chemistry A 120 (33) (2016) 6513–6520. `doi:10.1021/acs.jpca.6b03843`.

[21] G. C. Sosso, J. Chen, S. J. Cox, M. Fitzner, P. Pedevilla, A. Zen, A. Michaelides, Crystal nucleation in liquids: Open questions and future challenges in molecular dynamics simulations, Chemical Reviews 116 (12) (2016) 7078–7116. `doi:10.1021/acs.chemrev.5b00744`.

[22] E. Sanz, C. Vega, J. R. Espinosa, R. Caballero-Bernal, J. L. Abascal, C. Valeriani, Homogeneous ice nucleation at moderate supercooling from molecular simulation, Journal of the American Chemical Society 135 (40) (2013) 15008–15017. `doi:10.1021/ja4028814`.

[23] J. Yan, G. Patey, Heterogeneous ice nucleation induced by electric fields, The Journal of Physical Chemistry Letters 2 (20) (2011) 2555–2559. `doi:10.1021/jz201113m`.

[24] S. Karthika, T. K. Radhakrishnan, P. Kalaichelvi, A review of classical and nonclassical nucleation theories, Crystal Growth and Design 16 (11) (2016) 6663–6681. `doi:10.1021/acs.cgd.6b00794`.

[25] L. Lupi, A. Hudait, V. Molinero, Heterogeneous nucleation of ice on carbon surfaces, Journal of the American Chemical Society 136 (8) (2014) 3156–3164. `doi:10.1021/ja411507a`.

[26] R. Cabriolu, T. Li, Ice nucleation on carbon surface supports the classical theory for heterogeneous nucleation, Physical Review E - Statistical, Nonlinear, and Soft Matter Physics 91 (5). `doi:10.1103/PhysRevE.91.052402`.

[27] Y. Bi, R. Cabriolu, T. Li, Heterogeneous ice nucleation controlled by the coupling of surface crystallinity and surface hydrophilicity, Journal of Physical Chemistry C 120 (3) (2016) 1507–1514. `doi:10.1021/acs.jpcc.5b09740`.

[28] B. Glatz, S. Sarupria, Heterogeneous ice nucleation: Interplay of surface properties and their impact on water orientations, Langmuir 34 (3) (2018) 1190–1198. `doi:10.1021/acs.langmuir.7b02859`.

[29] F. K. Coradin, G. R. Possetti, R. C. Kamikawachi, M. Muller, J. L. Fabris, Etched fiber Bragg gratings sensors for water-ethanol mixtures: A comparative study, Journal of Microwaves and Optoelectronics 9 (2) (2010) 131–143. `doi:10.1590/S2179-10742010000200007`.

[30] P. Aursand, M. A. Gjennestad, E. Aursand, M. Hammer, Ø. Wilhelmsen, The spinodal of single- and multi-component fluids and its role in the development of modern equations of state, Fluid Phase Equilibria 436 (2017) 98–112. `doi:10.1016/j.fluid.2016.12.018`.

[31] K. Takaizumi, T. Wakabayashi, The freezing process in ethanol-water systems as revealed by differential scanning calorimetry, Journal of Solution Chemistry 26 (10). `doi:10.1007/BF02768051`.

[32] K. Koga, H. Yoshizumi, Diffential scanning calorimetry (DSC) studies on the freezing processes of water-ethanol mixtures and distilled spirits, Journal of Food Science 44 (5) (1979) 1386–1389. `doi:10.1111/j.1365-2621.1979.tb06444.x`.

[33] H. J. Borchardt, F. Daniels, The application of differential thermal analysis to the study of reaction kinetics, Journal of the American Chemical Society 79 (1) (1957) 41–46. `doi:10.1021/ja01558a009`.

[34] R. Anderson, R. Adams, B. Duggins, Limitations of thermocouples in temperature measurements, 25th ISA Anaheim CA (1979) 1–33.

[35] J. M. Campbell, F. C. Meldrum, H. K. Christenson, Is ice nucleation from supercooled water insensitive to surface roughness?, Journal of Physical Chemistry C 119 (2) (2015) 1164–1169. `doi:10.1021/jp5113729`.

[36] A. Dewaele, J. H. Eggert, P. Loubeyre, R. Le Toullec, Measurement of refractive index and equation of state in dense He, H_2, H_2O and Ne under high pressure in a diamond-anvil cell, Physical Review B 67 (9) (2003) 094112. `doi:10.1103/PhysRevB.67.094112`.

[37] D. Lee, R. Haynes, D. Skeen, Properties of optical fibres at cryogenic temperatures, Monthly Notices of the Royal Astronomical Society 326 (2) (2001) 774–780. `doi:10.1046/j.1365-8711.2001.04630.x`.

[38] M. Boerkamp, D. W. Lamb, P. G. Lye, Investigating surface crystal growth using an intrinsic exposed core optical fibre sensor, Sensors and Actuators, B: Chemical 157 (2) (2011) 581–585. `doi:10.1016/j.snb.2011.05.026`.

[39] P. Mani, A. Rallapalli, V. R. Machavaram, A. Sivaramakrishna, Monitoring phase changes in supercooled aqueous solutions using an optical fiber Fresnel reflection sensor, Optics Express 24 (5) (2016) 5395. `doi:10.1364/OE.24.005395`.

[40] W. Han, M. Rebow, D. Liu, G. Farrell, Y. Semenova, Q. Wu, Optical fiber Fresnel reflection sensor for direct detection of the solid–liquid phase change in n-octadecane, Measurement Science and Technology 29 (12) (2018) 125107. `doi:10.1088/1361-6501/aaeabb`.

[41] R. Kumar, W. Han, D. Liu, W. P. Ng, R. Binns, K. Busawon, Y. Q. Fu, Z. Ghassemlooy, C. Underwood, K. Mahkamov, J. Yuan, C. Yu, H. Shu, X. A. Li, T. Guo, G. Farrell, Y. Semenova, Q. Wu, Optical fibre sensors for monitoring phase transitions in phase changing materials, Smart Materials and Structures 27 (10) (2018) 105021. `doi:10.1088/1361-665X/aaddba`.

[42] W. Han, M. Rebow, X. Lian, D. Liu, G. Farrell, Q. Wu, Y. Ma, Y. Semenova, SNS optical fiber sensor for direct detection of phase transitions in C18H38 n-alkane material, Experimental Thermal and Fluid Science 109 (November 2018) (2019) 109854. `doi:10.1016/j.expthermflusci.2019.109854`.

[43] A. D. Kersey, M. A. Davis, H. J. Patrick, M. LeBlanc, K. P. Koo, Fiber grating sensors, Journal of Lightwave Technology 15 (8) (1997) 1442–1463. `doi:10.1109/50.618377`.

[44] R. C. Kamikawachi, I. Abe, A. S. Paterno, H. J. Kalinowski, M. Muller, J. L. Pinto, J. L. Fabris, Determination of thermo-optic coefficient in liquids with fiber Bragg grating refractometer, Optics Communications 281 (4) (2008) 621–625. `doi:10.1016/j.optcom.2007.10.023`.

[45] Y. Saito, J. J. Wang, D. A. Smith, D. N. Batchelder, A simple chemical method for the preparation of silver surfaces for efficient SERS, Langmuir 18 (8) (2002) 2959–2961. `doi:10.1021/la011554y`.

[46] M. S. Wahl, Ø. Wilhelmsen, D. R. Hjelme, Addressing challenges in fabricating reflection-based fiber optic interferometers, Sensors 19 (18) (2019) 4030. `doi:10.3390/s19184030`.

[47] K. Takaizumi, A curious phenomenon in the freezing-thawing process of aqueous ethanol solution, Journal of Solution Chemistry 34 (5) (2005) 597–612. `doi:10.1007/s10953-005-5595-6`.

[48] S. Facq, F. Danède, B. Chazallon, Ice particle crystallization in the presence of ethanol: An in situ study by Raman and X-ray diffraction, Journal of Physical Chemistry A 117 (23) (2013) 4916–4927. `doi:10.1021/jp4015614`.

[49] G. M. Kontogeorgis, E. C. Voutsas, I. V. Yakoumis, D. P. Tassios, An equation of state for associating fluids, Industrial & Engineering Chemistry Research 35 (11) (1996) 4310–4318. `doi:10.1021/ie9600203`.

[50] A. J. Queimada, C. Miqueu, I. M. Marrucho, G. M. Kontogeorgis, J. A. P. Coutinho, Modeling vapor-liquid interfaces with the gradient theory in combination with the CPA equation of state, Fluid Phase Equilibria 228 (2005) 479. `doi:10.1016/j.fluid.2004.08.011`.

[51] M. Oliveira, I. Marrucho, J. Coutinho, A. Queimada, Surface tension of chain molecules through a combination of the gradient theory with the CPA EoS, Fluid Phase Equilibria 267 (1) (2008) 83–91. `doi:10.1016/j.fluid.2008.02.020`.

[52] M. Hongo, T. Hibino, Measurement of vapor-liquid-equilibria of binary and ternary-systems containing 1-propanol, water and calcium-chloride at 298.15 K, Kagaku Kogaku Ronbunshu 15 (4) (1989) 863–867. `doi:10.1252/kakoronbunshu.15.863`.

[53] J. Hu, C. A. Haynes, A. H. Wu, C. M. Cheung, M. M. Chen, E. G. Yee, T. Ichioka, K. Nishikawa, P. Westh, Y. Koga, Chemical potential and concentration fluctuation in some aqueous alkane-mono-ols at 25°C, Canadian Journal of Chemistry 81 (2) (2003) 141–149.

[54] A. Kotsarenko, N. Yarymazaev, V. Kalinichenko, Pressure isotherms of saturated vapor over the diethylene glycol water-methanol system from 251.95 K to 298.15 K, Journal of Applied Chemistry of the USSR 62 (8) (1989) 1750–1752.

[55] A. Shalmashi, F. Amani, Densities and excess molar volumes for binary solution of water + ethanol, + methanol and + propanol from (283.15 to 313.15) K, Latin American Applied Research 44 (2) (2014) 163–166.

[56] A. Aasen, D. Reguera, Ø. Wilhelmsen, Curvature corrections remove the inconsistencies of binary classical nucleation theory, Physical Review Letters 124 (2020) 045701. `doi:10.1103/PhysRevLett.124.045701`.

[57] Ø. Wilhelmsen, D. Bedeaux, D. Reguera, Communication: Tolman length and rigidity constants of water and their role in nucleation, The Journal of Chemical Physics 142 (17) (2015) 171103. `doi:10.1063/1.4919689`.

[58] R. Feistel, W. Wagner, A new equation of state for H_2O ice Ih, Journal of Physical and Chemical Reference Data 35 (2) (2006) 1021–1047. `doi:10.1063/1.2183324`.

[59] Ø. Wilhelmsen, A. Aasen, G. Skaugen, P. Aursand, A. Austegard, E. Aursand, M. A. Gjennestad, H. Lund, G. Linga, M. Hammer, Thermodynamic modeling with equations of state: Present challenges with established methods, Industrial & Engineering Chemistry Research 56 (13) (2017) 3503–3515. `doi:10.1021/acs.iecr.7b00317`.

[60] B. Zobrist, T. Koop, B. P. Luo, C. Marcolli, T. Peter, Heterogeneous ice nucleation rate coefficient of water droplets coated by a nonadecanol monolayer, The Journal of Physical Chemistry C 111 (5) (2007) 2149–2155. `doi:10.1021/jp066080w`.

[61] P. Montero de Hijes, J. R. Espinosa, C. Vega, E. Sanz, Ice growth rate: Temperature dependence and effect of heat dissipation, The Journal of Chemical Physics 151 (4) (2019) 044509. `doi:10.1063/1.5103273`.

[62] P. Montero de Hijes, J. R. Espinosa, E. Sanz, C. Vega, Interfacial free energy of a liquid-solid interface: Its change with curvature, The Journal of Chemical Physics 151 (14) (2019) 144501. `doi:10.1063/1.5121026`.

[63] L. Ickes, A. Welti, C. Hoose, U. Lohmann, Classical nucleation theory of homogeneous freezing of water: Thermodynamic and kinetic parameters, Physical Chemistry Chemical Physics 17 (8) (2015) 5514–5537. `doi:10.1039/c4cp04184d`.

[64] T. van Westen, R. D. Groot, Predicting the kinetics of ice recrystallization in aqueous sugar solutions, Crystal Growth & Design 18 (4) (2018) 2405–2416. `doi:10.1021/acs.cgd.8b00038`.

[65] J. R. Espinosa, C. Vega, E. Sanz, Ice–water interfacial free energy for the TIP4P, TIP4P/2005, TIP4P/Ice, and mW models as

obtained from the mold integration technique, The Journal of Physical Chemistry C 120 (15) (2016) 8068–8075. `doi:10.1021/acs.jpcc.5b11221`.

[66] M. Warkentin, J. P. Sethna, R. E. Thorne, Critical droplet theory explains the glass formability of aqueous solutions, Physical Review Letters 110 (1) (2013) 015703. `doi:10.1103/PhysRevLett.110.015703`.

[67] C. A. Jeffery, P. H. Austin, Homogeneous nucleation of supercooled water: Results from a new equation of state, Journal of Geophysical Research: Atmospheres 102 (D21) (1997) 25269–25279. `doi:10.1029/97JD02243`.

[68] R. S. Smith, B. D. Kay, The existence of supercooled liquid water at 150 K, Nature 398 (6730) (1999) 788. `doi:10.1038/19725`.

[69] J. Frenkel, Note on a relation between the speed of crystallization and viscosity, Phisik. Zeit. Sowjetunion 1 (1932) 498–510.

[70] S. Wu, Z. He, J. Zang, S. Jin, Z. Wang, J. Wang, Y. Yao, J. Wang, Heterogeneous ice nucleation correlates with bulk-like interfacial water, Science Advances 5 (4) (2019) eaat9825. `doi:10.1126/sciadv.aat9825`.

[71] N. E. Dorsey, The freezing of supercooled water, Transactions of the American Philosophical Society 38 (3) (1948) 247. `doi:10.2307/1005602`.

[72] J. A. Lange, Lange's handbook of chemistry, 15th Edition, McGraw-Hill, Inc., New York, 1999.

[73] A. Chapoy, R. Anderson, H. Haghighi, T. Edwards, B. Tohidi, Can n-propanol form hydrate?, Industrial & Engineering Chemistry Research 47 (5) (2008) 1689–1694. `doi:10.1021/ie071019e`.

[74] B. Y. Okamoto, R. H. Wood, P. T. Thompson, Freezing points of aqueous alcohols. Free energy of interaction of the CHOH, CH_2, CONH and C=C functional groups in dilute aqueous solutions, Journal of the Chemical Society, Faraday Transactions 1: Physical Chemistry in Condensed Phases 74 (1978) 1990. `doi:10.1039/f19787401990`.

[75] H. R. Pruppacher, Interpretation of experimentally determined growth rates of ice crystals in supercooled water, The Journal of Chemical Physics 47 (5) (1967) 1807–1813. `doi:10.1063/1.1712169`.

[76] T. Buttersack, S. Bauerecker, Critical radius of supercooled water droplets: On the transition toward dendritic freezing, The Journal of Physical Chemistry B 120 (3) (2016) 504–512. `doi:10.1021/acs.jpcb.5b09913`.

[77] S. Bauerecker, P. Ulbig, V. Buch, L. Vrbka, P. Jungwirth, Monitoring ice nucleation in pure and salty water via high-speed imaging and computer simulations, Journal of Physical Chemistry C 112 (20) (2008) 7631–7636. `doi:10.1021/jp711507f`.

[78] W. S. Price, H. Ide, Y. Arata, Solution dynamics in aqueous monohydric alcohol systems, Journal of Physical Chemistry A 107 (24) (2003) 4784–4789. `doi:10.1021/jp027257z`.

[79] J. R. Espinosa, C. Navarro, E. Sanz, C. Valeriani, C. Vega, On the time required to freeze water, The Journal of Chemical Physics 145 (21) (2016) 211922. `doi:10.1063/1.4965427`.